First Principles Study of ZnO and Graphene Based Interfacial Electronic Structures for Nanoelectronics

TIAN, Xiaoqing

A Thesis Submitted in Partial Fulfillment
of the Requirements for the Degree of
Doctor of Philosophy
in
Electronic Engineering

The Chinese University of Hong Kong
September 2010

ProQuest LLC.
789 East Eisenhower Parkway
P.O. Box 1346
Ann Arbor, MI 48106 - 1346

Abstract

First Principles Study of ZnO and Graphene Based Interfacial Electronic Structures for Nanoelectronics

Submitted by Xiaoqing Tian

for the degree of Doctor of Philosophy in Electronic Engineering

at the Chinese University of Hong Kong

September 2010

Supervisor: Professor Jianbin Xu

Advances in experimental techniques such as nanofabrication, characterization and synthesis have resulted in the development of many novel and interesting materials and devices. Surfaces and interfaces play an indispensible role for nanoelectronics development. ZnO and graphene have drawn tremendous research interests in recent years, due to their exceptional merits in electrical, optical and magnetic applications. This thesis attempts to ferret out the current experimental research progress, particularly, the frontiers of ZnO and graphene based surfaces and interfaces, and employs first principles to explore their electronic structures, to acquire mechanistic understanding of experimental findings, and to shed light on rational design of functional devices.

First, we study the controllable modulation of the electronic structures of ZnO($10\bar{1}0$) surface functionalized by various types of carboxylic acids. The calculated structural results are consistent with the experimental ones attained by the Fourier transform infrared attenuated total reflectance (FT-IR-ATR). Mercapto-acetic acid molecules are found to contribute an abundance of band gap states into ZnO.

Mercapto-acetic monolayer functionalized ZnO($10\bar{1}0$) is on the verge of metal-to -insulator transition, which is consistent with the experimental finding of an conductivity increase by 6 orders of magnitude. Mercapto-acetic acid functionalized ZnO($10\bar{1}0$) surface shows a strong configuration-dependence for both electronic structure and adsorption energy. Moreover, mercapto-acetic acid molecule functionalized ZnO also shows facet-dependent characteristic in which the monolayer functionalized ZnO($2\bar{1}\bar{1}0$) does not show metal-to-insulator transition. Acetic acid does not contribute to the band gap states of ZnO($10\bar{1}0$), whereas benzoic acid and 9-anthracenecarboxylic acid do contribute an abundance of band gap states to ZnO($10\bar{1}0$).

Second, we study the band gap opening of graphene bilayer by F4-TCNQ doping and externally applied electric filed effects. With F4-TCNQ concentration of 8.0 $\times 10^{13}$ molecules/cm^2, the electrostatic charge transfer between each F4-TCNQ molecule and graphene is 0.45e, and the built-in electric field E_{bi} between the graphene layers could achieve 0.070 V/Å. The charge transfer and band gap opening of the F4-TCNQ doped bilayer graphene can be further modulated by externally applied electric field (E_{ext}). At 0.077 eV/Å, the gap opening at the Dirac point (K) ΔE_K = 306 meV and the band gap E_g = 253 meV are around 71% and 49% larger than those of the pristine bilayer under the same E_{ext}. By combining F4-TCNQ molecular doping and E_{ext}, the p-type semiconductor bilayer graphene are attained, with the band gap and hole concentration varied in a wide range.

Third, the self-assembly mechanism of PTCDA ultrathin films on graphene with the coverage in a range of 0.3~3 monolayers (MLs) are interrogated by first principles method. For α modification mode, with critical thickness of 1 ML, the growth of PTCDA on graphene follows the Stranski-Krastanov (SK) growth mode. In contrast, for β modification mode, the PTCDA can form two complete MLs on graphene substrate. From the thermodynamical viewpoint, α modification mode is more stable than β modification mode. At 1 ML, the PTCDA follows a continuous and planar packing arrangement on graphene, which is almost unperturbed by typical defects in graphene substrate. This is in consistentcy with the experimental findings. For α

modification mode with 2 and 3 ML coverage, the bulk-like phases appear. At the same time, the total charge transfer between PTCDA and graphene per $5\sqrt{3}\times5$ super cell at 2 MLs saturates with $0.42e$, which is larger than those of 1 or 3 ML coverage.

Finally, the magnetic properties of graphene by organic molecule modification are investigated by first principles method. For the first time, we demonstrate that methoxyphenyl group can introduce a delocalized *p*-type ferromagnetism into graphene sheet, with the Curie temperature (T_c) above room temperature. Each aryl group can totally induce 1 μ_B into molecule/graphene system. Moreover, an around 1.1 eV direct band gap is introduced into both majority and minority spin bands of graphene by methoxyphenyl group modification. Zigzag graphene nanoribbon (GNR) shows strong site-specific magnetism by aryl group adsorption near the edge. At specific site of GNR, each molecule could totally induce 3~4 μ_B into molecule/GNR hybrid system.

These four theoretical sub-topics stem from the experimental advances in ZnO and graphene based surfaces and interfaces. They form the mechanistic understanding of the respective surfaces and interfaces down to the molecular level.

論文摘要

面向納米電子學的基於氧化鋅和石墨烯界面電子結構的第一性原理計算

田曉慶

香港中文大學
電子工程哲學博士學位

二零一零年九月

導師：許建斌教授

實驗技術的進展尤其是納米加工，表征和合成，產生了很多新奇的材料和器件。表面和界面是納米電子學發展的重要平臺。鑒於在電學，光學和磁學方面的應用的前景，关于氧化鋅和石墨烯的研究引起了廣泛的興趣。本論文努力去追踪基於氧化鋅和石墨烯表面和界面的實驗進展和前沿，用第一性原理計算的方法研究相應的電子結構，闡述實驗中的关键物理結果，並且給予實驗提供有益的理论基础和思考分析。

首先，我們研究了用多種羧酸分子可控性調控氧化鋅$(10\bar{1}0)$表面的電子結構。計算中得到的最穩定的吸附構型和傅立葉紅外變換光譜的實驗結果一致。巰基乙酸分子可以向氧化鋅禁帶中提供大量電子態密度。巰基乙酸單分子層功能化氧化鋅表面處在半導體向金屬態轉變的臨界狀態，与實驗中發現的氧化鋅電導率提高6個數量級结构相符。巰基乙酸分子功能化氧化鋅$(10\bar{1}0)$表面其電子結構和吸附能具有強烈的構型差異特性。巰基乙酸分子功能化氧化鋅表面電子結構同时具有晶向差異特性，巰基乙酸分子功能化氧化鋅$(2\bar{1}\bar{1}0)$表面沒有發生半導體向金屬態轉變。乙酸分子不能向氧化鋅禁帶提供電子態密度，而苯甲酸和9-蒽甲酸可以向氧化鋅禁帶提供大量電子態密度。

其次，我們用2,3,5,6-四氟-7,7',8,8'-四氰二甲基對苯醌 (F4-TCNQ) 摻雜以及外加電場的方法調制雙層石墨烯的禁帶寬度。當F4-TCNQ的濃度為8.0×10^{13}分子/平方厘米時，每個F4-TCNQ分子從石墨烯獲得0.45個電子，兩層石墨烯之間的

内建電場為0.070伏/埃。由F4-TCNQ摻雜后的雙層石墨烯其電荷轉移和禁帶寬度可以進一步被外加電場調制。當外加電場達到0.077伏/埃時，狄拉克點的能級之差為306毫電子伏特，禁帶寬度為253毫電子伏特，分別比純淨的双層石墨烯在同樣強度的外電場下對應的狄拉克點的能級之差和禁帶寬度提高了71%和49%。通過F4-TCNQ摻雜及電場調節，我們可以得到具有*p*-型半導體特性的雙層石墨烯。采用以上的方法，雙層石墨烯的禁帶寬度及電荷密度可以控制在較大的範圍內。

再次，對菲四甲酸二酐(PTCDA)超薄膜在石墨烯表面的自主裝機制用從頭算方法進行了研究。PTCDA超薄膜的厚度為0.3個單分子層到3個單分子層。對於α生長模式，臨界厚度為1個單分子層，所以PTCDA 在石墨烯表面遵循層島結合的生長模式。對於β生長模式，PTCDA在石墨烯表面的臨界厚度為兩個單分子層。從熱力學的觀點分析，α生長模式比β生長模式穩定。對於單分子層，PTCDA在石墨烯表面遵循平面排列的連續結構，並且這種結構不被典型的缺陷態擾動，這和實驗結果一致。對於α生長模式，當PTCDA的厚度為2到3個分子層時，類體相結構會出現。兩層PTCDA和石墨烯5√3×5元胞的電荷轉移為0.42個電子，這比單層和三層PTCDA和石墨烯的電荷轉移大。

最後，用第一性原理計算的方法研究了有機分子功能化的石墨烯磁性。我們首次發現了甲氧苯基功能化的石墨烯具有*p*型擴展態鐵磁性，居裏溫度高於室溫。每個甲氧苯基基可以向分子/石墨烯體系中引入1個玻爾磁子。同時，石墨烯中自旋向上和自旋向下的能帶都被引入了約1.1電子伏特的禁帶寬度。之字形邊緣的石墨帶具有強烈的位點取向磁矩特性。在石墨帶邊緣特定的位點，每個分子可以向分子/石墨帶雜化體系中引入3~4個玻爾磁子。

這四個界面專題理論研究來源於氧化鋅和石墨烯表面和界面的實驗進展，我们的结果闡明了面向納米電子學的先進材料其界面原子級尺度的电子结构特性和支配这些特性的物理機制。

Acknowledgements

First of all, I would like to express my immense gratitude to my supervisor Prof. J. B. Xu, who has provided an enormous myriad of crucial guidelines and patient instructions to my research work. I have also learned a lot of research methods for material sciences from him. Prof. Xu's insightful senses into nanoelectronics have inspired me to learn and investigate semiconductor materials.

I would like to thank Dr. N. Ke and Mr. W. K. Chan for their valuable assitance in laboratory and daily life issues.

I would like to thank Mr. Frank Ng and Mr. Stephen Chan of ITSC of CUHK for their technical assistance and support in high performance computing (HPC) facilities.

My profound gratitude is devoted to my current Solid State Electronics & Photonics labmates, Dr. W. G. Xie, Ms. Q. L. Chen, Mr. J. Du, Mr. D. X. Xia, Mr. M. D. Wang, Mr. H. X. Zhang, Mr. X. M. Wang, Mr. Y. R. Su, Mr. X. Wan, Mr. K. Chen, Mr. H. F. Lu, Mr. Z. W. Kang, Drs. Y. Li, C. L. Wang, and previous labmates, Drs. K. Xue, J. An, X. F. Wang, Mr. X. J. Yu, Mr. J. Gao, Mr. H. Z. Zeng, Drs. C. M. Sun, W. Yuan, and Y. Chen (BME Lab and Southeast University) who have made my research activities interesting in Hong Kong, by their encouragement and appreciation.

Also I wish to thank Profs. R. Car and A. Selloni for their kind-hearted host, co-supervision and stimulating discussions during my visit to Princeton University in 2008. Drs. F. Zipoli, X. F. Wu, A. Satta, W. Chen, Mr. Z. F. Li and Mr. L. Lin of Princeton University are gratefully acknowledged for their kind-hearted help and stimulating discussions.

I would like to thank my family for their support.

Table of Contents

List of Figures

List of Tables

Chapter 1 Introduction to ZnO and Graphene Based Interfacial Electronic Structures

ZnO and graphene have drawn tremendous research interest in recent yeas, due to their merits of applications in electrical, optical and magnetic areas. Their electronic structures determine their properties and potentials in these areas. Therefore, how to manipulate the electronic structures of ZnO and graphene is of fundamental importance. Surface and interface play the role as platform for current top down and bottom up nanotechnology.

1.1 ZnO($10\bar{1}0$) and ZnO($2\bar{1}\bar{1}0$) Majority Surfaces

1.1.1 Structure of ZnO Crystal and Its Majority Surfaces

ZnO crystal is composed of zinc and oxygen atoms. The bonding between Zn and O is composed of partial ionic bond and partial covalent bonds. ZnO crystal has wurtzite structure, with 2 O and 2 Zn atoms respectively in its primitive cell as shown in Figure 1.1(a). Its lattice constants are a = 3.249 Å and c = 5.205 Å. ZnO has two majority surfaces: ZnO($10\bar{1}0$) and ZnO($2\bar{1}\bar{1}0$), which are also non-polar surfaces as shown in Figure1.1(b). The surface energy of ZnO ($10\bar{1}0$) and ZnO($2\bar{1}\bar{1}0$) are lower than other sufaces, which makes them frequently appear as majority surfaces of experimentally synthesized nanocrystal.[1] The surface structure of these two majority surfaces are drastically different from bulk, and there is an obvious buckling that the topmost O atoms are higher than that of Zn atoms, which is believed to be partial charge transfer from topmost Zn atoms to topmost O atoms.

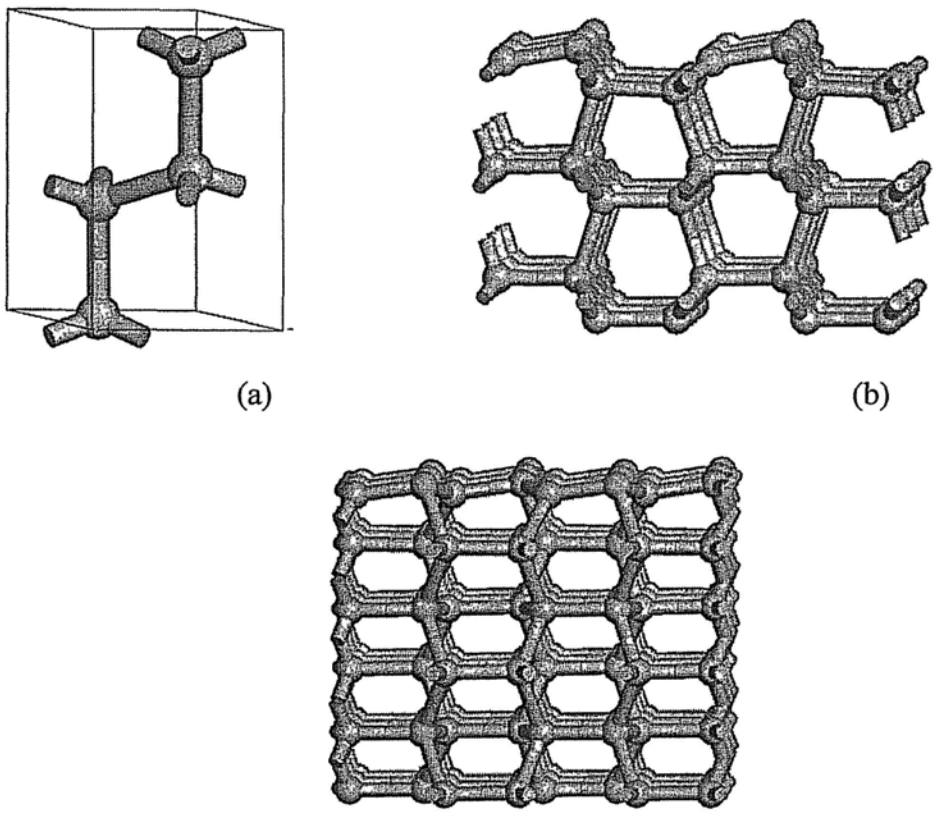

Figure 1.1 (a) ZnO primitive cell, surface slab models of (b) ZnO $(10\bar{1}0)$ surface and (c) ZnO $(2\bar{1}\,\bar{1}0)$ surface. Oxygen atoms are red and zinc atoms are ice blue.

1.1.2 Atomic-Scale Characterization of ZnO Majority Surfaces.

Advances in experimental characterization techniques, especially the emerging of STM and AFM, which achieve to measure the geometric and electronic structures of surface and interface at atomic-scale. In 2002, U. Diebold *etal.* have used STM to characterize the ZnO majority surfaces.[2] The well-defined ZnO$(10\bar{1}0)$ flat terraces, separated by monoatomic steps appears, running either along the [0 0 0 1] or $[\bar{1}2\bar{1}0]$ crystallographic directions as shown Figure1.2(a). The well defined flat terraces with scale of 2nm×2nm facilitate the possibility of atomic manipulation as the STM manipulation of Mn atoms on GaAs(110).[3] Near-atomic resolution was gained for ZnO$(10\bar{1}0)$ as shown in Figure2(b). From Figure2(b), dark and bright atomic rows can be seen running along the $[\bar{1}2\bar{1}0]$ direction. The dark and bright atomic rows are associated with ZnO dimmers along $[\bar{1}2\bar{1}0]$.

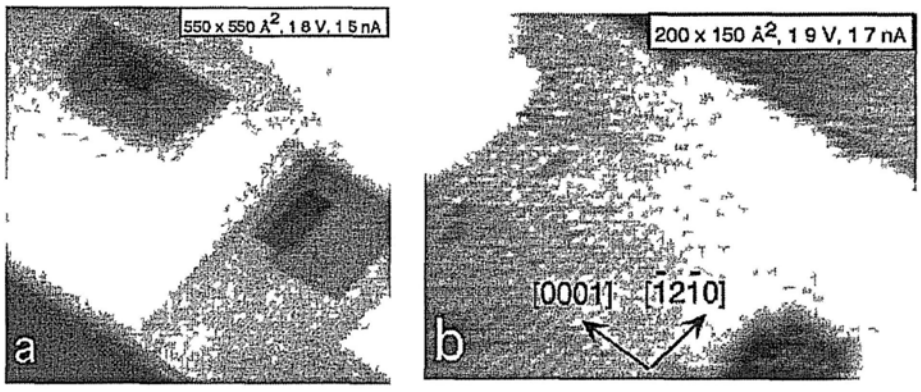

Figure 1.2 STM images of the ZnO(10$\bar{1}$0) surface. (a) The large-scale image shows flat terraces that are separated by single-layer height steps. (b) Near-atomic-resolution image with bright and dark rows running along the [$\bar{1}$2$\bar{1}$0] direction. Taken from Ref. 2.

The STM images of ZnO(2$\bar{1}$ $\bar{1}$0) are shown in Figure 1.3. From its STM images, we could find that the surface of ZnO(2$\bar{1}$ $\bar{1}$0) is rougher than ZnO(10$\bar{1}$0).

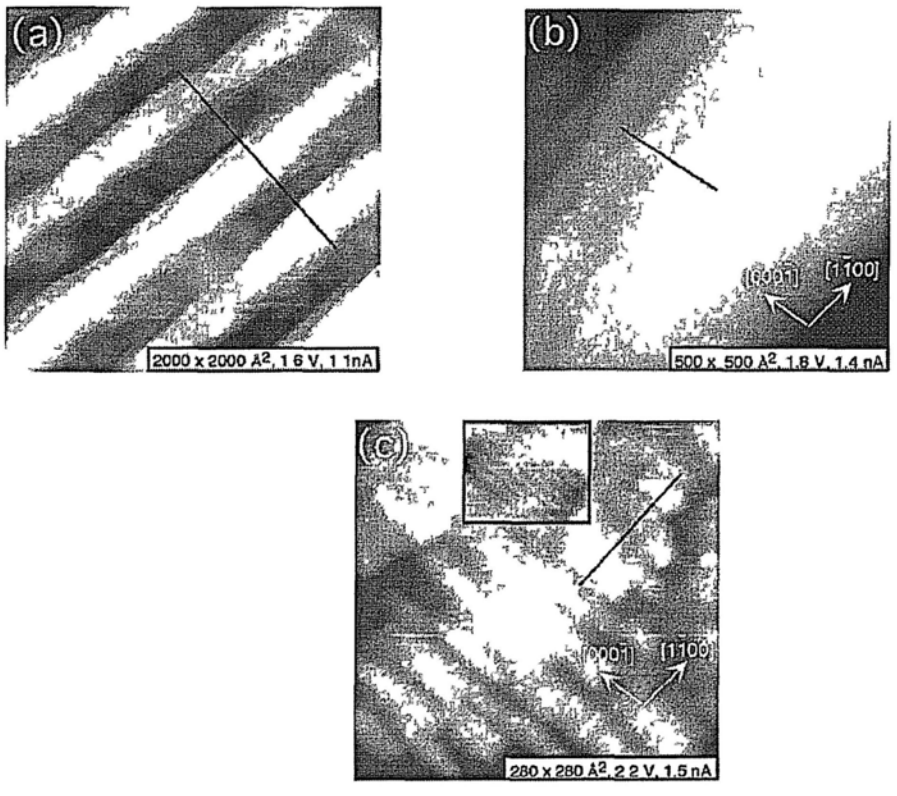

Figure 1.3 STM images of the ZnO(2$\bar{1}$ $\bar{1}$0) surface. (a) The large-scale image shows 200-300 Å wide and 35–65 Å deep grooves that are running along the [$\bar{1}$100] direction. (b) The sides of the grooves ascend in a cascade of terraces separated by multiple-height steps. (c) The smaller scale image shows a high density of small terraces elongated in the direction of the atomic rows The inset shows a nearatomic resolution image with atomic rows running along the [0 0 0 1] direction Taken from Ref. 2.

1.1.3 STS of ZnO Majority Surfaces

From the STS of ZnO surfaces as shown in Figure1.4, the clean majority surfaces have a band gap around 2.5 eV, which is smaller than the general value 3.3 eV. This band gap reduction is believed to come from defects, such as O vacancy, and interstitial Zn.

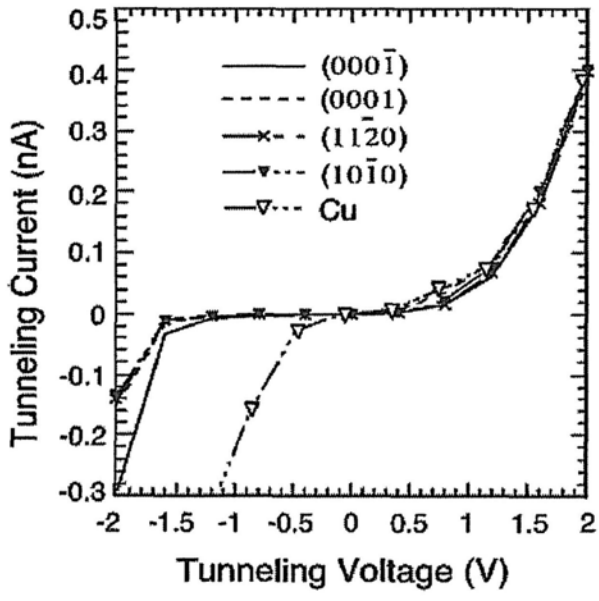

Figure 1.4 STS of four low-index surfaces of ZnO and Cu. The same settings for the sample bias and tunneling current of 2 V and 0.4 nA, respectively, were used. The Cu curve is shown as a reference for a metallic behavior. Taken from Ref. 2.

1.1.4 Metal Doped ZnO Majority Surfaces

The growth of Cu on ZnO majority surfaces is of interest for surface catalysis and the low-temperature synthesis of methano, water-gas shift reaction, and methanol steam reforming.[4, 5] The surface adsorption and reaction for sulphide on Cu/ZnO majority surfaces have also been investigated. [6, 7] The growth mechanism of Cu on ZnO is also of research interest, as it is considered as a model two-dimensional (2D) growth. The growth for Cu on ZnO(10 $\bar{1}$ 0) follows Vollmer-Weber growth mode (3D island like), due to the interaction between Cu atoms is stronger than that between Cu and ZnO(10 $\bar{1}$ 0) surface.[4] The STM images for Cu growth on ZnO(10-10) are shown in Figure 1.5. The clusters nucleate first at step edges and then nucleate on the center

of flat terrace, because there are dangling bonds at step edges and the adsorption energy is larger than that adsorption on center of flat terrace. When the coverage is increased, the Cu clusters begin to nucleate on the center of flat terrace. The average cluster heights are 7.2, 8.9, 11.8, and 14 Å, and the average cluster diameters are 34, 36, 38, and 45 Å at 0.05, 0.1, 0.25, and 0.5 ML coverage, respectively. So the growth of Cu on clean ZnO($10\bar{1}0$) follows 3D island like model. Cu growth on another majority surface ZnO($2\bar{1}\bar{1}0$) also follows the 3D island like model.[7]

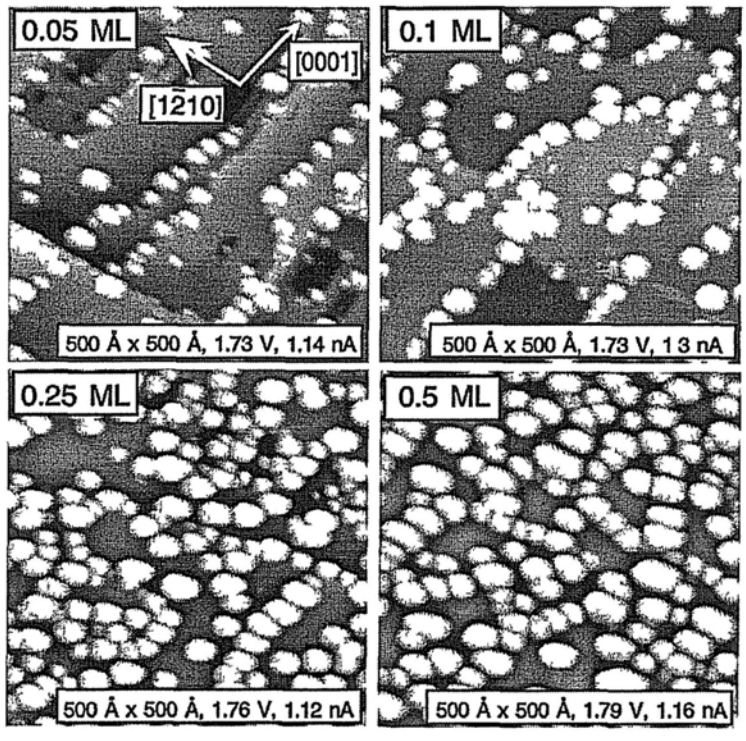

Figure 1. 5 *STM images for various Cu coverages (0 05-0.5 ML) on the ZnO($1\ 0\bar{1}0$) surface* Taken from Ref. 4.

1.1.5 Organic Molecule Doped ZnO Majority Surfaces

Organic molecule functionalized ZnO surface could be used to tune its electronic structure, and the corresponding transport properties could be modulated.[8] Besides, the organic molecule functionalized ZnO could have a good contact with metal electrodes.[9] Another application of organic molecule functionalized ZnO is dye-sensitized solar cells.[10,11] The comparison of contact between Au and ZnO with

and without $HOOC(CH2)_{10}COOH$ functionalization is shown in Figure1.6. Without organic molecular layer coating, the contact between Au and ZnO is Schottky contact of height Φ_B. When there is an organic layer between Au and ZnO, the energy barrier between ZnO and Au is drastically reduced, and the contact has been tuned from Schottky contact to Ohmic contact.[8] This contact improvement could increase the conductivity of the one dimensional device.

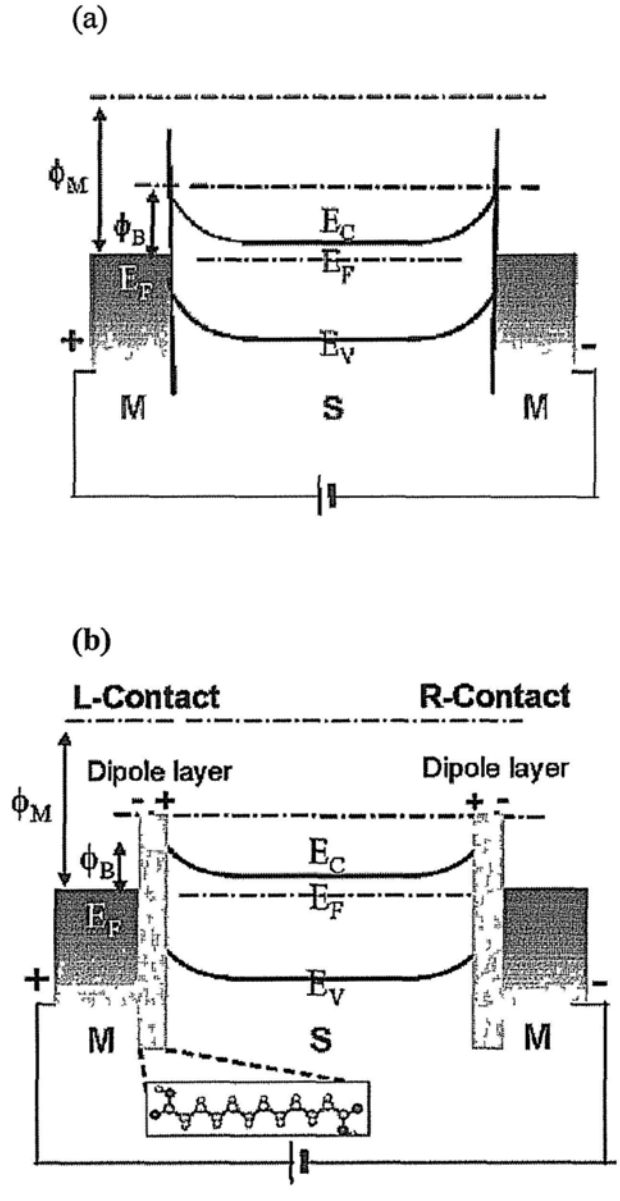

Figure 1.6 (a) Energy-level diagram of metal/semiconductor/metal interfaces, Φ_M is the work function of the metal. There is an energy barrier Φ_B between the metal contact and the untreated NB. (b) Energy-level diagram of Au electrode and a ZnO NB with a thin molecular layer between. The molecules form an interface dipole layer, which helps to decrease the energy barrier between the NB and Au. Taken from Ref. 8.

Poly(3-hexylthiophene) (P3HT) coated ZnO was used as dye-sentized solar cells as shown in Figure1.7. It was found that the morphologies could influence the photo-to-current convention efficiency.[12] P3HT plays the role as molecular donor while ZnO as semiconductor acceptor. The nano-scale morphology of P3HT on ZnO($10\bar{1}0$) has been investigated by DFT based *ab initio* calculation method as shown in Figure 1.8.[13]

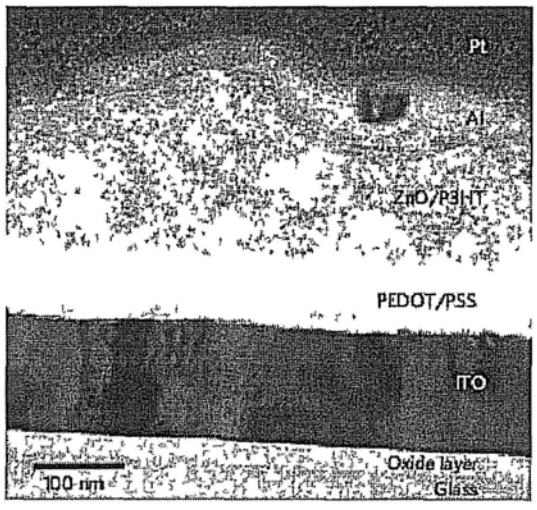

Figure 1.7 Transmission electron micrograph of a cross-section of a typical P3HT/ZnO photovoltaic cell. Taken from Ref. 12.

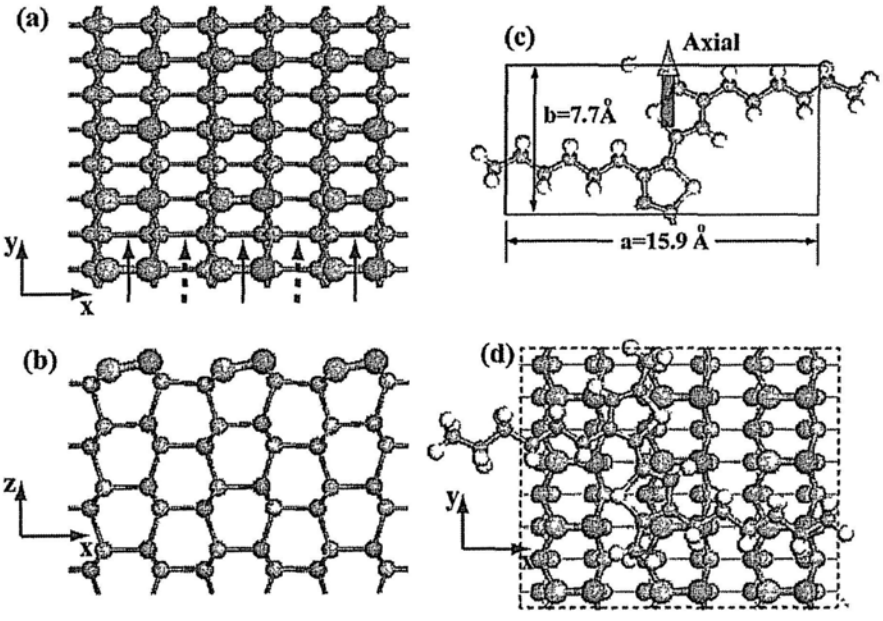

Figure 1.8 Schematic description of (a) top view and (b) side view of dimerized ZnO ($10\bar{1}0$) surface. Zn and O atoms on the surface are indicated by blue and red balls, respectively. Solid line arrows show ZnO dimer row, dashed arrows show the trench between two ZnO dimer rows. Taken from Ref. 13.

1.2 Graphite and Graphene

1.2.1 Structure of Graphite and Graphene

Graphite crystal has hexagonal layered structure, with 4 atoms in its primitive cell, which is shown in Figure1.9 (a). Its lattice constants are a =2.462 Å and c = 6.710 Å. The graphene is single layer exfoliated from graphite, and its structure is shown in Figure1.9 (b).

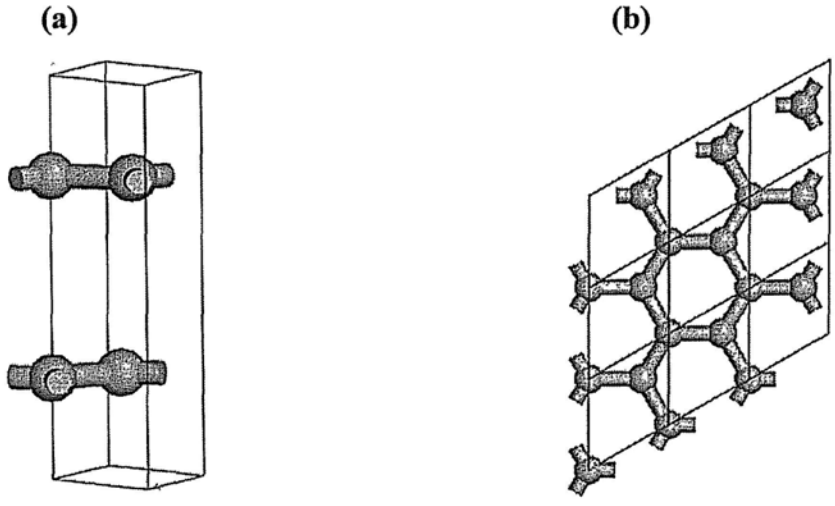

Figure 1.9 (a) Primitive crystal of graphie, (b) 3×3 cell of graphene.

1.2.2 Organic Molecule Functionalized Graphene

The electronic structure of graphene could be modulated by different aromatic molecules, and accordingly different properties could be gained such as p type and n type doping. For example, using Na-NH_2 and An-CH_3 n type doped graphene could be gained, and p type doped graphene could be gained by An-Br and TPA doping.[14] The molecular structures of organic dopants are shown in Figure 1.10. By p type doping, the Raman G and 2D frequencies are shifted up; meanwhile the Raman 2D frequencies are shifted up and Raman G band frequencies are shifted down by n type down as shown in Figure 1.11.

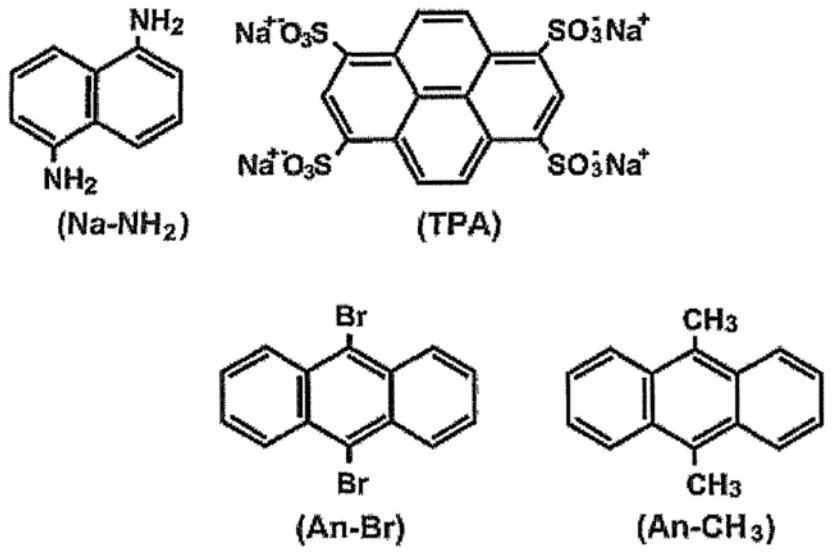

Figure 1.10 Chemical structures of the aromatic molecules used as dopants.

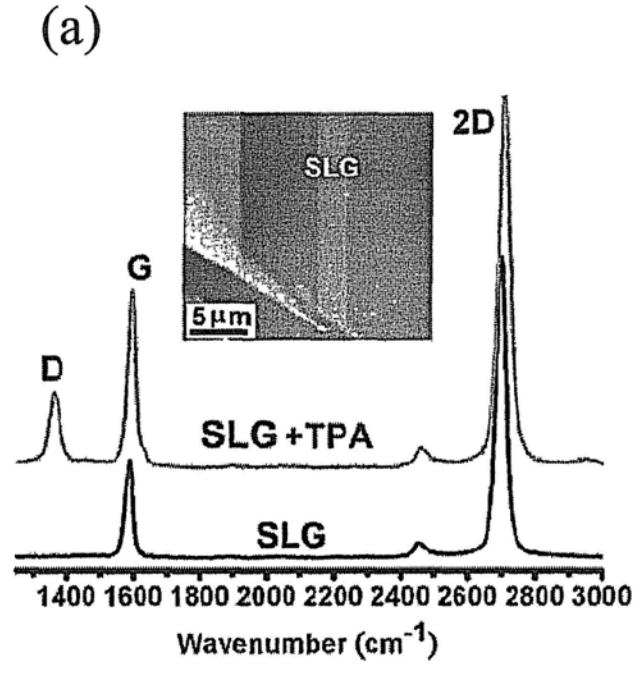

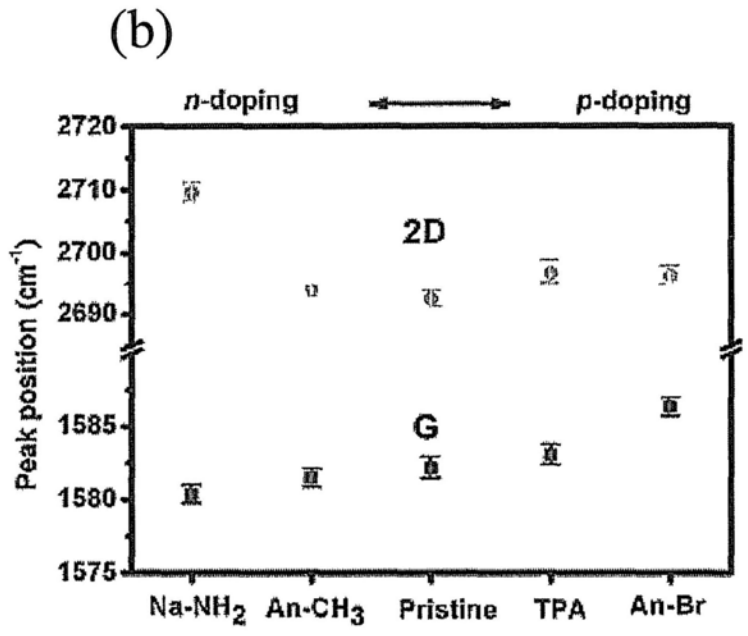

Figure 1.11 (a) Typical Raman spectra obtained from SLG (bottom) and SLG modified with TPA molecules (top). Inset: AFM image of a typical SLG film. (b) Statistical intensity ratio I(2D)/I(G) for SLG films modified with various aromatic molecules. Error bars indicate standard deviations. Taken from Ref. 14.

The *p* type doping of graphene was realized by tetrafluoro-tetracyano quinodimethane (F4-TCNQ) adsorption on the graphene surface as shown in Figure 1.12.[15] The charge transfer only occurs at the F4-TCNQ interface, and the bulk F4-TCNQ film remains largely uncharged. The F4-TCNQ doped graphene rem. The work function was increased by 0.7 and 1.3 eV, by depositing 0.1 and 0.2 nm F4-TCNQ on graphene respectively. The work function of chemically inert substrate such as graphene and graphite is increased only if there is charger transfer from substrate to adsorbate overlayer. The charge transfer creates an interfacial dipole which causes the up shift of work function of graphene. The F4-TCNQ doping is a nondestructive and effective method to modify the electronic structure of graphene.

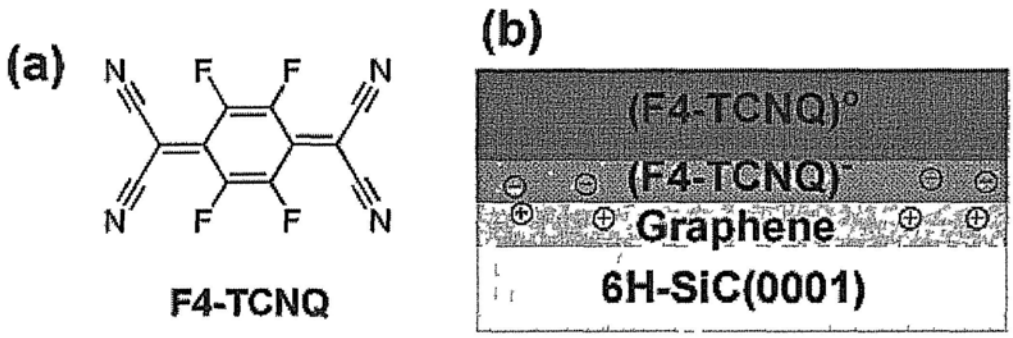

Figure 1.12 Schematic drawings of (a) structure of tetrafluoro-tetracyanoquinodimethane (F4-TCNQ) and (b) the charge transfer at the F4-TCNQ/graphene interface. Electron transfer from graphene to F4-TCNQ only occurred at the interface, where F4-TCNQ (in direct contact with graphene) is negatively charged and graphene is positively charged. F4-TCNQ in multilayers remains its neutral state (uncharged). Taken from Ref. 15.

The self-assembly of an *n* type organic semiconductor of perylene-3,4,9,10-tetracarboxylic dianhydride (PTCDA) on graphene have been investigated by STM and synchrotron photoemission spectroscopy (PES) as shown in Figure 1.13.[16, 17] The PTCDA molecular planes are parallel to graphene substrate, and exhibits as herringbone arrangement molecular planes. The molecular planes are stable and continuous at the substrate step edges. The defects in substrate have very limited on the structural perturbation effects on the structures of molecular planes. The PES study reveals that there is weak charge transfer from graphene to PTCDA. The PTCDA functionalized could be used as the substrate of nano-electronic devices, and the PTCDA adlayers could facilitate the atomic layer deposition of dielectric materials e.g. Al_2O_3 on graphene.[18]

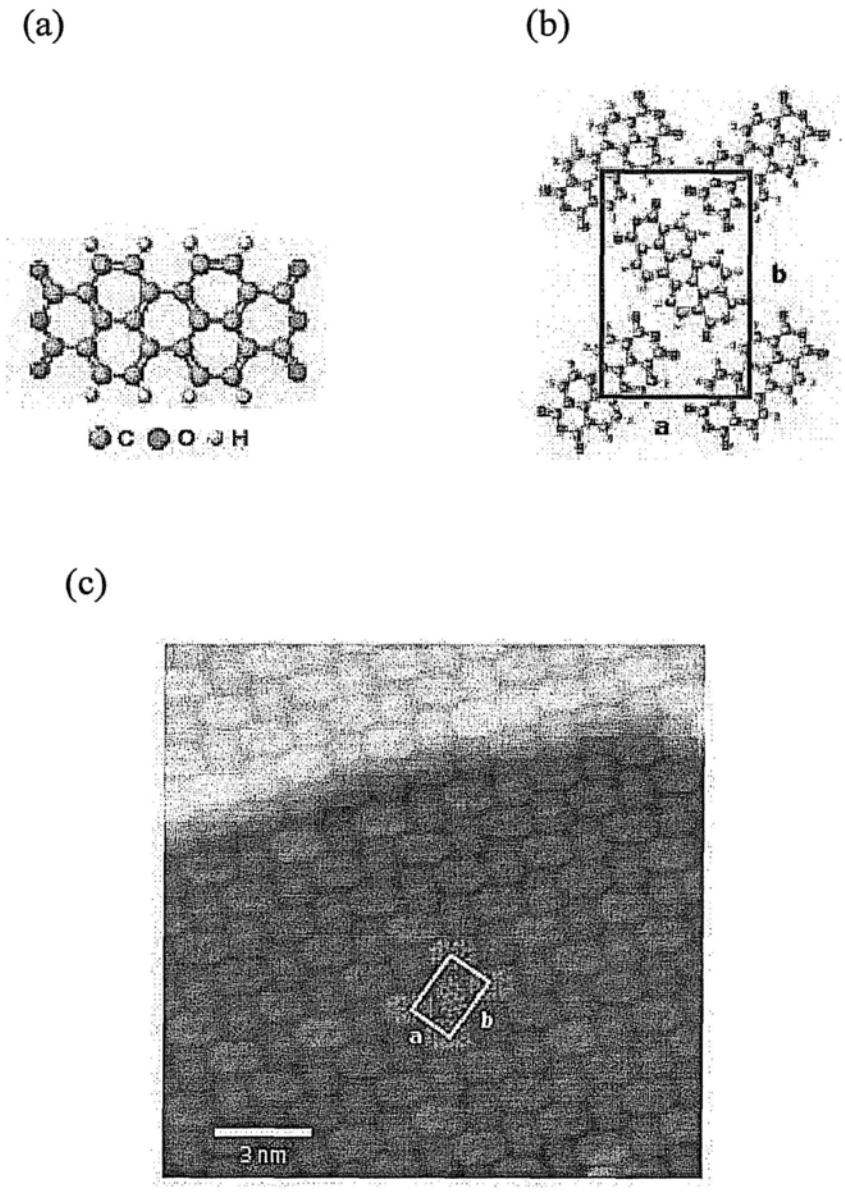

Figure 1.13 Self-assembled PTCDA monolayer on the epitaxial graphene substrate: (a) Molecular structure of PTCDA. (b) PTCDA herringbone unit cell, with the lattice vectors a and b shown. (c) Molecular-resolution STM image of the PTCDA monolayer. The PTCDA molecular structure and unit cell outline are overlaid. The monolayer continuously follows the graphene sheet over the SiC step edge. Taken from Ref. 16.

Aryl group molecules are frequently used in modification of graphene and carbon nanotube (CNT) as shown in Figure 1.14. The transport properties of epitaxial graphene (EG) on SiC substrate could be tuned from near-metallic to semiconducting as shown in Figure 1.15.[19] The aryl groups functionalized nanosheets disperse readily in polar aprotic solvents, allowing alternative avenues for simple incorporation into different polymer matrices.[20, 21] The charge transfer between aryl group and graphene

has been found in experiments.[22] However, the exact interaction mechanism between methoxyphenyl, nitrophenyl and graphene is needed to be understood at atomic scale.

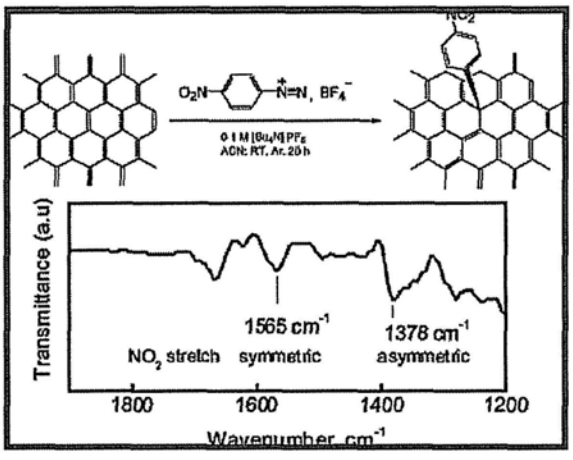

Figure 1. 14 (Top) Schematic illustration of the spontaneous grafting of aryl groups to epitaxial graphene via reduction of 4-nitrophenyl diazonium (NPD) tetrafluoroborate. (Bottom) Transmission FT-IR spectrum of NP-functionalized epitaxial graphene (EG). Taken from Ref. 19.

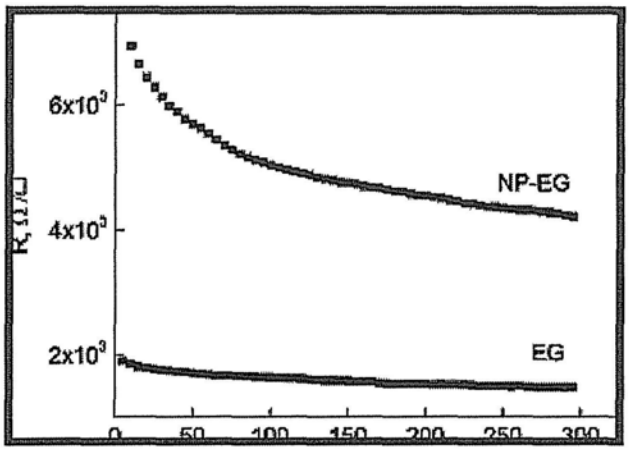

Figure 1.15 Temperature dependence of sheet resistance of pristine (EG) and nitrophenyl functionalized graphene (NP-EG) measured by the van der Pauw technique. Taken from Ref. 19.

1.2.3 Graphene Oxide

Chemically derived graphene oxide (GO) exhibits drastically different properties from pristine graphene. The functional groups such as -O-, -COOH, and –OH could modulate the electronic structure and physical properties of GO to a wide

range.[23, 24] Figure 1.16 shows the atomic structure model of GO. High resolution transmission electron microscopy (TEM) was used to characterize the atomic structure of GO, and it was found that there is in-plane and out-plane structural distortion and strain induced by Oxygen-contained functional groups. There are also pentagon-heptagon pairs in GO as shown in Figure 1.17. Chemical reduction could increase the conductivity of close-to-insulating GO by up to 4 orders of magnitude, but the conductivity of reduced graphene oxide (RGO) is lack behind that of pristine graphene by a factor of 10~100.[24] H_2 and -NH_2 group containing molecules could be used to as the reduction reactants for GO.[25, 26]

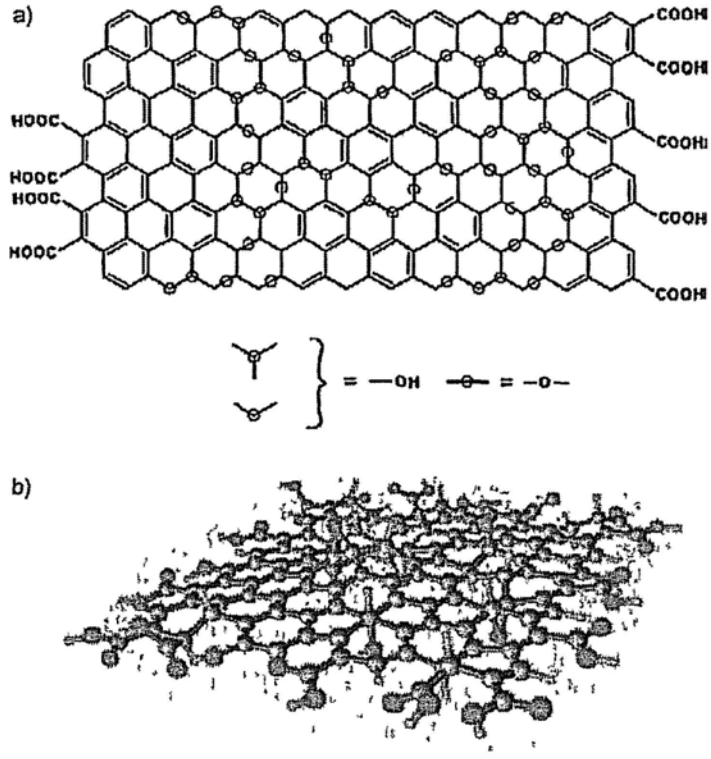

Figure 1.16 (a) Chemical structure model of GO. Position of oxygen functional groups are indicated by circles. The functional groups are attached on both sides of the graphene sheet. (b) 3D view of a GO sheet. In reality, the sheets are corrugated due to puckering caused by the functional groups. Taken from Ref. 23.

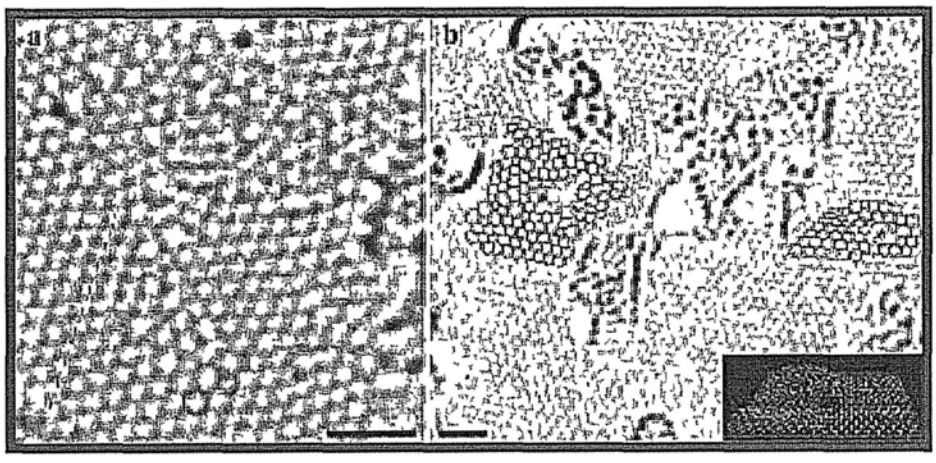

Figure 1.17 Extended topological defects and deformations in RGO. (a) Atomic resolution TEM image of a nonperiodic defect configuration. Dark contrast can be directly interpreted in terms of atomic structure. As examples, a carbon hexagon is indicated in blue, a pentagon in magenta, and a heptagon in green. (b) Partial assignment of the configurations in defective areas. Carbon pentagons, hexagons, and heptagons are indicated in magenta, blue, and green, respectively. Taken from Ref. 26.

References

(1) (a) Lucas, M.; Mai, W. J.; Yang, R.S.; Wang, Z. L.; Riedo, E. *Nano Lett* **2007**, 7, 1314-1317. (b) Wang, X.D.; Zhou, J.; Song, J.H.; Liu, J.; Xu, N.S.; Wang, Z.L. *Nano Lett* **2006,** 6, 2768-2772.

(2) Dulub, O.; Boatner, L. A.; Diebold, U. *Surface Science* **2002**, 519, 201.

(3) Kitchen, D.; Richardella, A.; Tang, J. M.; Flatté, M. E.; Yazdani, A. *Nature* **2006**, 442, 436.

(4) Dulub, O.; Boatner, L. A.; Diebold, U. *Surface Science* **2002**, 504, 271.

(5) Ozawa, K.; Sato, T.; Oba, Y.; Edamoto, K.; *J. Phys. Chem. C* **2007**, 111, 256.

(6) Halevi, B.; Vohs, J. M.; *Surface Science* **2008**, 602, 198.

(7) Bech, M.; Simonsen, J. B.; Handke, B.; Li, Z. S.; Møller, P. J. *Surface Science* **2006**, 600, 3375.

(8) Lao, C. S.; Li, Y.; Wong, C. P.; Wang, Z. L. *Nano Lett.* **2007**, **7**, 1323.

(9) Yip, H. L.; Hau, S. K.; Baek, N. S.; Ma, H.; Jen, A. K. Y. Adv. Mater. **2008**, 20, 2376.

(10) Quintanaa, M.; Marinadob, T.; Nonomurab, K.; Boschloob, G.; Hagfeldt, A. *J. Photochem. Photobiol. A* **2009**, 202, 159.

(11) Martini, C.; Poize, G.; Ferry, D.; Kanehira, D.; Yoshimoto, N.; Ackermann, J.; Fages, F.; *ChemPhysChem* **2009**, 10, 2465-2470.

(12) Oosterhout, S. D.; Wienk, M. M.; Van Bavel, S. S.; Thiedmann, R.; Koster, L. J. A.; Gilot, J.; Loos, J.; Schmidt, V.; Janssen, R. A. J.; *Nature Materials* **2009**, 8, 818– 824.

(13) Dag, S.; Wang, L. W. *Nano Lett.* **2007**, 8, 4185-4190

(14) Dong, X. C.; Fu, D. L.; Fang, W. J.; Shi, Y. M.; Chen, P.; Li, L. J. *Small* 2009, 5, 1422-1426.

(15) Chen, W.; Chen, S.; Qi, D. C.; Gao, X. Y.; Wee, A. T. S. *J. Am. Chem. Soc.* **2007**, 129, 10418-10422.

(16) Wang, Q. H.; and Hersam, M. C. *Nat. Chem.* **2009**, 1, 206.

(17) Huang, H.; Chen, S.; Gao, X. Y.; Chen, W.; and Wee, A. T. S. *Acs Nano* **2009**, 3,

3431.

(18) Wang, X. R.; Tabakman, S. M.; and Dai, H. J. *J. Am. Chem. Soc.* **2008**, 130, 8152.

(19) Bekyarova,E. ; Itkis, M. E. ; Ramesh, P. ; Berger, C. ; Sprinkle, M. ; de Heer, W. A. ; Haddon, R. C. *J. Am. Chem. Soc.* **2009**, *131*, 1336-1337.

(20) Lomeda, J. R. ; Doyle, C. D. ; Kosynkin, D. V. ; Hwang, W. F. ; Tour, J. M., *J. Am. Chem. Soc.* **2008**, *130*, 16201-16206.

(21) Park, S. J. ; Ruoff , R. S. *Nat. Nanotech.* **2009**, *4*, 217-224.

(22) Sharma, R.; Baik, J. H.; Perera, C. J.; Strano, M. S. *Nano Lett.* **2010**, *10*, 398-405.

(23) Eda, G.; Chhowalla, M. *Adv. Mater.* **2010**, *22*, 2392–2415.

(24) Go´mez-Navarro, C.; Meyer, J. C.; Sundaram, R. S.; Chuvilin, A.; Kurasch, S.; Burghard, M.; Kern, K.; Kaiser, U. *Nano Lett.* **2010**, *10*, 1144–1148

(25) Li, X. L.; Zhang, G. U.; Bai, X. D.; Sun, X. M.; Wang, X. R.; Wang, E. G.; Dai, H. J. *Nat. Nanotech.* **2008**, *3*, 538-542.

(26) Compton, O. C.; Dikin, D. A.; Putz, K. W.; Brinson, L. C.; Nguyen, S. B. T. *Adv. Mater.* **2010**, *22*, 892–896

Chapter 2 Introduction to Density Functional Theory

2.1 Many-Particle Hamiltonian

To study and calculate the properties of atomic and molecular systems, Quantum Mechanics is a necessary tool. The Schrödinger Equation plays the central role in Quantum Mechanics, as Newton's laws in classical mechanics. For the characterizing the electronic structure of a many-particle with the interaction of a time dependent potential, the full time dependent Schrödinger Equation is needed to be solved as shown in E.q.(1).

$$ih\frac{\partial\psi(r,t)}{\partial t} = H\psi(r,t) \qquad (2\text{-}1\text{-}1)$$

If the potential is time-independent, the wavefunction solution $\psi(r,t)$ has the following formula:

$$\psi(r,t) = \psi(r)f(t) \qquad (2\text{-}1\text{-}2)$$

By E.q.(2), spatial and temporal variables of $\psi(r,t)$ are separated. Then Schrödinger Equation has the time-independent expression:

$$H\psi(r) = E\psi(r) \qquad (2\text{-}1\text{-}3)$$

The above time-independent E.q.(2) is frequently used and very important in computational material sciences. For a many-particle system, the Hamiltonian could be described as

$$H = T_n + U_{nn} + U_{ext} + T_e + U_{ee} \qquad (2\text{-}1\text{-}4)$$

where the kinetic and potential energies of nuclei and electrons are given by,

$$T_n = \sum_{\mu} -\frac{1}{2M_\mu}\nabla_\mu^2 \qquad (2\text{-}1\text{-}5)$$

$$U_{nn} = \sum_{\mu<\nu} \frac{Z_\mu Z_\nu}{|R_\mu - R_\nu|} \qquad (2\text{-}1\text{-}6)$$

$$U_{ext} = \sum_i \left(\sum_\mu \frac{-Z_\mu}{|r_i - R_\mu|} \right) \qquad (2\text{-}1\text{-}7)$$

$$T_e = \sum_i -\frac{1}{2m}\nabla_i^2 \qquad (2\text{-}1\text{-}8)$$

$$U_{ee} = \sum_{i<j} \frac{1}{|r_i - r_{j|}|} \qquad (2\text{-}1\text{-}9)$$

2.2 Born-Oppenheimer Approximation

To exactly solve the many-particle E.q. (2-1-3) is an impossible task, so reasonable approximations are needed to accompany the computational capability. The adiabatic Born-Oppenheimer approximation [1] which relies on the significant difference between the mass of the electrons and those of ions brings the first simplication. The scientific error is estimated by (m/M)1/4, where m and M are the mass of electron and nuclear separately. In this picture, the nuclei of the system are seen as fixed, generating a static external potential U_{ext} in which the electrons are moving. The total wave function in Eq. (2-1-3) can then be separated into the product of a nuclear part and an electronic part as (2-2-1) and the Hamiltonian can be rewritten as (2-2-2).

$$\psi(R,r) = \psi_{nucl}(R)\psi_{elec}(r) \qquad (2\text{-}2\text{-}1)$$

$$H = H_{nucl} + H_{elec} \qquad (2\text{-}2\text{-}2)$$

From E.q. (2-1-4), the electrons Hamiltonian could be separated as

$$H_{el} = T_e + U_{ext} + U_{ee} = \sum_i h_i + U_{ee} \qquad (2\text{-}2\text{-}3)$$

The problem has therefore been simplified to a system of electrons interacting

with each other in the external potential U_{ext} generated by the nuclei and a stationary electronic state is described by the wavefunction $\psi_{elec}(r)$ satisfying the many-electron Schrödinger equation:

$$H_{elec}\psi_{elec}(r) = E_{elec}\psi_{elec}(r) \qquad (2\text{-}2\text{-}4)$$

The many-electron wavefunction could be expressed as

$$\psi_{elec}(r) = \psi_1(r_1)\psi_2(r_2)\cdots\psi_n(r_n) \qquad (2\text{-}2\text{-}5)$$

Eq. (2-2-5) is named as Hartree wavefunction.

2.3 Hartree-Fock Method

In wavefunction based methods, the simplest treatment with useable accuracy is the Hartree-Fock method. In this method, one assumes that the wavefunction can be written as the antisymmetric sum of products of single-electron wave functions (a Slater determinant) to satisfy the Pauli exclusion principle and electron asymmetric exchange. Then the many-electron wavefunction is in the following formula:

$$\psi_{HF} = \frac{1}{\sqrt{N}}\begin{vmatrix} x_1(r_1)x_2(r_1)\cdots x_n(r_1) \\ x_1(r_2)x_2(r_2)\cdots x_n(r_2) \\ \vdots \\ x_1(r_n)x_2(r_n)\cdots x_n(r_n) \end{vmatrix} \qquad (2\text{-}3\text{-}1)$$

2.4 Density Functional Theory (DFT)

2.4.1 Hohenberg-Kohn Theorems

Density functional theory (DFT) is a method to study and predict the observables of the many-particle system in a simpler and easier way. Single-electron approximation was proposed based on DFT.[2] The properties of a many-body system

could be expressed as a functional of electron density $\rho(r)$, which originates from Thomas-Fermi's spirit.[3-4] The density $\rho(r)$ being a function of only three variables *x*, *y*, and *z*, it is a much simpler variable to deal with than the many-body wave function depending on $3N$ variables (where N is the number of electrons in the system). Hohenberg-Kohn theorem can be summarized in two points as follows:

1) The external potential and hence the total energy E is a unique functional of the electron density $\rho(r)$

Proof: Prove by contradiction. Assume that there exist two different external potentials $v_1(r)$ and $v_2(r)[v_2(r) \neq v_2(r) + const.]$, which both give the same electron density $\rho(r)$. Then we have two Hamiltonians, H_1 and H_2 with the same ground state density $\rho(r)$ and different Φ_1 and Φ_2. Then we have:

$$E_1 = <\Phi_1 | H_1 | \Phi_1> = \int v_1(r)\rho(r)dr + <\Phi_1 | T+U | \Phi_1> \qquad (2\text{-}4\text{-}1)$$

$$E_2 = <\Phi_2 | H_2 | \Phi_2> = \int v_2(r)\rho(r)dr + <\Phi_2 | T+U | \Phi_2> \qquad (2\text{-}4\text{-}2)$$

Now we use the variational principle, taking Φ_2 as a trial function for the H Hamiltonian, to obtain:

$$\begin{aligned} E_1 &< \langle \Phi_2 | H_1 | \Phi_2 \rangle = \int v_1(r)\rho(r)dr + \langle \Phi_2 | T+U | \Phi_2 \rangle \\ &= E_2 + \int [v_1(r) - v_2(r)]\rho(r)dr \end{aligned} \qquad (2\text{-}4\text{-}3)$$

In addition, we can take the Φ_2 as a trial function for the H_2 Hamiltonian, to obtain:

$$E_2 < \langle \Phi_1 | H_2 | \Phi_1 \rangle = E_1 + \int [v_2(r) - v_1(r)]\rho(r)dr \qquad (2\text{-}4\text{-}4)$$

When we add the above two equations, we then obtain the contradiction:

$$E_1 + E_2 < E_1 + E_2 \qquad (2\text{-}4\text{-}5)$$

Thus we conclude that there exists an unique map between the external potential $v_1(r)$ and the ground state density $\rho(r)$. This implies that all the energies, including the total energy, is a functional of the density. We write this as $E = E[\rho(r)]$. The density determines the Hamiltonian, and thereby, the wavefunction.

2) The ground-state energy E can be obtained variationally, and the density $\rho^0(r)$ that minimizes the total energy is the exact ground-state density

Proof: Suppose we have a trial density $\rho'(r)$. Then this density defines its own wavefunction Φ', and the expectation value of the true Hamiltonian satisfies the variational principle

$$\begin{aligned} E &= <\Phi'|H|\Phi'> = \int v'(r)\rho'(r)dr + <\Phi'|T+U|\Phi'> \\ &= E[\rho'(r)] \geq E[\rho^0(r)] = <\Phi^0|H|\Phi^0> \end{aligned} \qquad (2\text{-}4\text{-}6)$$

Thus, the correct density is the one that produces the minimum energy.

2.4.2 Kohn-Sham Method

The total energy of many-electron system could be expressed generally by a functional of electronic density $\rho(r)$ as:

$$E[\rho] = T_e[\rho] + U_{ext}[\rho] + U_{ee}[\rho] \qquad (2\text{-}4\text{-}7)$$

where $U_{ext}[\rho]$ is an effective Kohn-Sham single particle potential.

Kohn and Sham revised the above expression as:

$$E[\rho] = T_0[\rho] + U_{ext}[\rho] + E_{cl}[\rho] + E_{xc}[\rho] \qquad (2\text{-}4\text{-}8)$$

where $E_{xc}[\rho]$ is exchange energy and $E_{cl}[\rho]$ is correlation energy.

The $E_{xc}[\rho]$ and $E_{cl}[\rho]$ are contributed from:

1) Non equal kinetic energy: $T_e[\rho] \neq T_0[\rho]$ (2-4-9)

2) Exchange energy and self-interaction correction: $U_{ee} \neq E_{cl} + \cdots$ (2-4-10)

3) Correlation energy by: $\Psi(r_1,...r_n) \neq \prod_p \phi_{p1}(r_1)...\phi_{p1}(r_1)$ (2-4-11)

2.4.3 Kohn-Sham Equation

The variation of the total energy leads to:

$$\delta\Omega[\{\Phi_i(r)\}] = 0 \qquad (2\text{-}4\text{-}12)$$

$$\Omega[\{\Phi_i(r)\}] = E[\rho] - \sum_{i,j}(\varepsilon_{ij}(\int \Phi_i^*(r)\Phi_i(r)dr - \delta_{ij}) \qquad (2\text{-}4\text{-}13)$$

$$\rho(r) = \sum_{i=1} \Phi_i^*(r)\Phi_i(r) \qquad (2\text{-}4\text{-}14)$$

Finally, we could attain the Kohn-Sham equation:

$$[\frac{1}{2}\nabla_i^2 + V_{eff}(r)]\Phi_i^{KS}(r) = \varepsilon_i \Phi_i^{KS}(r) \qquad (2\text{-}4\text{-}15)$$

$$V_{eff}(r) = V_{ext}(r) + U_{cl}(r) + V_{xc}(r) \qquad (2\text{-}4\text{-}16)$$

2.4.4 Solution of Kohn-Sham Equation

Now we must apply the variational principle and the variables to be adjusted are the KS orbitals themselves. In practice, this is done just like in the HF method, a basis set expansion is used to represent the KS orbitals. Thus, similar computational engines are required for both DFT and HF theory. We write the entire energy functional in terms of the KS orbitals:

$$[\frac{1}{2}\nabla_i^2 + V_{eff}(r)]\Phi_i^{KS}(r) = \varepsilon_i \Phi_i^{KS}(r) \qquad (2\text{-}4\text{-}17)$$

The solution must be obtained by iterative methods until self-consistence is achieved (SCF):

$$\rho_0(r) \rightarrow V_{eff}(r) \rightarrow \Phi_i^{KS}(r) \rightarrow \rho(r) \rightarrow V_{eff}(r) \rightarrow \Phi_i^{KS}(r) \rightarrow \ldots \quad (2\text{-}4\text{-}18)$$

2.5 Electron Density Approximation

2.5.1 Local Density Approximation (LDA)

The simplest approximation to the $E_{xc}[\rho]$ is the local density approximation (LDA) by using the local form of the exchange-correlation of a uniform electron gas. This approximation was first suggested by Slater in 1951,[5] and later introduced into DFT by Kohn and Sham.[2] The LDA exchange-correlation energy is given by:

$$E_{xc}^{LDA}[\rho] = \int \rho(\vec{r}) \varepsilon_{xc}(\rho(\vec{r})) d\vec{r} \qquad (2\text{-}5\text{-}1)$$

$$\varepsilon_{xc}(\rho(\vec{r})) = \varepsilon_x(\rho(\vec{r})) + \varepsilon_c(\rho(\vec{r})) \qquad (2\text{-}5\text{-}2)$$

where $\varepsilon_x(\rho(\vec{r})) = -\frac{3}{4}\left(\frac{3\rho((\vec{r}))}{\pi}\right)^{1/3}$ is the Dirac/Slater Exchange energy of the gas. The Coulomb correlation piece is obtained from interpolations of the Monte Carlo data of Ceperly and Alder.[6] The typical LDA approximation is the SWVN implementation that implies Slater Exchange plus Coulomb correlation obtained by Vosko, Wilk and Nussair[7] as follows:

Exchange energy:

$$\varepsilon_x[r_s] = -\frac{0.9164}{r_s}$$

Correlation energy:

$$\varepsilon_c^{LDA}(r_s) = \begin{cases} -0.2846/(1+1.0529\sqrt{r_s}+0.3334 r_s) & \text{if } r_s \geq 1 \\ -0.0960 + 0.0622 \ln r_s - 0.0232 r_s + 0.0040 r_s \ln r_s & \text{if } r_s \leq 1 \end{cases}$$

where $r_s = [\frac{3}{4\pi\rho(r)}]^{\frac{1}{3}}$ is the Weigner-Seitz radius.

For core electrons, r_s is smaller than 1, and 1~6 for valence electrons. The

LDA by its self does not contain sufficient accuracy for chemical applications. It is necessary to include terms that explicitly take into account the spatial variation of the density. LDA holds for slowly varying systems and could be questionable when applied to atoms, molecules, and solids. However, LDA gives surprisingly good results1 compared to experiment.[8] The application of LDA to a large variety of systems was shown to reproduce satisfactorily many physical quantities such as ground-state atomic structures and vibrational properties of molecules and solids.[9]

2.5.2 Generalized Gradient Approximation (GGA)

Although LDA shows great success in many systems, it overestimates the cohesive energy. Improvement over LDA has been developed in recent years by considering the correction of density gradient. More explicitly, the exchange-correlation functional can be formally written as:

$$E_x^{CGA} = E_x^{LDA} - \sum_{\sigma} F(s_\sigma)\rho_\sigma^{4/3}(\vec{r})d\vec{r} \qquad (2\text{-}5\text{-}3)$$

$$s_\sigma = \frac{|\nabla\rho|}{\rho_\sigma^{4/3}} \qquad (3\text{-}10\text{-}2)$$

Two frequently used choices for the exchange functional are:

Becke form [10]: $F^{B88} = \frac{\beta s_\sigma}{1+6\beta s_\sigma Sinh^{-1}(s_\sigma)}$ (2-5-4)

Perdew form [11]: $F^{P86} = \left(1+1.296x^2+14x^4+0.2x^6\right)^{1/15}$ (2-5-5)

$$x = \frac{s_\sigma}{(24\pi^2)^{1/3}} \qquad (2\text{-}5\text{-}6)$$

The β parameter in the Becke form is a fit to accurate densities of a large number of atoms, while the Perdew form does not have any empirical parameters. Typical combinations in common use give rise to the functionals and the commonly used forms include Becke,[10] Perdew-Wang 91[11] and its simplified version PBE[12], and

BLYP.[13] Calculations show that GGA usually provides improvements on accuracy over LDA. For the bcc Fe, it gives the correct ferromagnetic ground state. For transitional metal oxides FeO and CoO, it gives the qualitative results, while LDA give wrong results. But GGA isn't better than LDA for all cases, and sometimes it's overdone.

2.5.3 Hybrid Functionals

The HF method could cause a systematic error, and the lack of Coulomb correlation implies that the energies are higher than they should be. Thus a combination of the HF (exact) exchange and the functional Coulomb exchange-correlation could improve things considerably. Hybrid functionals are of this kind. The popular B3LYP functional is the prime example of this kind.[14] This functional has the following form:

$$E_{XC} = E_{XC}^{LSDA} + a_0(E_X^{exact} - E_X^{LSDA}) + a_X \Delta E_X^{B88} + a_C \Delta E_C^{PW91} \quad (2\text{-}5\text{-}7)$$

where a_0=0.20, a_x=0.72, and a_c=0.81, and they are determined empirically.

2.6 Plane Waves Expansion

In order to solve Kahn-sham equations, another feature must be specified. Namely, a suitable basis set must be chosen for the expansion of the Kohn-Sham orbitals. For the case of an infinitely extended crystal, by employing a cell-based approach and Born-von-K´arm´an periodic boundary conditions, plane waves of the form

$\psi_k(r) \propto e^{ik \cdot r}$ with the wave vector k fulfilling Bloch theorem

$\psi_k(r + R) = e^{(ik \cdot R)} \psi_k(r)$ for every lattice vector R are employed. The periodicity allows one to describe the crystal by considering only one unit cell and to expand the Kohn-Sham orbitals in a Fourier series:

$$\psi_i(r) = \psi_{n,k} = \frac{1}{\sqrt{\Omega}} \sum_G c_n(k+G) e^{i(K+G)\cdot r} \qquad (2\text{-}6\text{-}1)$$

where the sum extends over the reciprocal lattice vectors G, and Ω is the volume of the unit cell. Then, the electronic structure is characterized by the band index n and the wave vector k restricted to the first Brillouin zone.

The representation of the Kohn-Sham wave functions in the form of Eq. (2-6-1) allows for an easy control of the convergence behaviour by systematically increasing the number of Fourier coefficients G. For Γ point sampling, the number of wavefunctions used is controlled by the largest wave vector G_{max} in the Fourier expansion which fixes the energy cutoff as $E_{cut} = \hbar^2 |G_{max}|^2 / 2m_e$. Other advantages of using a plane wave formulation are that the same basis set can be used for all atomic species and that plane waves do not depend on nuclear positions so that correction terms are not needed for the calculation of forces, unlike in the case of localized basis sets.[15]

The plane wave basis set formulation can also be applied to a non-periodic system. The system is then placed at the centre of a periodic supercell. If the supercell is large enough the interactions between systems in neighbouring cells become negligible.

2.7 Pseudopotentials

The electronic structure of an atom consists of core states and valence states. The inner orbitals are tightly bound to the nucleus and hardly influenced by the interaction with neighbouring species while the outer electrons lay at higher energies and are almost entirely responsible for the bonding properties of the system. Based on these properties, pseudopotentials (PPs) were introduced to simplify electronic calculations by replacing the nucleus and the "frozen" core with their combined effective influence on the valence electrons. The pseudopotentials used in this thesis are norm-conserving[16] and fulfill the following requirements:

1) The ground-state pseudo valence eigenvalues match exactly the all-electron (AE) values;

2) The pseudo wavefunctions and the AE orbitals are identical beyond a chosen core radius r_c;

3) The integrals from 0 to r of the AE and pseudo charge densities agree for $r > r_c$ for each valence state (norm conservation);

4) The logarithmic derivatives of the AE and pseudo wavefunctions, and their first energy derivatives agree for $r > r_c$.

The norm-conservation of the charge is an essential requisite for the accuracy of the pseudopotential and must be imposed to each angular momentum wave. To achieve high accuracy norm-conserving PPs are non-local, i.e. they contain a term which depends on the angular momentum of the wavefunction they act on. They can be written as

$$V^{PP}(r) = \sum_{lm} |lm\rangle V_l(r) \langle lm| \qquad (2\text{-}7\text{-}1)$$

where the $|lm\rangle$ are spherical harmonics, and $V_l(r)$ is the pseudopotential for angular momentum l. This formulation is expensive as the evaluation of Eq. (2-7-1) requires $N_{pw}N_k(N_{pw} + 1)/2$ projectors to be calculated for each angular momentum component l, where N_{pw} is the number of plane waves in the expansion and N_k is the number of points in the Brillouin zone.

In the Kleinman-Bylander form,[17] this semi-local form is replaced by a fully separable non-local formulation:

$$V^{PP} = V^{local} + \sum_{lm} \frac{|\psi_{lm}\delta V_l\rangle \langle \delta V_l \psi_{lm}|}{\langle {}_l\psi_{lm} | \delta V | \psi_{lml}\rangle} \qquad (2\text{-}7\text{-}2)$$

where V^{local} is an arbitrary local potential, ψ_{lm} are the pseudo wave functions for a reference state, and δV_l is defined through

$$\delta V = V_l - V^{local} \qquad (2\text{-}7\text{-}3)$$

where V_l is the l angular momentum component of the pseudopotential in its semi-local form [Eq. (2-7-1)]. Writing the pseudopotential in this form allows the

number of integrals of V^{PP} for an energy-band calculation to be reduced to $N_{pw}N_k$. The treatment of original wavefunctions and potential to pseudo-wavefunctions PP is illustrated in Figure 2.1.

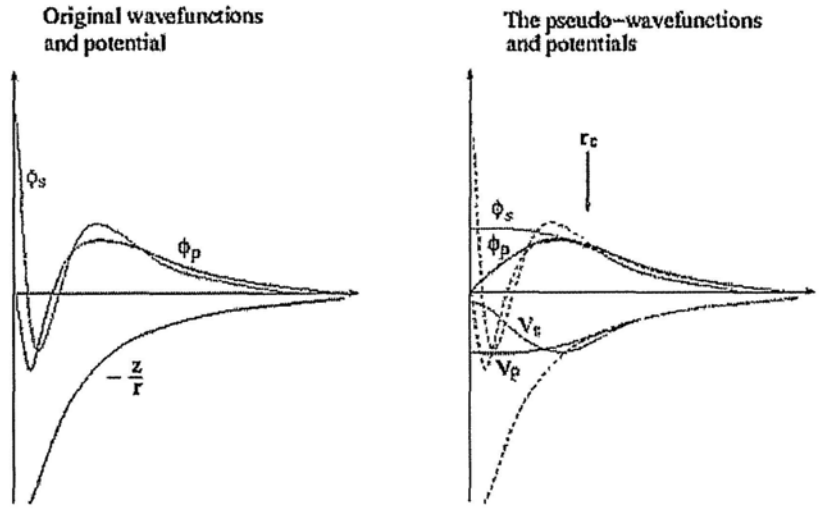

Figure 2.1 The principle of PP.

It is not a trivial task to construct pseudopotentials because they are nonlocal and depend on real eigenvalues. Efficient approaches include empirical methods by fitting to experimental data, semi-empirical model pseudopotentials, and *ab initio* norm-conserving pseudopotentials. The latter reproduce the full wavefunctions in the region $r > r_c$ and real charge densities in the whole space. Although they have a good transferability, they need high energy cutoff for planewaves due to their locality.

2.7.1 Ultrasoft Pseudopotentials (USPP)

In 1990, Vanderbilt proposed the norm conservation criteria to obtain smoother pseudo wave functions, named ultrasoft pseudopotentials (USPP).[18] This can be done by splitting the pseudo wave functions into two parts:

1) Ultrasoftvalence wave function that do not fulfill the norm conservation criteria:

$$\varphi_i^{US}(r) \quad \left(\int_0^{r_c} \left| \varphi_i^{US}(r)^2 \right| \neq \int_0^{r_c} \left| \varphi_i^{AE}(r)^2 \right| \right)$$

2) A core augmentation charge (charge deficit in the core region):

$$Q_{nm}(r) = \psi^{AE}{}_n{}^*(r)\psi^{AE}{}_m(r) - \varphi^{US}{}_n{}^*(r)\varphi^{US}{}_m(r)$$

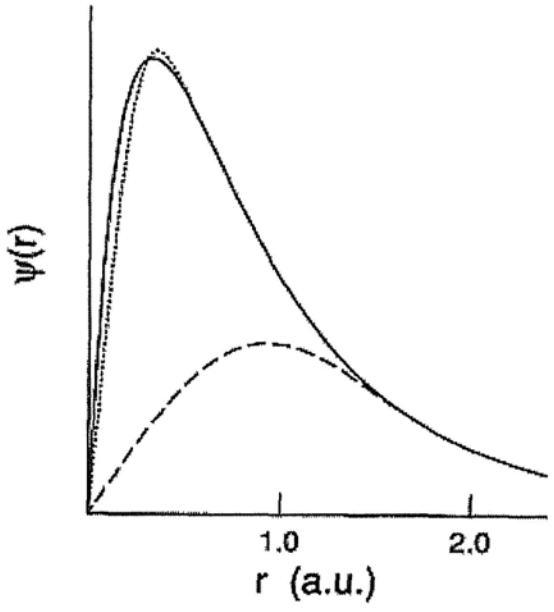

Figure 2.2 Oxygen 2*p* radial wave function (solid line), and corresponding norm-conserving.

The comparison of O 2*p* pseudo-wave-functions (HSC)[16] (dotted line), and ultra soft pseudo-wave-functions[18] are shown in Figure 2.2. With this processing method, the pseudo-wave-functions are as soft as possible within the core region, and this method could robustly decrease the cut off of kinetic energy and considerably fewer plane-waves for the attained calculation accuracy. USPP is efficient on applications of first-row and transitional metal systems.

2.7.2 Projector Augmented Wave Potentials (PAW)

The PAW method was supposed by by Blöchl in 1994,[19] which generalizes both the pseudopotential method and the linear augmented-plane-wave (LAPW) method in a natural way. The PAW method allows high-quality first-principles

molecular-dynamics calculations to be performed using the original fictitious Lagrangian approach of Car and Parrinello. Like the LAPW method it can be used to treat first-row and transition-metal elements with affordable effort and provides access to the full wave function. The augmentation procedure is generalized in that partial-wave expansions are not determined by the value and the derivative of the envelope function at some muffin-tin radius, but rather by the overlap with localized projector functions. The pseudopotential approach based on generalized separable pseudopotentials can be regained by a simple approximation. The principle of PAW is shown in Figure 2.3. The differences between USPP and PAW potentials are:

1) USPP use plane wave cutoff for the density equivalent to that of norm-conserving pseudopotentials support grids required.

2) PAW uses one-center expansions with radial grids and a smooth compensation density lower cutoff for the density than USPP.

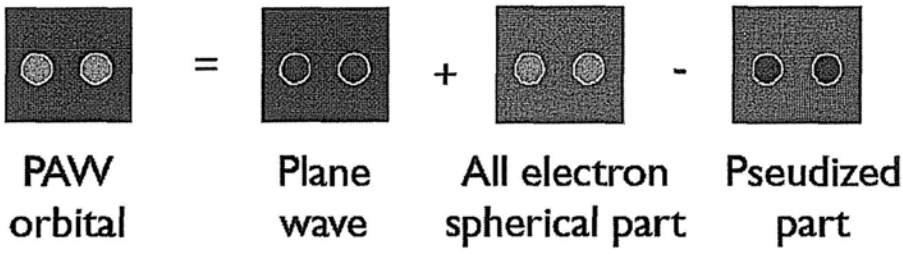

Figure 2.3 Principle of PAW method.

Outside the core, the wave functions are represented by plane wave, and inside the core, the wave functions are atomic like. The retained atomic like part permits the application of DFT+U as introduced in next section.

2.8 DFT+U

Conventional density functional theory DFT often fails to describe the Hamiltonian with strong localized *d* or *f* electrons.[20,21] Large errors in the intra-atomic Coulomb (U) and exchange interactions (J) are the source of this failure. The DFT+U

method takes into account orbital dependence of the U and J which is absent in the DFT. As in DFT+U scheme, the Hamiltonian could be separated into three subsystems:

1) Delocalized *s* and *p* electrons which could be described by using an orbital-independent one-electron potential (LDA).
2) Localized *d* or *f* electrons for which the Coulomb *d-d* (*f-f*) interaction should be taken into account by a local Coulomb interaction term minus a Hund's rule coupling
3) Double counting correction term, because we have added explicitly the Hubbard term as in term 2, we have to correct the energy contribution of *d* or *f* orbitals, which are included in the LDA functional in order not to count twice their contributions.

The Hamiltonian of DFT+U scheme is described by the following equation:

$$\hat{\mathcal{H}} = \underbrace{\sum_{\mathbf{k}lml'm'\sigma} \epsilon_{lml'm'}(\mathbf{k})\, \hat{c}^{\dagger}_{\mathbf{k}lm\sigma}\, \hat{c}_{\mathbf{k}l'm'\sigma}}_{\text{LDA}} + \underbrace{\sum_{\substack{i=i_d,\\ l=l_d}} \sum_{m\sigma,m'\sigma'}{}' \frac{U^{\sigma\sigma'}_{mm'}}{2} \hat{n}_{ilm\sigma}\hat{n}_{ilm'\sigma'}}_{\text{local Coulomb interaction}}$$

$$\underbrace{-\sum_{\substack{i=i_d,\\ l=l_d}} \sum_{m\sigma,m'\sigma'}{}' J_{mm'} \hat{c}^{\dagger}_{ilm\sigma}\hat{c}^{\dagger}_{ilm'\sigma'}\hat{c}_{ilm'\sigma}\hat{c}_{ilm\sigma'}}_{\text{Hund's rule coupling}} - \underbrace{\Delta\hat{H}^{U}_{\text{LDA}}}_{\text{double counting corr.}}$$

(2-8-1)

References

(1) Born, M.; Huang, K. *Dynamical theory of crystal lattices.* Oxford: Oxford University Press, **1954**

(2) Kohn, W.; Sham, L. J. *Phys. Rev. B* **1965**, *140*, 1133-1138.

(3) Tomas, H. *Proc. Camb. Phil. Soc.* **1927**, *23*, 542

(4) Fermi, E. *Naz. Lincei.* 1927, ***6***, 602

(5) Slater, J. C. *Phys. Rev.* **1951**, *81*, 385-390.

(6) Caperley, D. M.; Alder, B. J. *Phys. Rev. Lett.* **1980**, *45*, 566-569.

(7) Perdew, T. P.; Zunger, A. *Phys. Rev. B* **1981**, *23*, 5048-5079.

(8) Jones, R. O.; Gunnarsson, O. *Rev. Mod. Phys.* **1989**, *61*, 689-746.

(9) Becke, A. D. *Phys. Rev. A* **1988**, *38*, 3098-3100.

(10) Perdew, J. P. *Phys. Rev. B* **1986**, *33*, 8822–8824.

(11) Perdew, J. P.; Chevary, J. A.; Vosko, S. H.; Jackson, K. A.; Pederson, M. R.; Singh, D. J.; Fiolhais, C. *Phys. Rev. B* **1992**, *46*, 6671-6678.

(12) Perdew, J. P.; Burke, K.; Ernzerhof, M. *Phys. Rev. Lett.* **1996**, *77*, 3865-3868.

(13) Lee, C.; Yang, W.; Parr, R. C. *Phys. Rev. B* **1988**, *37*, 785-789.

(14) Becke, A, D. *J. Chem. Phys.* **1993**, *98*, 5648–5652.

(15) Pulay, P. *Molec. Phys.* **1969**, *19*, 197.

(16) Hamann, D. R.; Schl ¨uter, M.; Chiang, C. *Phys. Rev. Lett.* **1979**, *43*, 1494-1497.

(17) Kleinman, L.; Bylander, D. M. *Phys. Rev. Lett.* 1982, *48*, 1425-1428.

(18) Vanderbilt, D. *Phys. Rev. B* **1990**, *41*, 7892-7895.

(19) Blöchl, P. E. *Phys. Rev. B* **1994**, *50*, 17953-17979.

(20) Nicholas J. Mosey and Emily A. Carter, Phys. Rev. B **2007**, *76*, 155123-155135.

(21) Anisimov, V. I. *J. Phys.: Condens. Matter* **1997**, *9* 767.

Chapter 3 Controllable Modulation of Electronic Structure of ZnO(10$\bar{1}$0) Surface by Carboxylic Acids

3. 1 Introduction

Functionalization of semiconductor surfaces by organic molecule is a promising route for the development of hybrid organic-inorganic devices and molecular nanostructures. The interface electronic structure between covalently attached organic layers and inorganic substrate was envisioned controllable by tuning the chemical type and composition of organic molecules.[1,2] The electronic structure of organic molecules adsorbed on surfaces has been frequently investigated by scanning tunneling microscopy and spectroscopy (STM and STS).

Zinc oxide has attracted a significant amount of attention in the past several years since this wide band gap semiconductor is found to have a number of potential applications in catalysis, solar cells, gas sensors, light emitting diodes (LEDs), diluted magnetic semiconductors (DMSs) and microelectronic devices. The low-index non-polar ZnO(10$\bar{1}$0) and (2$\bar{1}$ $\bar{1}$0) surfaces are of great interest, because they make industrial applications more favorable. Zn-O mixed (10$\bar{1}$0) and (2$\bar{1}$ $\bar{1}$0) surfaces also appear naturally as the majority surfaces of experimentally synthesized ZnO nanoparticles, nanobelts, nanowires and nanorods, since these nanostructures mainly grow along <0001> direction, (10$\bar{1}$0) and (2$\bar{1}$ $\bar{1}$0) appear as the major surfaces.[3] The surface energy of ZnO(10$\bar{1}$0) (2.3 J/m^2) is smaller than that of ZnO(2$\bar{1}$ $\bar{1}$0) (2.5 J/m^2) and those of polar surfaces ZnO(0001)-Zn and ZnO(000$\bar{1}$)-O (4.0 J/m^2), which make self-compensated (10$\bar{1}$0) surface most stable.[4] M-nonpolar ZnO(10$\bar{1}$0) was also used as the substrate without template for the growth of quantum structure in which large anisotropy of conductivity was found.[5]

Dye treated ZnO has been explored to the application of solar cells, due to its

abundance of charge carriers. Using organic molecule dye sensitized ZnO solar cell, high incident photon-to-current conversion efficiency up to 70% were obtained.[6] Besides photovoltaic properties of organic molecule treated ZnO, the electronic transport properties of ZnO nano-structures could also be tuned by organic molecule functionalization.[7] Carboxylic acids functionalization of ZnO surface is shown in Figure 3.1.

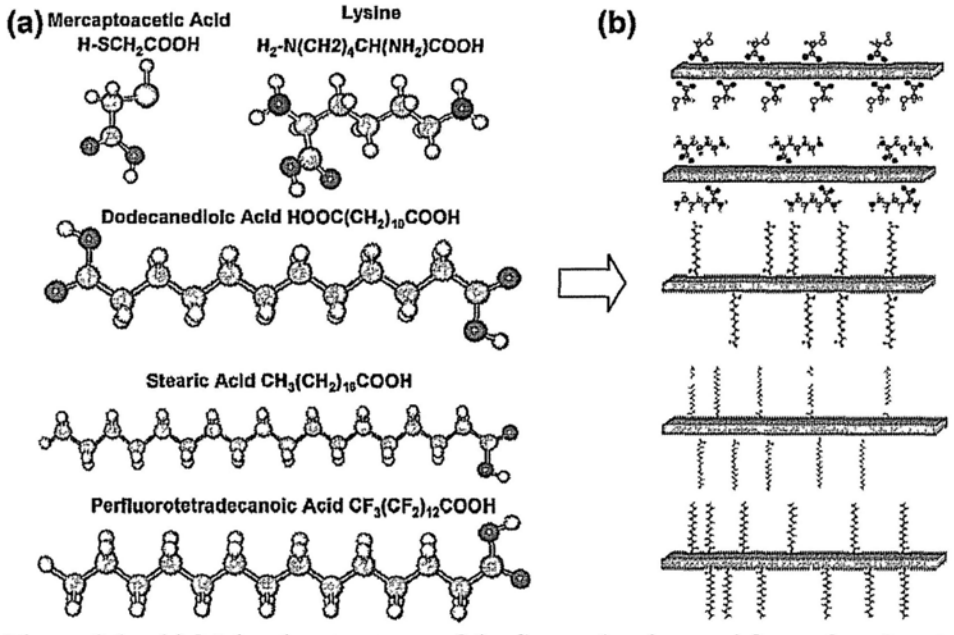

Figure 3.1 (a) Molecular structures of the five molecules used for surface functionalization. (b) Schematic models of the molecule-functionalized ZnO NBs.Taken from Ref. 7.

Carboxylic group (–COOH) is one of the frequently used anchor groups in the biosensor and materials surface functionalization. The adsorption of –COOH on semiconductor surface is able to enhance the electron injection into the conduction band. Ref. 7 has reported the experimental findings of conductivity and photoconductivity enhancement of ZnO by carboxylic group anchored molecule functionalization.

Mercapto-acetic acid molecule, with two functional groups: –COOH and –SH, is selected as the major molecule for this investigation. –COOH is normally used as the anchor for molecule's chemical bonding with semiconductor surface, while –SH is frequently used as the anchor for molecule with metal electrodes such as Au, Ag, and

Cu, so that the interface between ZnO and Au can be tuned from a Schotcky contact to an Ohmic contact.[7] Besides the role of anchoring electrode, –SH itself can also affect the interfacial electronic structure between molecule and semiconductor. The coverage effects are also investigated. The interfacial electronic structures between acetic acid, benzoic acid, 9-Anthracenecarboxylic acid and ZnO($10\bar{1}0$) are calculated to check the influence of the tail and chemical composition. The transport properties of various types of carboxylic acids functionalized ZnO NB are shown in Figure 3.2.

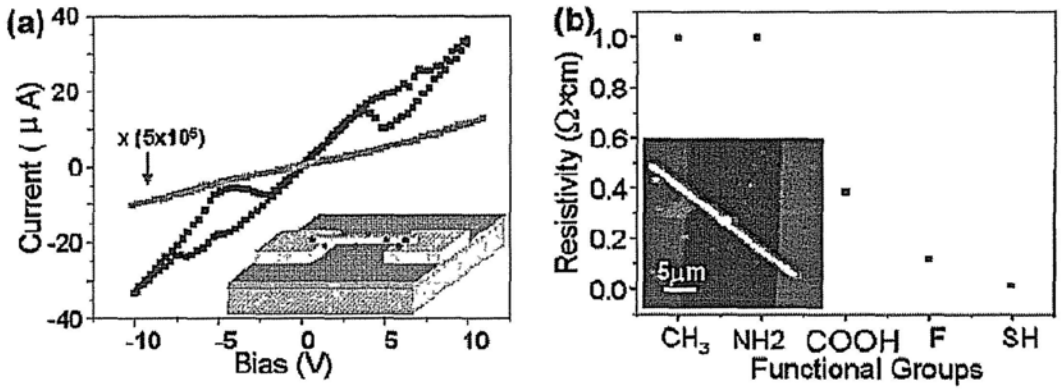

Figure 3.2 (a) *I-V* characteristics of a ZnO NB functionalized with the self-assembled thin molecule layer, HOOC(CH2)10COOH (black line), and an untreated ZnO NB sample (green line). The current of the untreated NB is magnified by 5×10^5 times for comparison purpose. Note: no Pt was deposited at the contacts so that the measured current for the untreated NB is low. Inset is a schematic view of the nanobelt device. (b) Resistivity of the NBs coated with different molecules. The lower inset image is an AFM image of a coated NB lying across two electrodes. Taken from Ref. 7.

3. 2 Calculation Methods

Here, we use state of the art first principles technique to investigate the interactions between a series of carboxylic acid molecules and ZnO($10\bar{1}0$) single crystalline surface. The calculations are performed within *Vienna ab initio simulation package* (VASP).[8] The PW91 general gradient approximation (GGA) is used.[9, 10] The electron-ion interaction is described by PAW method.[11] 29.40 Ry is used as the plane-wave basis set cutoff. The on-site coulomb interaction for Zn is used, namely GGA+U.[12] Conventional GGA or LDA overestimates the coupling between Zn 3*d* and O 2*p* electrons. The ZnO-3*d* electrons also have a higher energy towards the valence

band maximum (VBM) by conventional GGA or LDA. Conventional LDA or GGA treatment of ZnO has an energy gap around 0.8 eV. By DFT+U, this value can be improved, with an energy gap around 2.0 eV. However, this is still smaller than the experimental value of 3.3 eV by 39.4%, but consistent with other DFT+U calculation results.[13] The Zn 3*d* electrons mainly locate around 3~5 eV with respect to the valence band maximum (VBM) by GGA or LDA. After introducing on-site coulomb repulsion energy U, the Zn-3*d* electrons can be better described and the electronic structures are consistent with XPS experiments.[14,13] The Zn 3*d* electrons mainly locate around 7~9 eV below valence band top.

3. 3 Results and Discussion

Six layers of ZnO($10\bar{1}0$) 2×3 are used as the surface slabs for interaction of single molecule with surface, also corresponding to 1/6 monolayer coverage. A 1.6 nm vacuum layers is used to eliminate the longitudinal interactions between super cells. A 5×5×1 Monkhorst-Pack *k*-point mesh is used for the surface slab calculation. A 5×8×1 Monkhorst-Pack *k*-point mesh is used for ZnO($10\bar{1}0$) 2×2 surface slab calculation to simulate half monolayer coverage case. The coverage is defined as the ratio of number of molecules and number of outmost surface Zn atoms. The topmost four layers of the slab and the molecule are allowed to relax until all the residual forces are lower than 20meV/Å. The adsorption energy is calculated by the following equation:

$$\Delta E = -(E - E_0 - E_{adsorbate}) \qquad (1)$$

where E is the energy of ZnO($10\bar{1}0$) substrate with an adsorbate, $E_{adsorbate}$ is the energy of the molecule, and E_0 is the energy of ZnO($10\bar{1}0$) clean substrate without the adsorbate. The detailed adsorption process has been described by Newns-Anderson model.[15,16]

3. 3. 1 Five Typical Configurations with Single Molecule Adsorption

After optimization, five different configurations are considered as shown in Figure 3.3. Covalent adsorption of formic acid and other alkyl acids on ZnO and TiO_2 surface have been theoretically and experimentally investigated.[17-22] The adsorption energies ΔE_1 for 5 configurations are shown in Table 1. Configuration (a) and configuration (e) have the largest and second largest adsorption energies, respectively. Since each molecule in configuration (a) occupies two Zn atoms, the extreme coverage of configuration (a) is half monolayer. The coverage limit of configuration (e) is full monolayer, because each molecule occupies one Zn atoms. Therefore, configuration (e) is the most stable configuration thermodynamically. Fourier transform infrared attenuated total reflectance (FT-IR-ATR) experiments on carboxylic functionalized ZnO nanotips has demonstrated the disappearance of carbonyl bond (C=O) at 1710 cm^{-1} [21], and this is consistent with our calculated most stable configuration.

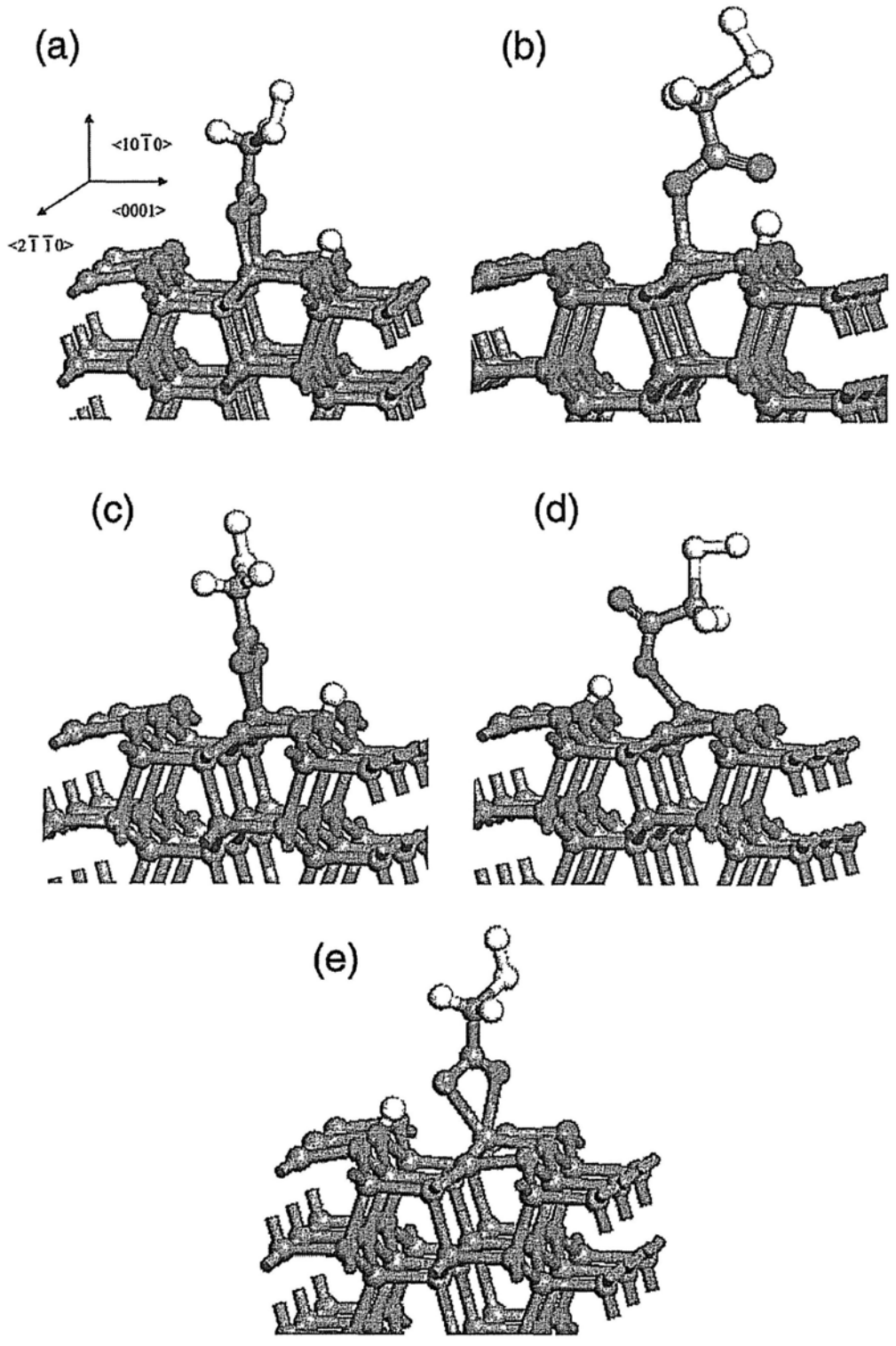

Figure 3. 3 Five adsorption configurations of single molecule case (a) bidentate bridging configuration, (b) monodentate ester-type configuration, (c) bidentate chelating configuration, (d) monodentate O-up configuration, (e) bidentate chelating with hydrogen bonding configuration.

Table 3.1 Adsorption energies $\Delta E_{(1,2,3)}$ and CBM-HOMO energy differences $E^{(1,2,3)}_{\text{CBM-HOMO}}$ for five configurations at 1/6, 1/2, 1 monolayer coverage, respectively.

	a	b	c	d	e
ΔE_1(eV)	1.95	1.59	1.48	0.90	1.73
ΔE_2(eV)	2.06	1.65			1.86
ΔE_3(eV)		1.47			1.66
$E^1_{\text{CBM-HOMO}}$(eV)	1.10	0.82	0.90	0.56	0.86
$E^2_{\text{CBM-HOMO}}$(eV)	0.98	0.60			0.58
$E^3_{\text{CBM-HOMO}}$(eV)		-0.35			-0.22

The electronic coupling between adsorbed molecular orbital and semiconductor surface can be analyzed by projected density of states (PDOS) into organic molecular orbital and semiconductor surface.

The band gap of clean ZnO($10\bar{1}0$) is 1.22 eV, as shown in Figure 3.4(a), and the isolated Mercapto-acetic acid molecule LUMO-HOMO gap is 4.20 eV, as shown in Figure 3.4 (b). Figure 3.4 (c) and (d) show the density of states (DOS) of configuration (b) and configuration (e), respectively. The ZnO surface energy gap is 1.22eV for all configurations. The only difference is the position of HOMO of molecule. For configuration (b), the HOMO lies at 0.40eV higher than VBM of semiconductor, and the energy difference between HOMO and CBM of semiconductor is 0.82eV, which is about 40% smaller than the energy band gap of ZnO surface. For configuration (e), the energy difference between HOMO and CBM of semiconductor is 0.86eV, which is about 30% smaller than the energy band gap of ZnO surface. Molecular orbitals in isolated molecule are strongly localized (Figure3.4 (b)), while adsorbed on ZnO, the molecular orbitals, such as HOMO-1 and below, have strong hybridization with ZnO valence band and tend to be delocalized (Figures 3.4 (c) and (d)). The HOMO of molecule remains its localized characteristics.

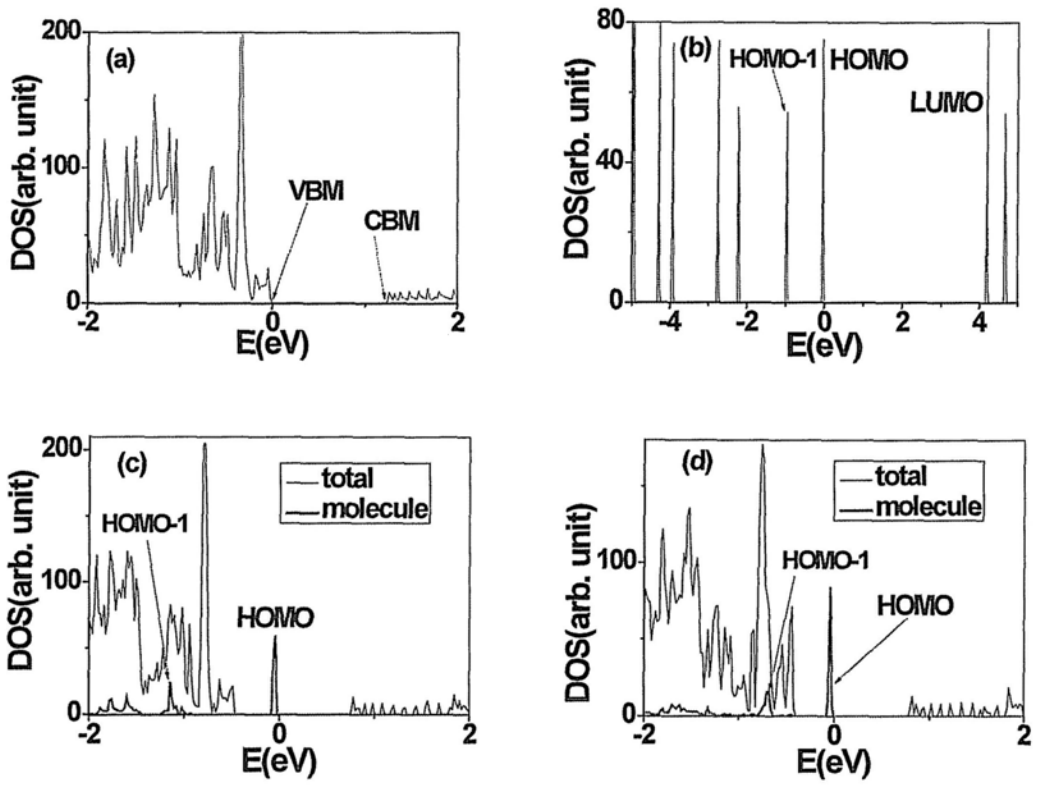

Figure 3. 4 DOS of single molecule case (a) DOS of clean ZnO(10 $\bar{1}$ 0) with 1.22 eV band gap, (b) DOS of isolated mercapto-acetic acid molecule with 4.20 eV LUMO-HOMO gap, (c)monodentate ester-type configuration's DOS, (d) bidentate chelating with Hydrogen bonding configuration's DOS.

The band gap states contributed by the organic molecule effectively facilitate decreasing the energy difference between CBM and VBM, and serve as the transitional states from semiconductor's VBM to CBM. However, this conclusion remains to be further confirmed by experiment. Two channels are possible for molecule excitation from the HOMO to the LUMO of molecule, or from the HOMO directly to the CBM of semiconductor.[23]

The HOMO of dye molecules normally resides in the band gap of semiconductor, while the LUMO lies in the conduction band in order to gain a high efficiency of dye sensitized solar cell. So the interface electronic structure of mercapto-acetic acid-ZnO fulfills these two criteria. The efficiency of dye sensitized solar cells is mainly evaluated by two factors: (1) the maximum photocurrent density, I_{ph}, corresponding to the charge injection from the HOMO of molecule into the

semiconductor conduction band. (2) the open circuit potential, V_{oc}, related to the energy difference between the HOMO and the CBM of semicondcutor.[24]

The energy difference $E^1_{\text{CBM-HOMO}}$ between CBM and HOMO is shown in Table 1 and it strongly depends on adsorption configurations from 0.56 to 1.10 eV. Ref. 25 has also reported the adsorption configuration dependent electronic structure of catechol on rutile TiO_2(110). Electronic structure shows bonding geometry dependence and only bidendate configuration introduces band gap states into the semiconductor. -COOH anchored dye on anatase TiO_2 has been studied and different adsorption modes lead to different open-circuit voltage of dye-sensitized solar cells.[26]

According to our calculations, each configuration can totally transfer around 0.3 electrons to the ZnO surface. The oxygen atom of –COOH gains electrons from surface by Zn-O bonding, while H atom of –COOH serves as the donor to the surface by O-H bonding. The net effect between the two charge transfer pathways is that the oxide surface gains 0.3 electrons from the molecule. Generally speaking, the gained electrons from the molecule may enhance the ZnO n-type intrinsic conductivity.

The charge transfer effects are almost the same for all configurations, but electronic structures depend on specific configurations, which is also an intriguing attribute of this molecule-oxide interface.

Hydrogen adsorption on ZnO($10\bar{1}0$) surface has led to metal to insulator transition, confirmed by STS measurement.[27] Another wide bandgap SiC also shows surface metallicity after β-SiC(100) passivated by hydrogen under UHV-STM study.[28]

3. 3. 2 Coverage Dependence: Half Monolayer and Full Monolayer

For coverage dependence, bidentate bridging configuration, monodentate ester-type adsorption and bidentate chelating with hydrogen bonding modes are mainly discussed. However, bidentate bridging configuration is lack of full monolayer coverage, since each molecule occupies two surface Zn atoms.

For 1/2 coverage, adsorption energy ΔE_2 and the CBM-HOMO energy difference

$E^2_{\text{CBM-HOMO}}$ are shown in Table1. The adsorption energies of three configurations are all higher than single molecule cases due to intermolecular interactions. Actually for configuration (b) and configuration (e), there are two growth directions for molecular assembly along <2 $\bar{1}$ $\bar{1}$ 0> or <0001>. For configuration (b), the adsorption energy for growth along <0001> is 0.38 eV higher than <2 $\bar{1}$ $\bar{1}$ 0>; for configuration (e), the corresponding value is 0.46 eV. So the molecules tend to assemble along <0001> at initial growth stage, and this preferred growth direction is the same with ZnO nanostructure growth direction.

Figure 3.5 (a) shows the DOS of bidentate bridging configuration, and the open circuit potential is 0.98 eV, which is about 0.12 eV less than that of 1/6 monolayer coverage. Figure 3.5 (b) shows the DOS of monodentate ester-type configuration, and the open circuit potential is 0.60 eV, which is about 0.15 eV less than that of 1/6 monolayer coverage. Figure 3.5 (c) shows the DOS of bidentate chelating with hydrogen bonding configuration, and the open circuit potential is 0.58 eV, which is about 0.28 eV less than that of 1/6 monolayer coverage. The band gap states of mercapto-acetic acid with half monolayer coverage have a width around 2~3 times that of 1/6 monolayer case. The occupied molecular orbitals (below VBM) have strong hybridization with ZnO valence band and tend to be more delocalized.

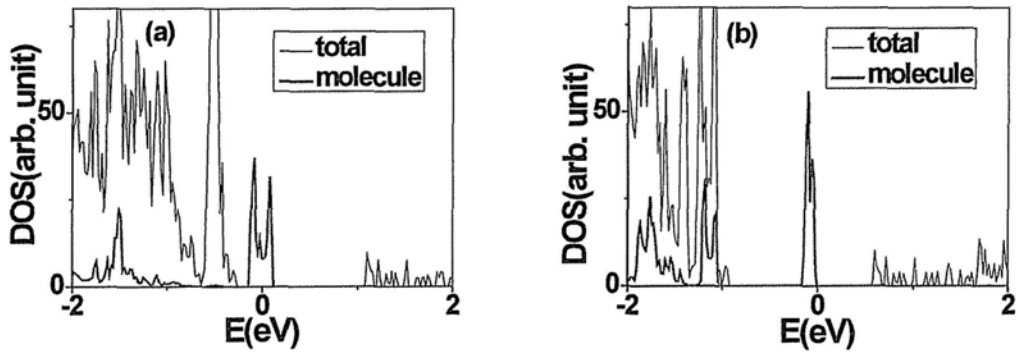

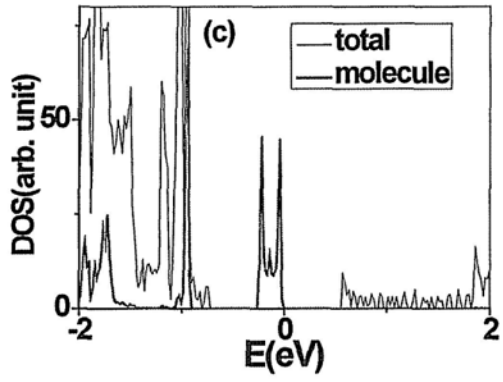

Figure 3.5 DOS of half monolayer coverage (a) DOS of bidentate bridging configuration, (b) DOS of monodentate ester-type configuration, (c) DOS of bidentate chelating with Hydrogen bonding configuration.

For full monolayer coverage, monodentate ester-type and bidentate chelating with hydrogen bonding adsorption modes are involved. The structures after optimization are shown in Figures 3.6 (a) and (b). Adsorption energy ΔE_3 and CBM-HOMO energy difference $E^3_{\text{CBM-HOMO}}$ are shown in Table1. The adsorption energies are 1.47 eV and 1.66 eV per molecule for monodentate ester-type and bidentate chelating with hydrogen bonding, respectively. The coupling between organic monolayer and semiconductor can be manifested by band structure. Figure 3.7 (a) shows the band structure of monodentate ester-type configuration. The Fermi level lies around 0.35 eV higher than the CBM. The 4*s* orbital of Zn has been partially filled, so the semiconductor has been on the edge of metal to insulator transition. The energy gap between VBM and CBM has been filled by molecule states. The molecule monolayer contributes the continued states from 0.21 eV below the VBM to the HOMO (0.35 eV higher than CBM). The semiconductor remains its merit of direct band gap characteristic, and the energy gap is 1.22 eV. The HOMO of molecule lies at the edge of CBM. Figure 3.7(b) shows the band structure of monolayer coverage case for bidentate chelating with hydrogen bonding. The Fermi level lies around 0.22 eV higher than the CBM, so for bidentate chelating with hydrogen bonding monolayer coverage, the organic molecule-semiconductor system is also on the edge of metal to insulator transition. The molecular monolayer contributes an abundance of

continuously occupied states with a width of 1.69 eV, which fully fills the band gap of ZnO. The conductive and photovoltaic performance will be pronouncedly enhanced. The merit of direct band gap characteristic of ZnO has also remained unchanged. These results are consistent with Ref. 7, which has reported experimentally that the conductance of ZnO is enhanced by 6 orders of magnitude upon mercapto-acetic acid molecule functionalization.

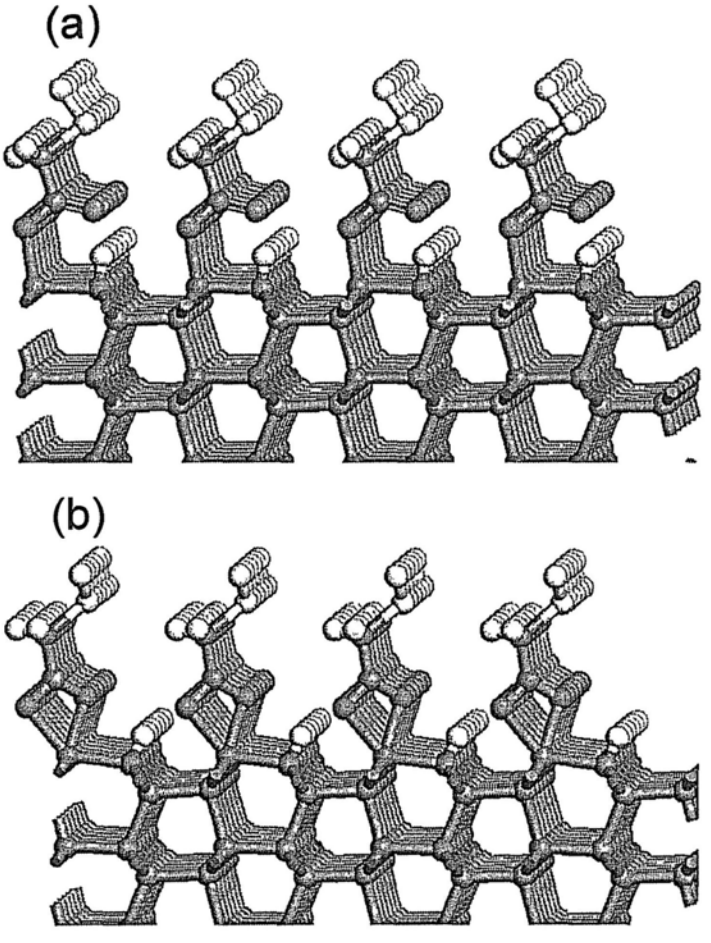

Figure 3.6 Structures of full monolayer coverage (a) monodentate ester-type configuration, (b) bidentate chelating with Hydrogen bonding configuration.

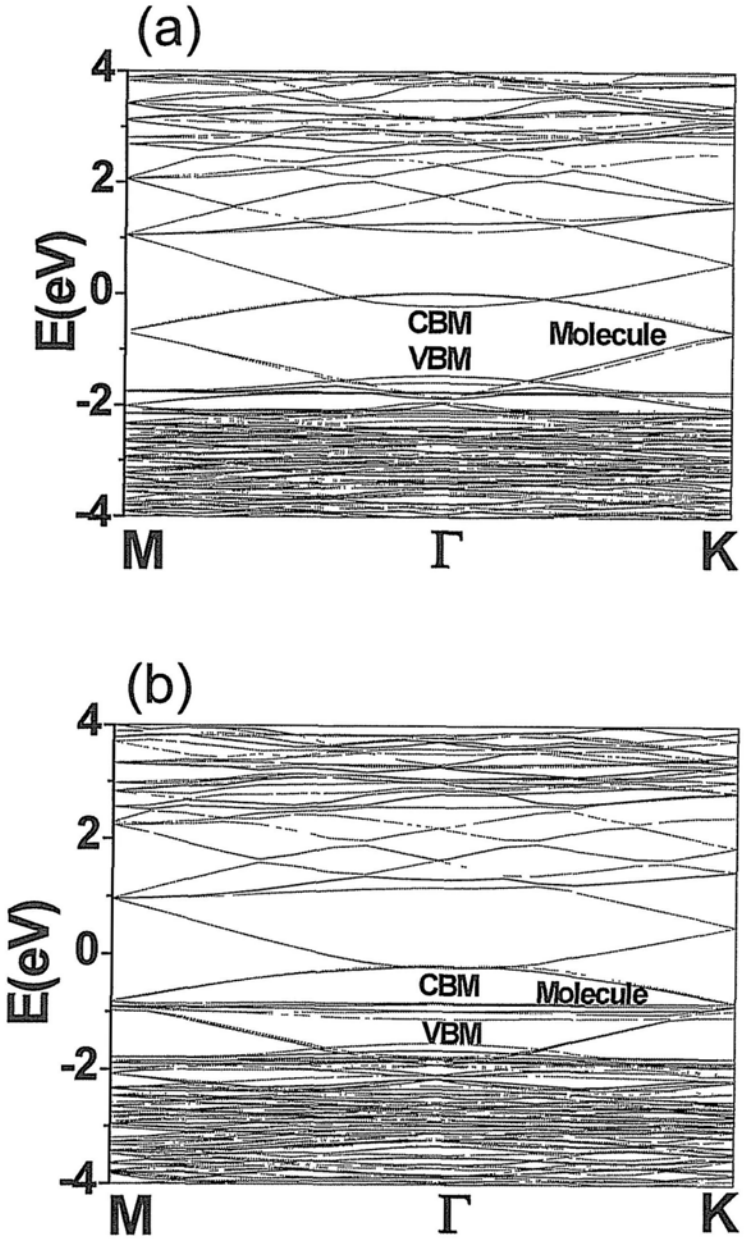

Figure 3.7 Band structures of full monolayer coverage (a) monodentate ester-type configuration, (b) bidentate chelating with Hydrogen bonding configuration.

3. 3. 3 Facet Dependence: Monolayer Functionalized ZnO($2\bar{1}\bar{1}0$) Surface

The interaction between mercapto-acetic acid molecule and another non-polar majority ZnO($2\bar{1}\bar{1}0$) surface is also investigated. Both monodentate ester-type configuration and bidentate chelating with hydrogen bonding configuration are involved on this surface. Figure 3.8 shows the optimized structure of molecular monolayer on ZnO($2\bar{1}\bar{1}0$). The intermolecular interaction has strong influence on the assembly morphology of molecule. ZnO($2\bar{1}\bar{1}0$) surface 1×1 is used as the substrate. Full monolayer coverage corresponds to 2 molecules per super cell. The molecular monolayer assembly structure is highly different from ZnO($10\bar{1}0$) case. The clean ZnO($2\bar{1}\bar{1}0$) band gap is 1.22 eV, as shown in Figure 3.9 (a). The figure shows the DOS of monodentate ester-type configuration. Molecules contribute to the band gap states, but no metal to insulator transition is found. The energy difference between the CBM and the HOMO is around 0.31 eV. The molecule contributed band gap states split into two peaks, HOMO and HOMO-1, corresponding to two molecule interaction. For bidentate chelating with hydrogen bonding configuration, with DOS shown in Figure 3.9 (c), the energy difference between the CBM and the HOMO is around 0.93 eV. The molecular monolayer contributes an abundance of band gap states into ZnO, but the band gap of ZnO has not been fully filled. The occupied molecular orbitals (below VBM) have strong hybridization with ZnO valence band and tend to be more delocalized. So mercapto-acetic acid molecule functionalized ZnO also shows face dependence and strong configuration dependent electronic structure.

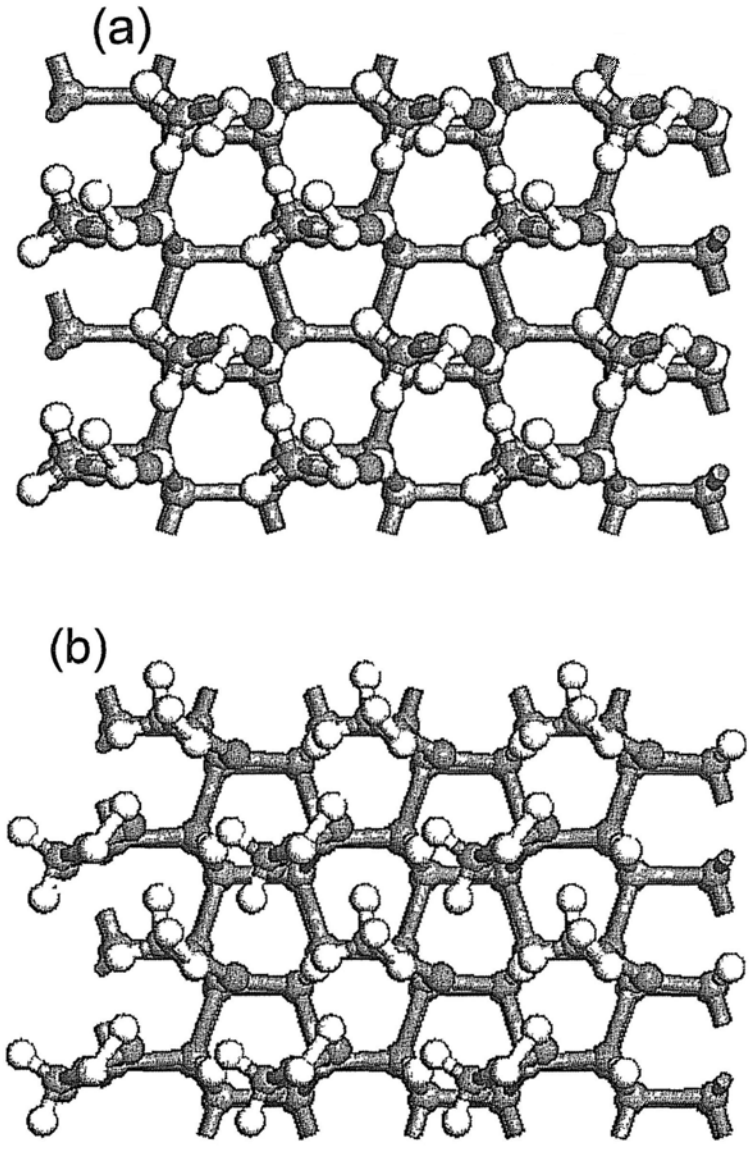

Figure 3.8 Structures of full monolayer coverage on ZnO($2\bar{1}\,\bar{1}\,0$) (a) top view of monodentate ester-type configuration, (b) top view of bidentate chelating with Hydrogen bonding configuration.

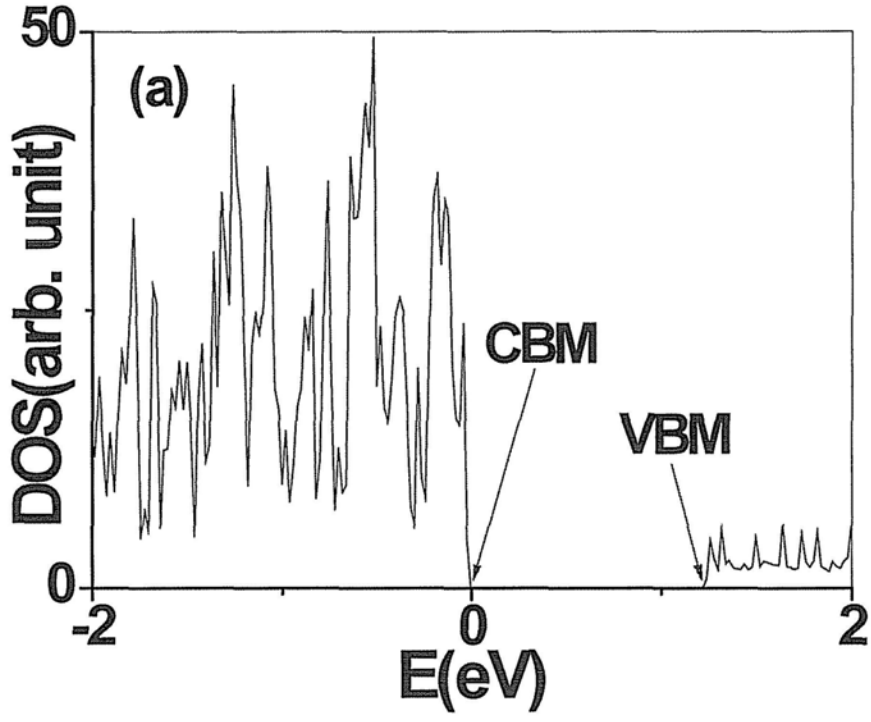
50
(a)
DOS(arb. unit)
CBM
VBM
0
-2
0
2
E(eV)

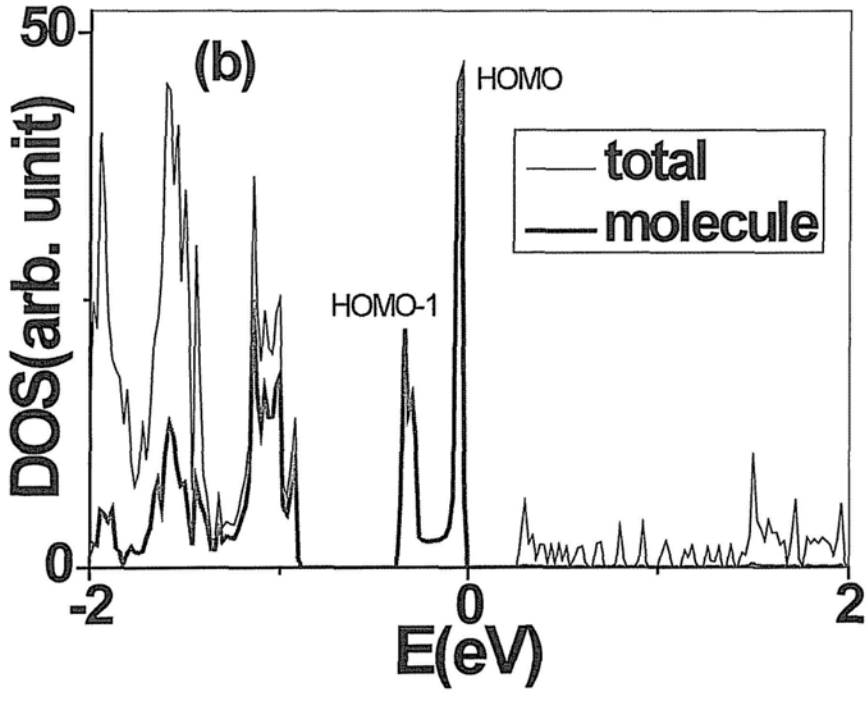
50
(b)
HOMO
total
molecule
HOMO-1
DOS(arb. unit)
0
-2
0
2
E(eV)

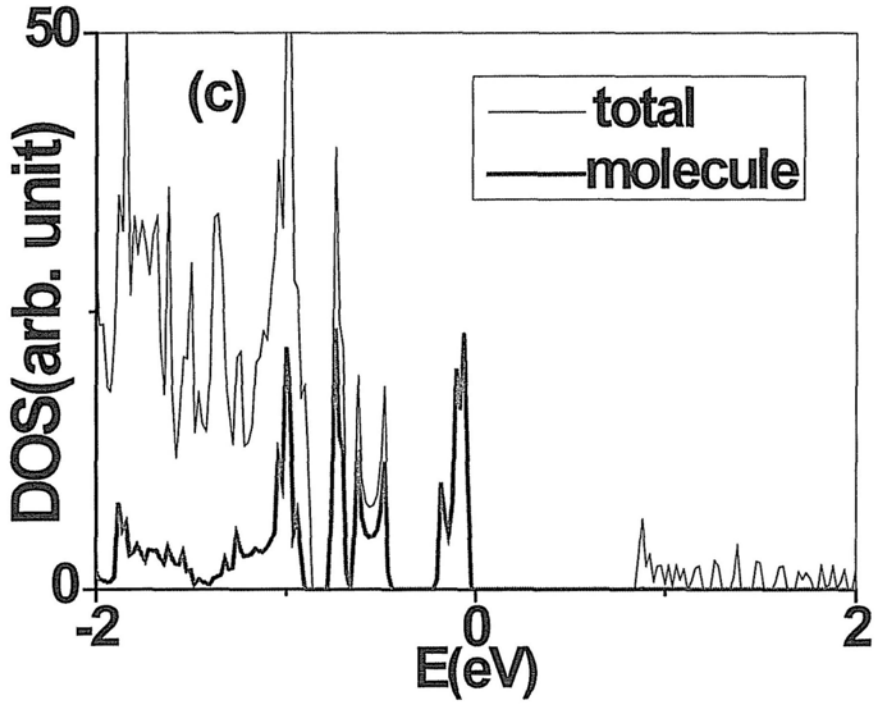

Figure 3.9 DOS of full monolayer functionalized ZnO($2\bar{1}\,\bar{1}\,0$) (a) DOS of clean ZnO($2\bar{1}\,\bar{1}\,0$) with 1.22 eV band gap, (b) DOS of monodentate ester-type configuration, (c) DOS of bidentate. chelating with hydrogen bonding configuration.

3.3.4 Tail Dependence

The influence of molecular tails on the electronic structure of molecule-semiconductor interface is investigated. The interface between acetic acid, benzoic acid, 9-Anthracenecarboxylic acid on ($10\,\bar{1}\,0$) with configuration (e) are calculated and the structure optimization results are shown in Figure 3.10. The DOS is shown in Figure 3.11.

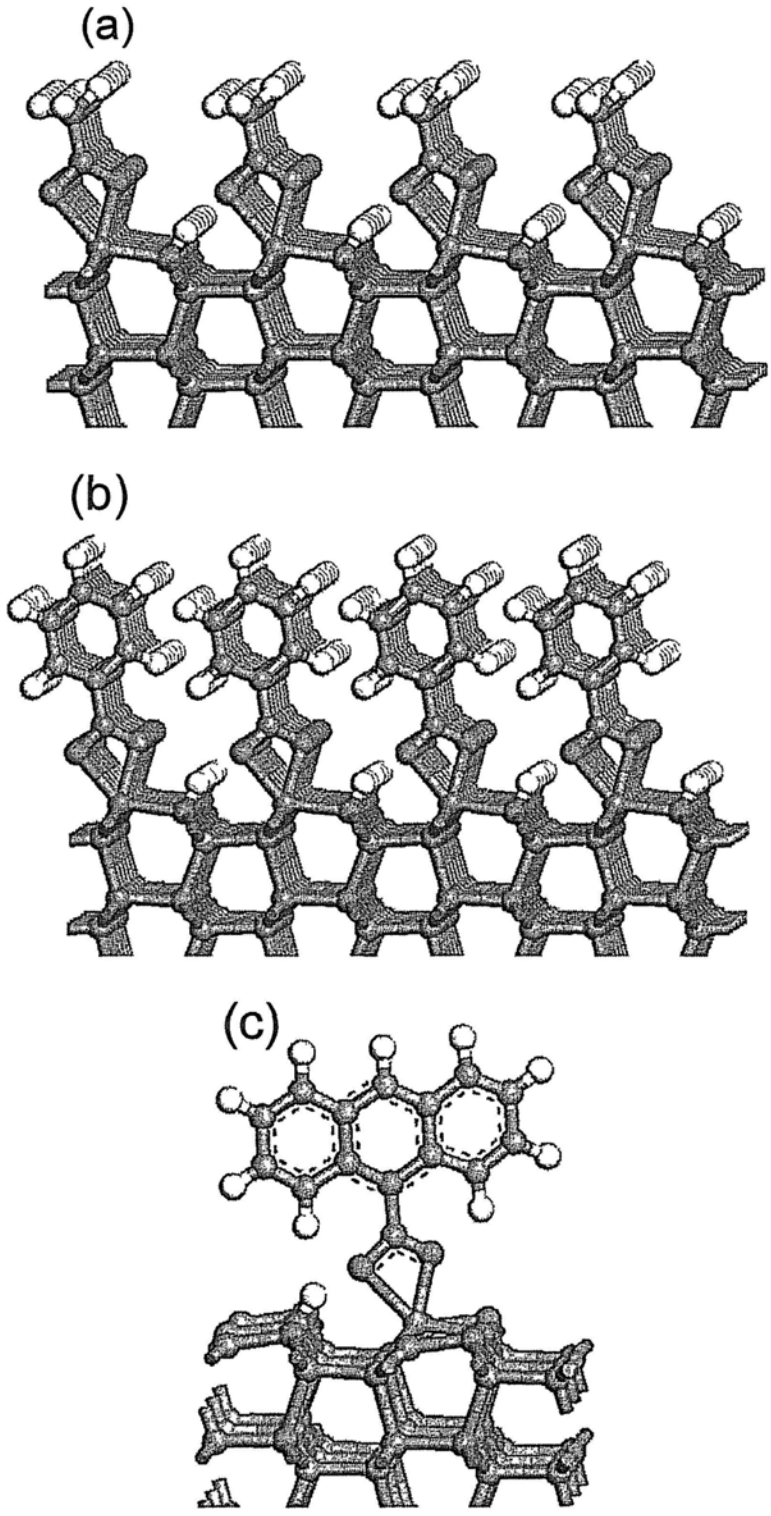

Figure 3.10 Structure of acetic acid full monolayer, benzoic acid full monolayer and 9-anthracenecarboxylic acid on surface.

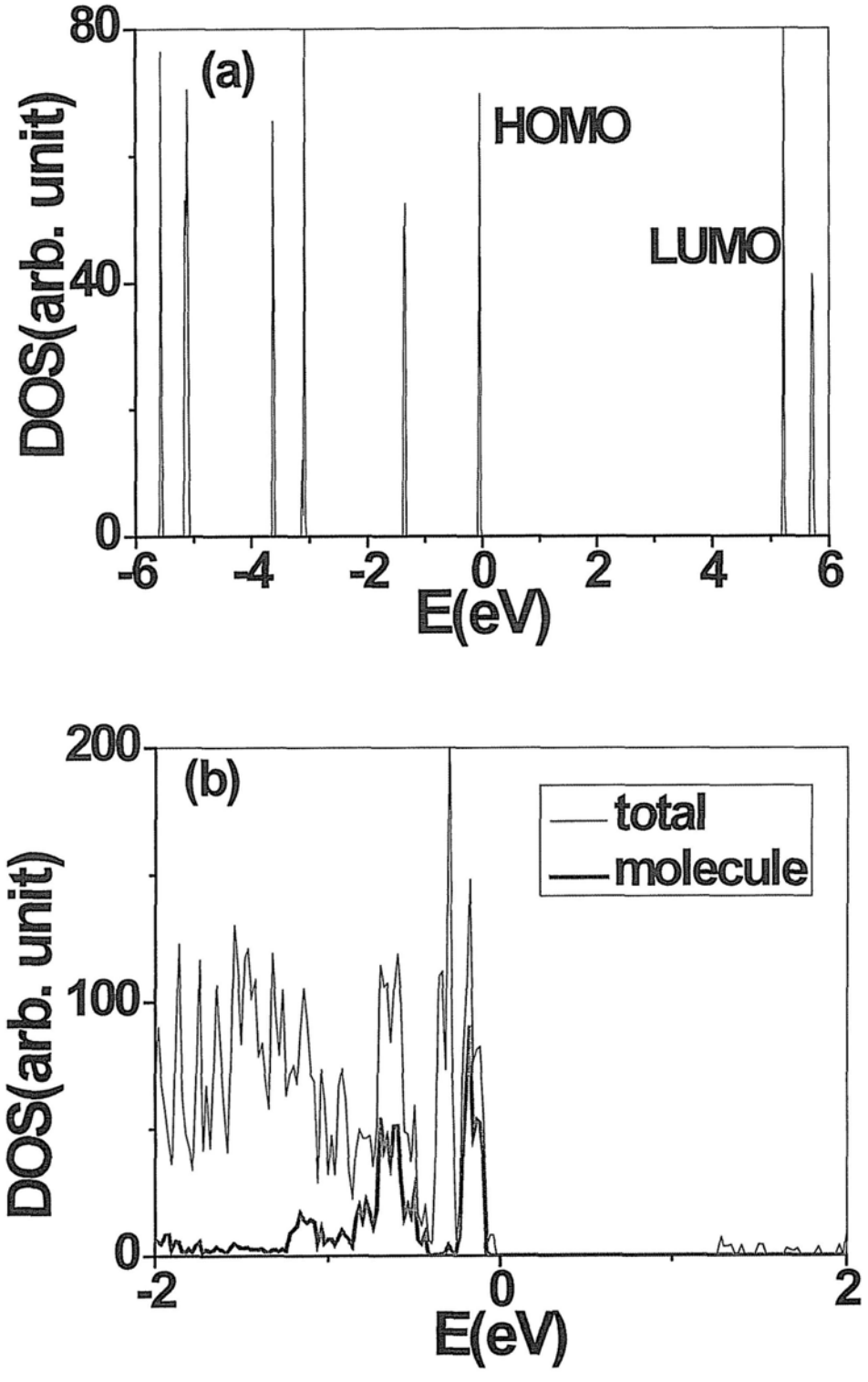
(a)
HOMO
LUMO
DOS(arb. unit)
E(eV)
80
40
0
-6
-4
-2
0
2
4
6
(b)
total
molecule
DOS(arb. unit)
E(eV)
200
100
0
-2
0
2

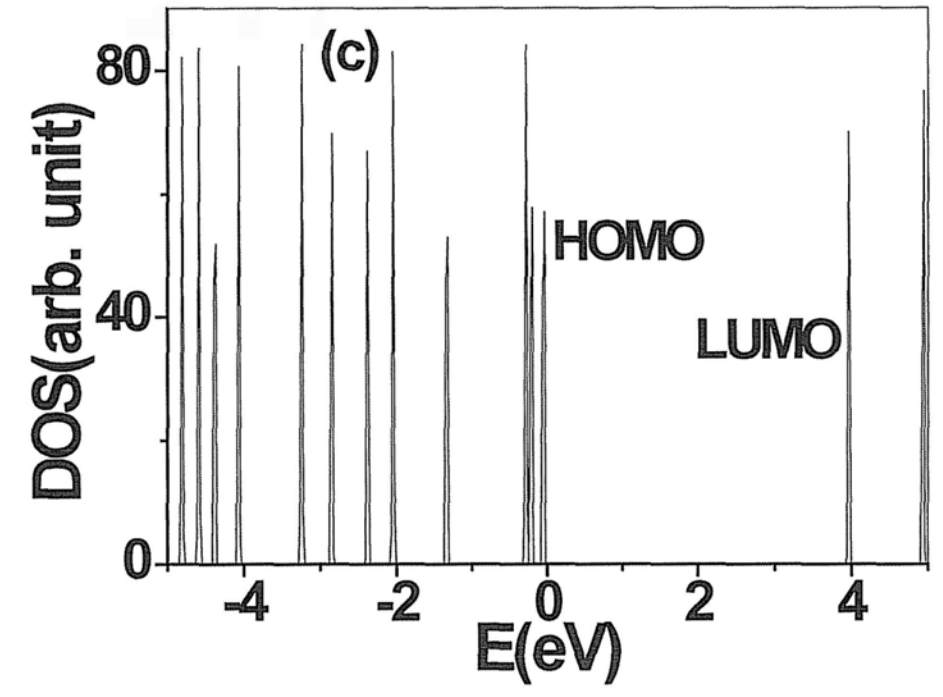
(c)
80
40
0
DOS(arb. unit)
HOMO
LUMO
-4
-2
0
2
4
E(eV)

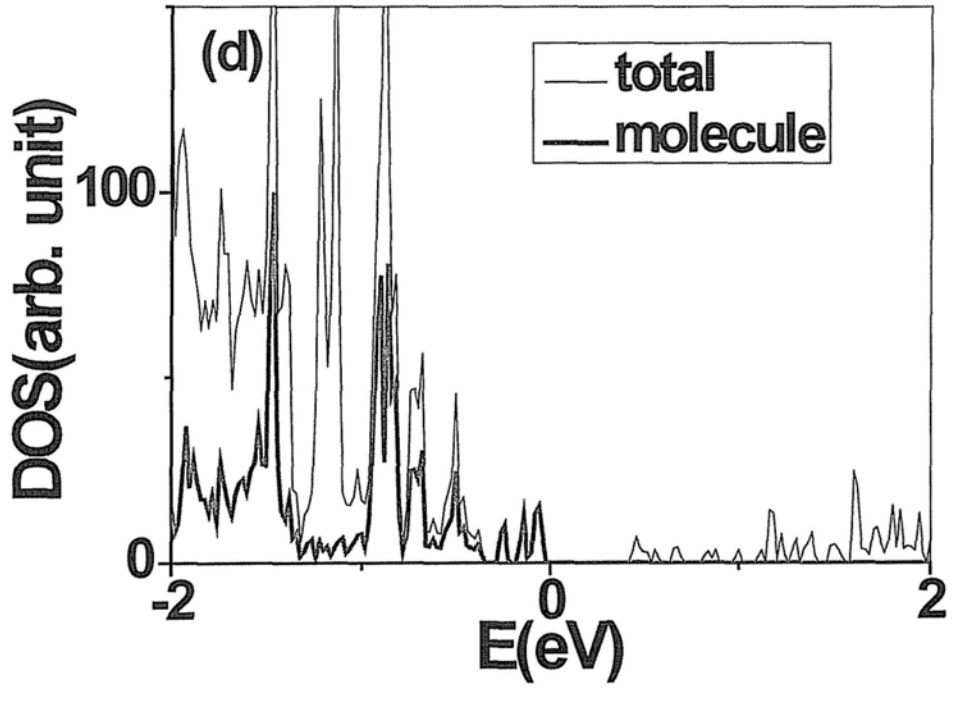
(d)
total
molecule
100
0
DOS(arb. unit)
-2
0
2
E(eV)

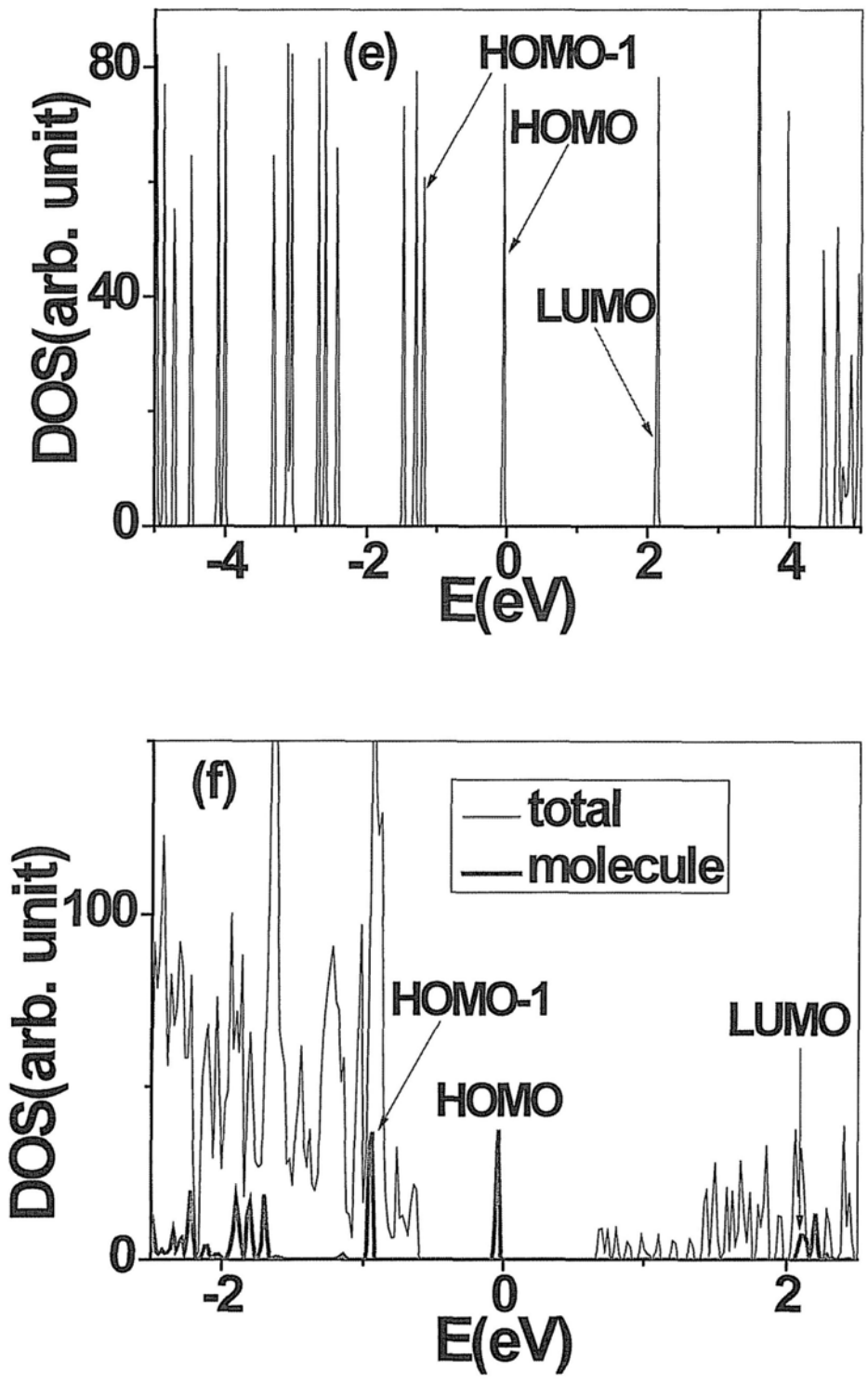

Figure 3.11 DOS of acetic acid full monolayer, benzoic acid and 9-anthracenecarboxylic acid on surface (a) DOS of isolated acetic acid molecule with 5.22 eV LUMO-HOMO gap, (b) DOS of acetic acid monolayer functionalized surface, (c) DOS of isolated benzoic acid molecule with 3.96 eV LUMO-HOMO gap, (d) Dos of benzoic acid monolayer functionalized surface, (e) DOS of isolated 9-anthracenecarboxylic acid molecule with 2.14 eV LUMO-HOMO gap, (f) DOS of 9-anthracenecarboxylic acid functionalized surface.

Figure 3.11(a) shows the DOS of isolated acetic acid molecule and its LUMO-HOMO difference is 5.22 eV. Acetic acid does not contribute to the band gap states of ZnO, as shown in Figure 3.11(b), and is consistent with the self-consistent charge density functional tight binding (SCC-DFTB) calculation of carboxylic acid on ZnO($10\bar{1}0$) in Ref. 18. The LUMO-HOMO difference for benzoic acid is 3.96 eV, as shown in Figure3.11(c). Benzoic acid contributes an abundance of band gap states, with a width around 0.36eV as shown in Figure 3.11(d). The energy difference between the HOMO and the CBM is 0.86 eV. So it is expected this interface could have a good conductive and photovoltaic performance. The occupied molecular orbitals (below VBM) have strong hybridization with ZnO valence band and tend to be more delocalized. 9-anthracenecarboxylic acid is also used as the tail of the –COOH anchor group, which has been studied experimentally on TiO_2 surface.[29,30] The LUMO-HOMO gap of 9-anthracenecarboxylic acid is 2.14 eV, as shown in Figure 3.11 (e). The open circuit potential is 0.70 eV for 9-anthracenecarboxylic acid from its DOS distribution in Figure 3.11(f), in contrast to the same situation for mercapto-acetic acid with 0.90eV in configuration (e). The occupied molecular orbital HOMO-1 and below have strong hybridization with ZnO valence band, since there exist peaks at the same energy levels with ZnO.

3.4 Conclusion

Mercapto-acetic acid molecule is investigated as the major molecule for carboxylic acid molecules adsorption on ZnO($10\bar{1}0$). For 1/6 monolayer coverage, the electronic structure of mercapto-acetic acid molecule-ZnO interface shows a strong configuration dependence. Mercapto-acetic acid monolayer functionalized ZnO($10\bar{1}0$) is on the verge of metal to insulator transition, which is consistent with the experimental findings. Mercapto-acetic acid monolayer functionalized ZnO($2\bar{1}\bar{1}0$) surface does not show metal to insulator transition. Acetic acid does not contribute to the band gap states of ZnO($10\bar{1}0$) surface. However, benzoic acid and

9-anthracenecarboxylic acid can contribute an abundance of band gap states into the ZnO($10\bar{1}0$) surface, whereas 9-anthracenecarboxylic acid functionalized ZnO($10\bar{1}0$) surface shows a smaller CBM-HOMO energy difference compared to mercapto-acetic acid in the same situation. These results shed light on understanding of the charge carrier characteristics on organic molecule treated ZnO surfaces, and pave the way for future applications of organic molecule treated ZnO surfaces, in solar cells and biosensors, as well as oxide surface engineering and molecular electronics.

References

(1) Kanai, Y.; Selloni, A. *J. Am. Chem. Soc.* **2006**, 128, 3892-3893.

(2) Deutsch, D.; Natan, A.; Shapira, Y.; Kronik, L. *J. Am. Chem. Soc.* **2007**, 129, 2989- 2997.

(3) (a) Lucas, M; Mai, W. J.; Yang, R.S.; Wang, Z. L.; Riedo, E. *Nano Lett* **2007**, 7, 1314-1317. (b) Wang, X.D.; Zhou, J.; Song, J.H.; Liu, J.; Xu, N.S.; Wang, Z.L. *Nano Lett* **2006,** 6, 2768-2772.

(4) (a) Marana, N. L.; Longo, V. M.; Longo, E.; Martins, J. B. L.; Sambrano, J. R. *J. Phys. Chem. A* **2008**, 112, 8958-8963. (b) Diebolda, U.; Koplitzb, L. V.; Dulub, O. *Appl. Surf. Sci.* **2004**, 237, 336-342. (c) Meyer, B.; Marx, D.; Phys. Rev. B **2003**, 67, 035403-035413. (d) Kresse, G.; private communication with Diebolda. (e) Wander, A.; Schedin, F.; Steadman, P.; Norris, A.; McGrath, R.; Turner, T. S.; Thornton, G.; Harrison, N.M. *Phys. Rev. Lett.* **2001**, 86, 3811-3814. (f) Wander, A.; Harrison, N.M. *Surf. Sci.* **2000**, 457, L342- L346.

(5) Matsui, H.; Hasuike, N.; Harima, H.; Tabata1, H. *J. Appl. Phys.* **2008**, 104, 094309.

(6) Quintanaa, M.; Marinadob, T.; Nonomurab, K.; Boschloob, G.; Hagfeldt, A. *J. Photochem. Photobiol. A* **2009**, 202, 159-163.

(7) Lao, C. S.; Li, Y.; Wong, C. P.; Wang, Z. L. *Nano Lett.* **2007**, 7, 1323- 1328.

(8) Kresse, G.; Furthmu¨ller, J. *Comput. Mater. Sci.* **1996**, 6, 15-50.

(9) Perdew, J. P.; Chevary, J. A.; Vosko, S. H.; Jackson, K. A.; Pederson, M. R.; Singh, D. J.; Fiolhais, C. *Phys. Rev. B* **1992**, 46, 6671-6687.

(10) Perdew, J. P.; Wang, Y. *Phys. Rev. B* **1992**, 45, 13244-13249.

(11) Kresse, G.; Joubert, D. *Phys. Rev. B* **1999**, 59, 1758-1775.

(12) Dudarev, S.L.; Botton, G.A.; Savrasov, S.Y.; Humphreys, C.J.; Sutton, A.P. *Phys. Rev. B* **1998**, **57**, 1505.

(13) (a) Janotti, A.; Walle, C. G. V. D. *Phys. Rev. B* **2007**, **75**, 121201-121204. (b) Lany, S.; Zunger, A. *Phys. Rev. B* **2008**, 78, 235104-235128. (c) Kim, Y.S.; Park, C. H. *Phys. Rev. Lett.* **2009**, 102, 086403-086406. (d) Janotti, A.; Segev, D.; Walle, C. G. V.

D. *Phys. Rev. B* **2006**, 74, 045202-045210.

(14) Wang, J.; Li, Q.; Egerton, R.F. *Micron* **2007**, 38, 346-353

(15) Anderson, P. W. *Phys. Rev.* **1961**, 124, 41-53.

(16) Newnst, M. *Phy. Rev.* **1969**, 178, 1123-1145.

(17) Gong, X.Q.; Selloni, A.; Vittadini, A. *J. Phys. Chem. B* **2006**, 110, 2804-2811.

(18) Moreira, N. H.; Rosa, A. L. D.; Frauenheim, T. *Appl. Phy. Lett.* **2009**, 94, 193109-193111.

(19) Persson, P.; Lunell, S.; Ojamäe, L. *Int. J. Quantum Chem.* **2002**, 89, 172-180.

(20) Persson, P.; Ojam¨ae, L. *Chem. Phys. Lett.* **2000**, 321, 302-308.

(21) Taratula, O.; Galoppini, E.; Wang, D.; Chu, D.; Zhang, Z.; Chen, H.; Saraf, G.; Lu, Y. *J. Phys. Chem. B* **2006**, 110, 6506-6515.

(22) Tanner, R. E.; Sasahara, A.; Liang, Y.; Altman, E. I.; Onishi, H. *J. Phys. Chem. B* **2002**, 106, 8211-8222.

(23) Persson, P.; Bergstrm, R.; Lunell, S. *J. Phys. Chem. B* **2000**, 104, 10348-10351.

(24) Meng, S.; Ren, J.; Kaxiras, E. *Nano Lett.*, **2008**, 8, 3266-3276.

(25) Li, S. C.; Wang, J. G.; Jacobson, P.; Gong, X. Q.; Selloni, A.; Diebold, U. *J. Am. Chem. Soc.* **2009**, 131, 980-984.

(26) Angelis, F. D.; Fantacci, S.; Selloni, A.; Gra1tzel, M.; Nazeeruddin, M. K. *Nano. Lett.* **2007**, **7**, 3189-3195.

(27) Wang, Y.; Meyer, B.; Yin, X.; Kunat, M.; Langenberg, D.; Traeger, F.; Birkner, A.; Wo¨ll, Ch. *Phys. Rev. Lett.* **2005**, 95, 266104-266107.

(28) Deryckei, V.; Soukiassian, P. G.; Amy, F.; Chabal, Y. J.; Angeol, M. D. D.; Enriquezi, H. B.; Silly, M. G. *Nat. Mater.* **2003**, 2, 253-258.

(29) Kamat, P. V. *J. Phys. Chem.* **1989**, 93, 859-864.

(30) He, J. J.; Zhao, J. C.; Shen, T; Hidaka, H.; Serpone, N. *J. Phys. Chem. B* **1997**, 101, 9027-9034.

Chapter 4 Band Gap Opening of Bilayer Graphene by F4-TCNQ Molecular Doping and Externally Applied Electric Field

4. 1 Introduction

Graphene sheet has attracted abundance of research interest, since it was first experimentally discovered by K. S. Novoselov *et al.* in 2004.[1] Graphene-based nanoelectronics have been considered as a potential substitute of the conventional semiconductor-based microelectronics, due to its excellent properties including the extremely high mobility up to 20000 cm^2/V-s close to the Dirac point and the ballistic charge transport.[1-8] However, the zero-gap characteristic has limited its applications in the areas of electrical, optical and magnetic. Therefore, how to manipulate the electronic structure of graphene is of fundamental importance. Actually, it has been reported that a band gap can be opened asymmetrically in bilayer graphene, which could be generated by coulomb potential difference between the two graphene layers exerted by a perpendicular electric field (E_{ext}).[9-14] While the present bottleneck of using E_{ext} to create the band gap in bilayer graphene is that the band gap is extremely small with no more than 180 meV, as a results of E_{ext} strength weakened to the limit of 0.1 V/Å by the SiO_2 dielectric.[9]

In addition to the variable of E_{ext}, charge transfer doping is another variable of affecting the band-gap opening in bilayer graphene. Two effective doping approaches have been commonly applied to control the band gap opening of graphene. One method is the metal atomic doping. The *n*-type doping effects semiconductor has been successfully achieved, by doping potassium on ultrathin epitaxial graphene (EG). Furthermore, the gap between its valence and conduction bands could be tuned by

controlling the concentration of potassium.[15] The *p*-type doping effect has also been demonstrated by depositing gold atoms onto graphene[16], where the Dirac point was shifted into the unoccupied states. Unfortunately, one disadvantage induced by this method is structural conformation, defects and clustering of dopants. Another approach of controlling the band gap opening is hydrogenation of graphene, while the deficiency of strong structural conformation was still introduced.[17-19]

How to avoid these problems caused by metal atom doping and hydrogenation of graphene? Organic molecular surface functionalization is found to be an effective method. For example, as recently studied by the first principles theoretical calculations and experiments, it has been found that tetracyanoethylene (TCNE) and tetracyanoquinodimethane (TCNQ) functionalization on graphene could achieve the band gap opening and charge transfer induced *p*-type doping effect.[20-22] $NH_3(CH)_6CO_2$ and $NH_3(CH)_{10}CO_2$ modification on graphene could induce a band gap into graphene nanoribbon.[23] More previously, tetrafluoro-tetracyanoquinodimethane (F4-TCNQ) was proved to be an excellent candidate of functionalizing graphene to achieve the *p*-type doping effect, as studied by Wee *et al* in performing angle-resolved photoemission spectroscopy (ARPES) experiment.[24] One notable advantage of employing F4-TCNQ as a strong molecular acceptor to modify the graphene surface is that no defect or strong structural conformation was created, and hence the graphene could remain its perfect two dimensional honeycomb structure. The other advantage is that no clustering of molecular dopants appears due to the charged F4-TCNQ anions repulsion between each other at a high coverage. Accordingly, effective and controllable doping that maintains the extraordinarily high mobility of graphene would be accomplished by F4-TCNQ as a dopant. F4-TCNQ doped carbon nanotube field-effect transistor has been fabricated experimentally, and it was found that the device performances such as transconductance, on-resistance, and on/off ratio were improved by the F4-TCNQ doping effects.[25] F4-TCNQ P type doping of single layer graphene has also been investigated by first principles method.[26]

Since efforts have been previously reported to manipulate the electronic structure of bilayer graphene by E_{ext} and charge transfer related doping separately.[9-16,

[20] In the present report, by applying first principles method, we will for the first time theoretically investigate the modulation of bilayer graphene electronic structure by combining the F4-TCNQ molecular doping and E_{ext}. To give a contrast, the F4-TCNQ functionalizations on bilayer graphene at low and high coverage are taken into account respectively. The properties of the band gap opening and charge transfer are compared between the F4-TCNQ doping at different coverage and a pristine bilayer graphene.

4. 2 Computational Method

The calculations are performed within *Vienna ab initio simulation package* (VASP)[27] based on Density Functional Theory (DFT). The electron-ion interaction is described by PAW potentials[28] and plane-wave basis set, with the local density approximation (LDA) exchange-correlation functional and a cutoff energy of 29.40 Ry. Graphene bilayer modeled by $4\sqrt{3}\times7$ supercell is used as a substrate to simulate an isolated F4-TCNQ molecule adsorption, and also to represent a low coverage of 5.7×10^{-11} mol/cm^2. The supercell containing 244 atoms, which is large enough to ensure the lateral distance between the molecules is larger than 10 Å. The vacuum layer of 1.8 nm is used to eliminate the longitudinal interactions between the super cells. To simulate a high coverage of 1.3×10^{-10} mol/cm^2, a $3\sqrt{3}\times4$ bilayer graphene plus one F4-TCNQ molecule is applied. The sampling for the Brillouin zone includes $4\times4\times1$ and $6\times6\times1$ Monkhorst-Pack *k*-point for the low and high coverage respectively.

Our LDA calculations of band-gap opening of the pristine bilayer graphene under E_{ext} are in reasonable agreement with the experimental observations of a tunable band gap in the bilayer graphene.[9] LDA overestimates the adsorption energy, while GGA underestimates the adsorption energy. LDA is better than GGA in describing weakly bound system[29,30], but neither does GGA or LDA take into account the van der Waals interactions. In order to figure out the most stable adsorption site

and orientation, molecular mechanics (MM) calculations are carried out here, due to its success in treating π-conjugated molecules adsorption on surface.[31,32] MM+ force field, improved from MM2, is used in MM calculations. Ten high symmetry F4-TCNQ adsorption configurations are considered, according to the orientations of the benzene ring and cyano group with respect to the hexagonal rings of graphene. Configurations with the molecular planes parallel (lying-down) and perpendicular (standing-up) to the graphene surface are both taken into account, as shown in Figure1. The adsorption energy is calculated by the following equation:

$$\Delta E = -(E - E_0 - E_{adsorbate}) \qquad (1)$$

where E is the total energy of graphene with the molecular adsorbate; $E_{adsorbate}$ is the total energy of the molecular adsorbate; E_0 is the total energy of pristine graphene.

4.3 Results and Discussion

4.3.1 Adsorption Configurations of F4-TCNQ on Bilayer Graphene at Low Coverage.

Figure 4.1 shows ten adsorption configurations for F4-TCNQ molecules on bilayer graphene at the low coverage. Comparing the corresponding calculated adsorption energies listed in Table 1, it is found that the adsorption energies of four standing-up configurations are around 0.62 eV lower than the lying-down ones. Consequently, the molecule prefers to adopt the lying-down configuration on the graphene in which more functional atoms of the molecule interact with the carbon atoms of graphene by partial sp^3 hybridization. Among the six lying-down configurations, the most stable adsorption is rendered by configuration (e) with the largest adsorption energy of 1.95 eV. The transition from the lying-down to the standing-up configurations is very difficult, due to the very large energy barrier. For a comparison, the adsorption energies of four standing-up configurations are around 0.75 eV lower than these of lying-down ones from MM calculations. Again, the most

stable one among the lying-down configurations is found to be configuration (e) with the adsorption energy of 1.46 eV, which is around 0.06~0.19 eV larger than that of other lying-down sites. For configuration (e), the nitrogen atom of cyano group is on the top of the underlying carbon atom. Such arrangement is similar to the most stable adsorption configuration of F4-TCNQ on metal surfaces, such as Cu(111), Au(111) and Ag(111), with cyano group on top of metal atoms.[33, 34] In configuration (e), the central benzene ring of F4-TCNQ adopts laterally the relative position to the top layer graphene reminiscently to the Bernal stacking of the graphene layers via π-π interaction in graphite. As a reference, we also calculate the similar adsorption configurations of 2,3,5,6-tetrafluorobenzene on the graphene. The adsorption energy of configuration (e) is 0.37 eV, which is about 0.03~0.08 eV larger than that of other configurations.

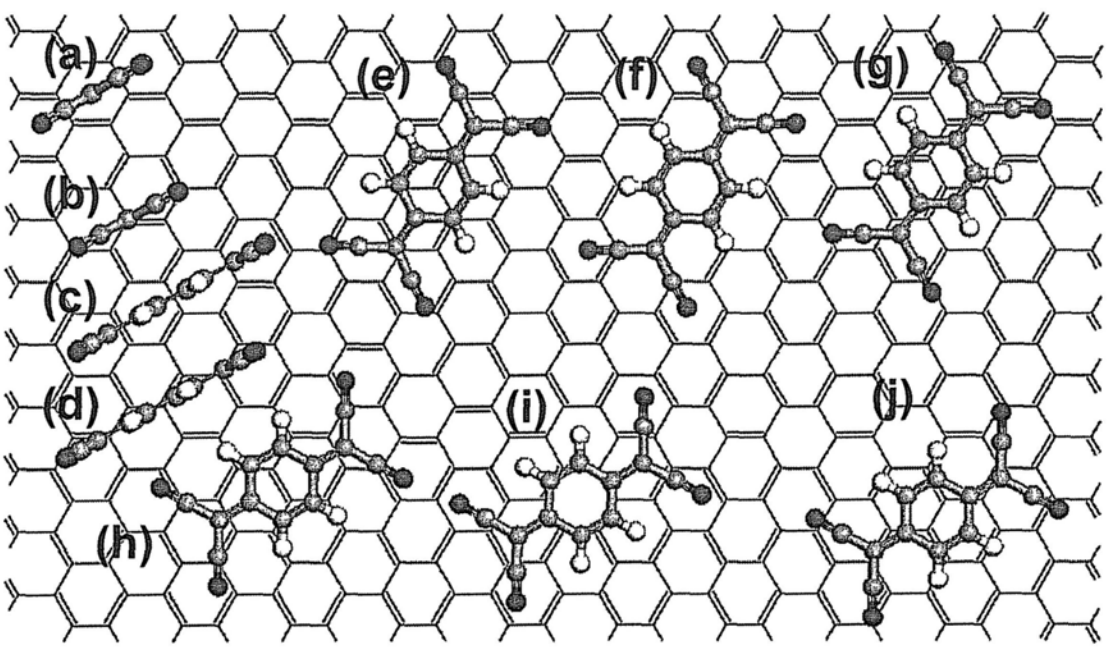

Figure 4.1 Top view of ten adsorption configurations for F4-TCNQ molecules on bilayer graphene. Nitrogen and fluorine atoms correspond to dark and light blue, carbon atoms of F4-TCNQ molecule are gray, and carbon atoms of the top graphene layer are red.

Table 4.1 Calculated adsorption energies of ten adsorption configurations for F4-TCNQ on bilayer graphene by DFT_LDA: (1) ΔE_1(eV) for the low coverage; (2) ΔE_2(eV) for the high coverage.

	a	*b*	*c*	*d*	*e*	*f*	*g*	*h*	*i*	*j*
ΔE_1(eV)	1.26	1.29	1.27	1.25	1.95	1.82	1.81	1.85	1.93	1.90
ΔE_2(eV)	0.72	0.90	0.69	0.88	1.28	1.15	1.27	1.35	1.39	1.24

4.3.2 Analysis of Band Structures of F4-TCNQ Doped Graphene at Low Coverage.

To interrogate the influence of F4-TCNQ adlayer on the electronic structure of graphene, the band structure of F4-TCNQ doped graphene with configuration (e) is calculated and depicted in Figure 4.2(a). The Dirac energy level (E_D) is around 160 meV above the Fermi level, which suggests that the molecular adlayer has introduced an efficient p- type doping effect into the graphene. A direct band gap opening of E_g = 149 meV is found, which turns to be ΔE_K = 155 meV at the Dirac point. The illustration of the band parameters including ΔE_K, E_g and γ_1 are described in Figure 4.3(a). The band structure of bilayer graphene near the K point consists of four parabolic bands.[9-14, 35] Here, E^{v1} and E^{v2} are defined as the highest and second highest occupied π orbitals. E^{c2} and E^{c2} denote the lowest and second lowest unoccupied π orbitals. E^{c1} and E^{v1} are separated by ΔE_K at the *K* point, while the minimum separation of band gap is denoted by E_g. For a pristine bilayer graphene, both ΔE_K and E_g are equal to 0 from the band structure calculation, as depicted in Figure 4.2(c). The other two bands E^{c2} and E^{v2} are separated by $2\gamma_1$. Here, γ_1 denotes the graphene interlayer tunneling energy.

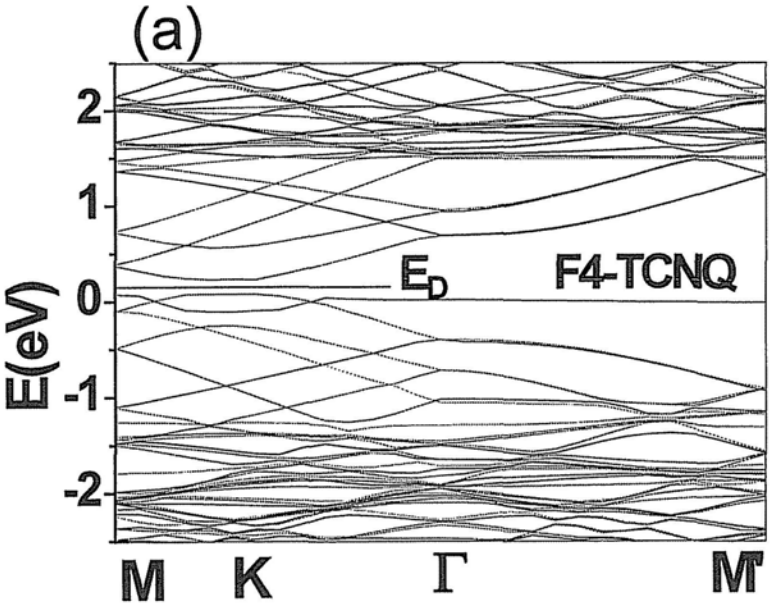
(a)
2
1
0
-1
-2
E(eV)
E_D
F4-TCNQ
M
K
Γ
M'

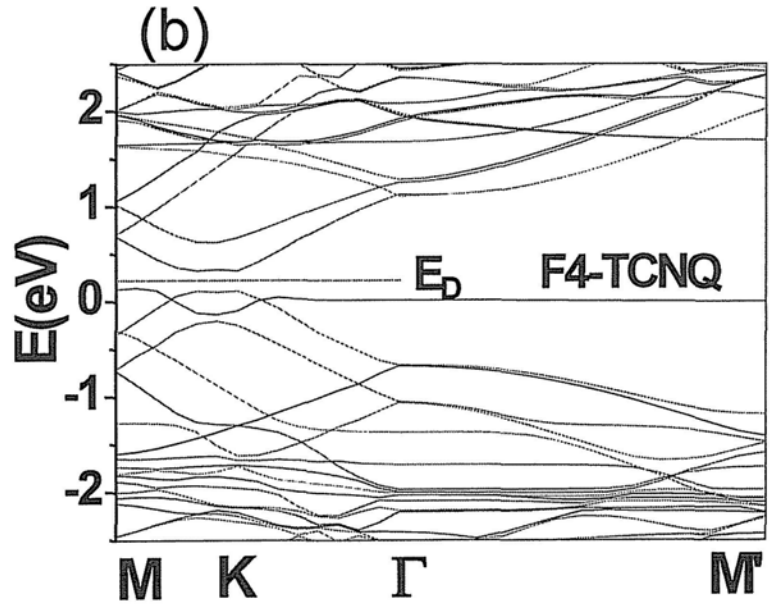
(b)
2
1
0
-1
-2
E(eV)
E_D
F4-TCNQ
M
K
Γ
M'

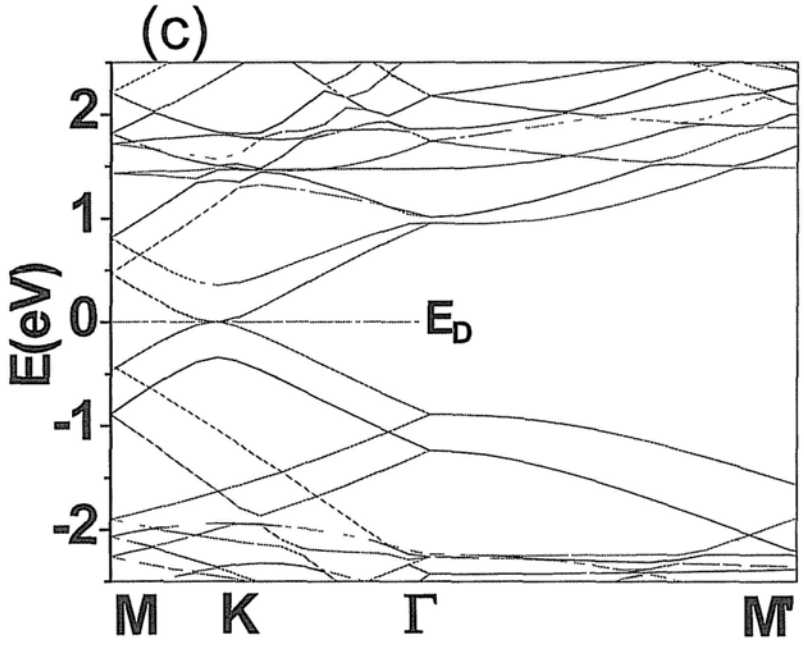

Figure 4.2 Band structure of F4-TCNQ molecule doped bilayer graphene and pristine bilayer graphene: (a) under the low coverage; (b) under the high coverage; (c) pristine bilayer graphene. The Fermi level is set to Zero.

(a)

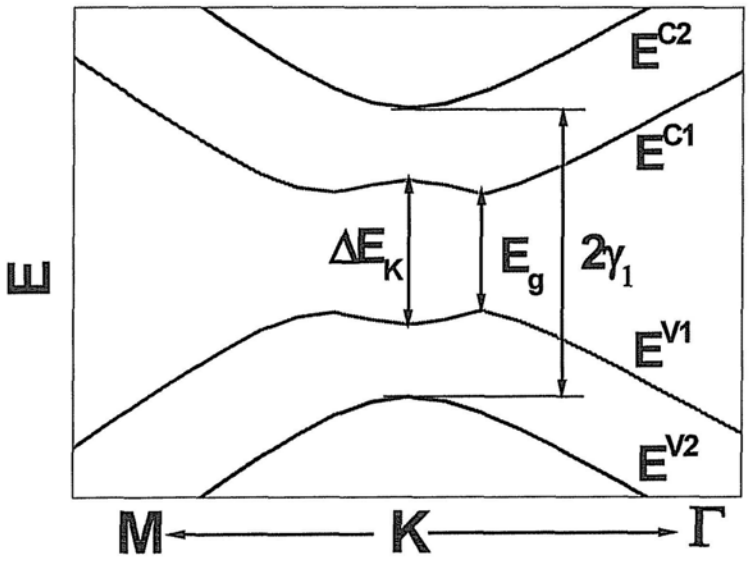

(b)

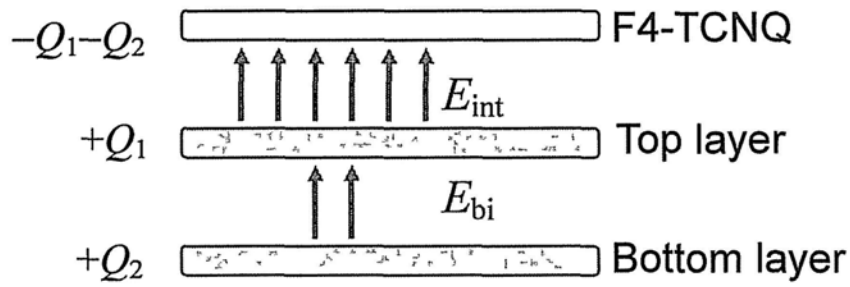

Figure 4.3 Band gap opening principles of F4-TCNQ molecule doped bilayer graphene: (a) band parameters; (b) built-in electric field distribution at zero bias.

As calculated, each F4-TCNQ molecule attains $0.63e$ from the graphene. The LUMO of F4-TCNQ is partially filled due to the charge transfer shown in the band structure. Between the top and bottom layers of the graphene, F4-TCNQ molecule could introduce a net electric field $E^* = E_{bi}$, where E_{bi} is the built-in electric field between the two graphene layers induced by the bottom layer charge Q_2. The net electric field E^* breaks the potential equivalence as shown in Figure 4.3 (b), since F4-TCNQ obtains the total charge of Q_1+Q_2 from the top (Q_1) and bottom (Q_2) layer graphene. E_{int} is the total electric field between the F4-TCNQ and graphene top layer. Actually, E^* could be estimated by tight binding model $E^* \approx \Delta E_K / d$ [10], where d is the distance between the inter layers of graphene. The build-in electrostatic field is approximately perpendicular to graphene surface as shown in Figure 4.3 (b), solely due to the charge redistribution induced by F4-TCNQ adsorption. This interfacial electric field yields the asymmetry between the two graphene layers and results in a significant band-gap opening .

4.3.3 Adsorption Configurations of F4-TCNQ on Bilayer Graphene at High Coverage.

In addition to F4-TCNQ adlayer at low coverage, the high coverage of F4-TCNQ adsorption on the graphene bilayer is investigated to provide a further

comparison. The adsorption energies for ten configurations, together with those at low coverage, are presented in Table 1. When increasing the coverage, the larger intermolecular repulsion force results in the increased total energy of molecule-substrate system, which are ascribed to the calculated average adsorption energies reduction of ~0.6 eV. Contrarily, the competition between the molecule-substrate interaction and intermolecular interaction brings about the transition of the most thermodynamically stable configuration from configuration (e) to configuration (i). In contrast to the low coverage adsorption, the most stable site is found to be site (i) according to its 0.98 eV adsorption energy, which is around 0.08~0.26 eV larger than other lying down ones obtained from MM calculation. As far as the optimized configuration (i) is concerned, the molecule is slightly rotated with respect to the graphene hexagonal ring due to the intermolecular repulsion force as shown in Figure 4.4. The intermolecular separation is 3.2 Å. Likewise, the adsorption energy of the standing-up configuration is around 0.48 eV smaller than the lying-down ones. Although these energies are about 0.14 eV smaller than that in the low coverage, they are large enough to prevent the transition from the lying-down to standing-up configurations. The adsorption energies of four standing-up configurations are around 0.58 eV lower than the lying-down ones from the MM calculation results.

(a)

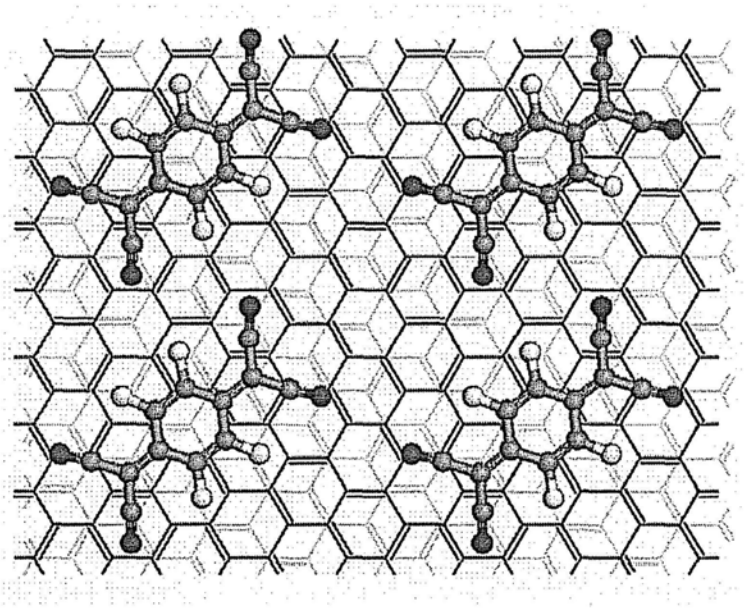

(b)

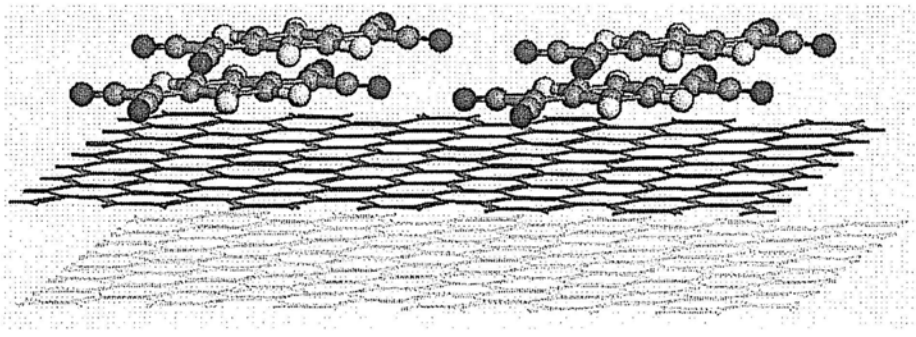

Figure 4. 4 Optimized structure of F4-TCNQ on bilayer graphene under the high coverage with 2×2 replicated cells: (a) top view and (b) side view. Nitrogen atoms are dark blue, fluorine atoms are light blue, carbon atoms of F4-TCNQ molecule are gray, carbon atoms of the top graphene layer are red, and carbon atoms of the bottom graphene layer are green.

4.3.4 Comparison of Band Gap Opening Energy between Low and High Coverages.

Under the high coverage, each molecule could gain 0.45*e* from the graphene. The E_D is enlarged to around 223 meV above the Fermi level, which suggests that the

p-type doping effect has been enhanced, compared to E_D = 160 meV for the low coverage. As depicted in Figure 4.2(b), it is found that a band gap opening (E_g) and the gap at the Dirac point K (ΔE_K) are found to be 213 meV and 236 meV respectively. E^* and E_{bi} between the two graphene layers are equal, around 0.070 V/Å. In comparison with the low coverage as shown in Figure 2(a), the band gap opening is markedly enhanced.

4.3.5 Influence of F4-TCNQ Doping on Graphene Mobility.

From the band structure, we could estimate the effective mass m^* of graphene electrons.[36] The m^* is inversely proportional to the second derivative of the energy band dispersion. Near K point, the m^* of F4-TCNQ doped bilayer is around 1.27 times that of pristine bialyer. Based on the Drude model that the mobility μ is inversely proportional to m^*, so μ has been reduced around 21% by F4-TCNQ doping. Considering the mobility varies up to one order in graphene[3], we could discover that the mobility deformation induced by F4-TCNQ is moderate.

4.3.6 Electric Fields Effects on Band Gap Opening of F4-TCNQ Doped Graphene Bilayer.

To further manipulate the interfacial electronic structure between F4-TCNQ and graphene, the electric displacement field (D) in the range of –0.3 ~ 0.3 V/Å is applied perpendicularly to the graphene basal plane, corresponding to E_{ext} of -0.077~0.077 V/Å, if SiO_2 relative dielectric constant ε_r =3.9 used as the standard ($D = \varepsilon_r\varepsilon_0 E_{ext}$), where ε_0 is vacuum permittivity. The breakdown E_{ext} limit of SiO_2 is 0.1 V/Å, and D strength of 0.27 V/Å was achieved in recent experiment.[9]

Since the electric field could alter the charge transfer between F4-TCNQ and graphene, the hole doping level will be enhanced or decreased, corresponding to the

shifting up or down of the Dirac point relative to the Fermi level. Furthermore, the net electric field between the top and bottom layers of graphene could be tuned by an externally applied electric field, which means that the inequivalence of the top and bottom layers will be manifested. Under this condition, the net electric filed between the top and bottom layers is $E^* = (E_{bi}+\varepsilon_r E_{ext}-E_{scr})$, where E_{ext} is the externally applied electric field and E_{scr} is the screening electric field in bilayer graphene (opposite to E_{ext}) by the induced charge. A negative E_{ext} will facilitate the electron transfer from the graphene to F4-TCNQ, while a positive E_{ext} will induce the opposite process. From Figure 4.5, we could find that the HOMOs under negative E_{ext} and zero bias mainly localize around F4-TCNQ, and the HOMO under positive E_{ext} distributes on both F4-TCNQ and graphene due to F4-TCNQ releasing charge to graphene. The charge transfer between the graphene and F4-TCNQ is in the range of 0.62~0.26e, in response to -0.077~0.077 V/Å E_{ext} variation. γ_1 is in the range of 414~426 meV, following -0.077~0.077 V/Å E_{ext}. By comparison, calculated γ_1 of a pristine bilayer is 350 meV, which is in good agreement with experiments.[37, 38] In the pristine bilayer, the net electric field between the top and bottom layers is $E^* = (\varepsilon_r E_{ext}-E_{scr})$. The band gap opening versus E_{ext} of the pristine bilayer is depicted in Figure 4.6(a), slightly smaller than the experimental values,[9] but in reasonable agreement. The relationship between the band gap opening versus E_{ext} for the F4-TCNQ doped bilayer under the high coverage is shown in Figure 4.6(b). A positive electric field obviously increases the band gap opening of the graphene, whereas a negative electric field reduces it, because the positive electric field constructively entrenches the E^*, while the negative electric field destructively rescinds it. As ΔE_K is increased, the calculated band gap also asymptotically follows[11]:

$$E_g \approx \Delta E_K \gamma_1 \Big/ \sqrt{\Delta E_K^2 + \gamma_1^2} \qquad (2)$$

(a)

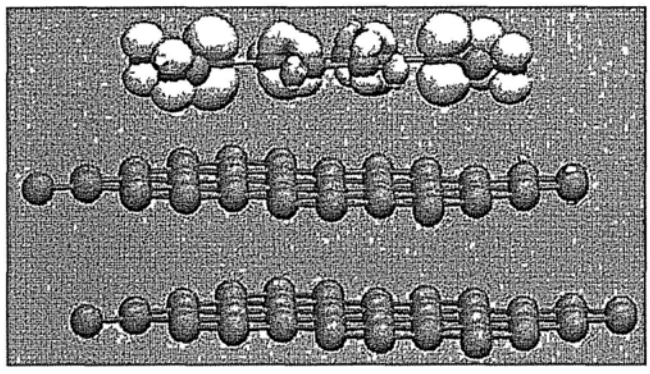

(b)

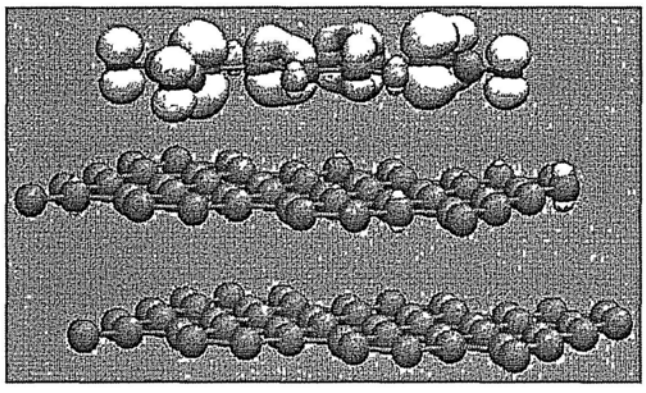

(c)

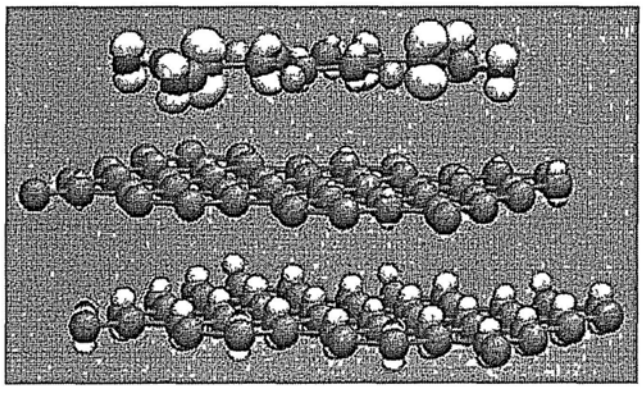

Figure 4.5 0.02 e/ $Å^3$ isosurface of charge redistribution induced by E_{ext}: (a) HOMO of -0.3 V/Å case; (b)) HOMO of zero bias case; (c) HOMO of 0.3 V/Å case.

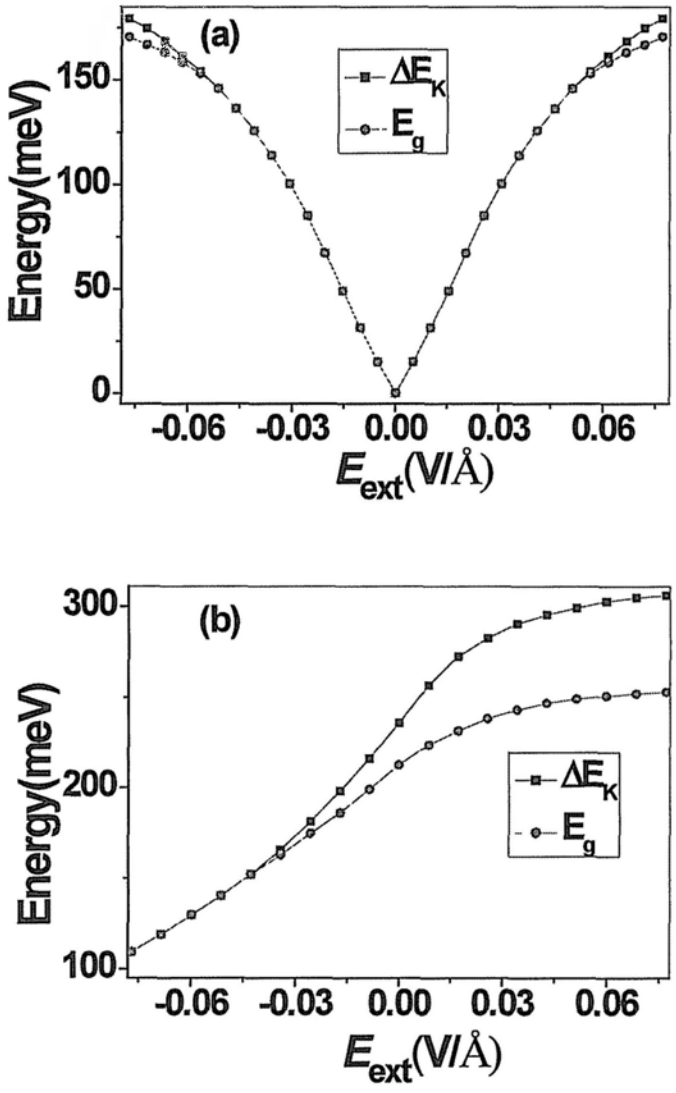

Figure 4.6 Effects of E_{ext} on band gap opening of bilayer graphene: (a) pristine bilayer; (b) F4-TCNQ molecule doped bilayer.

For a pristine bilayer, ΔE_K = 179 meV and E_g = 170 meV at 0.077 V/ Å, with E^* of around 0.054 V/Å. By comparison, in the case of the doped bilayer with the high concentration of F4-TCNQ, ΔE_K = 236 meV and E_g = 213 meV at zero bias, with E^* of 0.070 V/Å. At 0.077 V/Å, the gap openings of F4-TCNQ doped bilayer are enlarged to be ΔE_K = 306 meV and E_g = 253 meV, with E^* = 0.095 V/Å.

4. 4 Conclusion

In summary, we have used the first principles technique to investigate the interfacial electronic structure between F4-TCNQ adlayer and bilayer graphene. *P*-type bilayer graphene is obtained by F4-TCNQ molecular doping. The built-in electric field E^* between the two graphene layers by high F4-TCNQ doping could reach 0.070 V/Å, along with the gap openings ΔE_K = 236 meV and E_g = 213 meV. With E_{ext} of 0.077 V/Å, the gap openings of the doped graphene are ΔE_K = 306 meV and E_g = 253 meV, around 71% and 49% higher than their respective values for the pristine graphene bilayer under the same E_{ext}.

References

(1) Novoselov, K. S.; Geim, A. K.; Morozov, S. V.; Jiang, D.; Zhang, Y.; Dubonos, S. V.; Grigorieva, I. V.; Firsov, A. A. *Science* **2004**, *306*, 666-669.

(2) Castro Neto, A. H.; Guinea, F.; Peres,N. M. R.; Novoselov, K. S.; Geim, A. K. *Rev. Mod. Phys.* **2009**, *81*, 109-162.

(3) Geim, A. K. and Novoselov, K. S. *Nature Mater.* **2007**, *6*, 183-191.

(4) Pan, Y. ; Zhang, H. G.; Shi, D. X.; Sun, J. T.; Du, S. X.; Liu, Fe.; Gao, H. J. *Adv. Mater.* **2009**, *21*, 2777-2780.

(5) Yang, L.; Deslippe, J.; Park, C.-H.; Cohen, M. L.; Louie, S. G. *Phys. Rev. Lett.* **2009**, *103*, 186802-186805.

(6) Kudin, K. N.; Ozbas, B; Schniepp, H. C.; Prud'homme, R. K.; Aksay, I. A.; Car, R. *Nano Lett.* **2008**, *8*, 36-41.

(7) Yan, J; Zhang, Y.; Kim, P.; Pinczuk, A. *Phys. Rev. Lett.* **2007**, *98*, 166802-166805.

(8) Yan, Q. M.; Huang, B.; Yu, J.; Zheng, F. W.; Zang, J.; Wu, J.; Gu, B. L.; Liu, F.; Duan, W. H. *Nano Lett.* **2007**, *6*, 1469-1473.

(9) Mak, K. F.; Lui, C. H.; Shan, J.; Heinz, T. F. *Phys. Rev. Lett.* **2009**, *102*, 56405-56408.

(10) Gava. P.; Lazzeri, M.; Saitta, A. M.; Mauri, F.; *Phys. Rev. B* **2009**, *79*, 165431-165443.

(11) Min. H; Sahu, B.; Banerjee, S. K.; MacDonald, A. H. *Phys. Rev. B* **2007**, *75*, 155115-155121.

(12) McCann, E. *Phys. Rev. B* **2006**, *74*, 161403(R)-161406.

(13) Castro, E. V.; Novoselov, K. S.; Morozov, S. V.; Peres, N. M. R.; Lopes dos, Santos J. M. B.; Nilsson, J.; Guinea, F.; Geim, A. K.; and Castro Neto, A. H. *Phys. Rev. Lett.* **2007**, *99*, 216802-216805.

(14) Avetisyan, A. A.; Partoens, B.; Peeters, F. M. *Phys. Rev. B* **2009**, *79*, 035421-035427.

(15) Ohta, T. ; Bostwick, A. ; Seyller, T.; Horn, K; Rotenberg, E. *Science* **2006**, *313*, 951-954.

(16) Gierz, I.; Riedl, C.; Starke, U.; Ast, C. R.; Kern, K.; *Nano Lett.* **2008**, *8*, 4603-4607.

(17) Elias, D. C.; Nair, R. R.; Mohiuddin, T. M. G.; Morozov, S. V.; Blake, P.; Halsall, M. P.; Ferrari, A. C.; Boukhvalov, D. W.; Geim, A. K.; and Novoselov, K. S. *Science* **2009**, *323*, 610-613.

(18) Zhou, J.; Wu, M. M.; Zhou, X.; and Sun, Q. Appl. Phys. Lett. **2009**, *95*, 103108-103110.

(19) Sofo, J. O.; Chaudhari, A. S.; and Barber, G. D. Phys. Rev. B **2007**, 75, 153401-153404.

(20) Lu, Y. H.; Chen, W.; Feng, Y. P.; He, P. M. *J. Phys. Chem. B.* **2009**, *113*, 2-5.

(21) Manna, A.K; and Pati, S.K. *Chem. Asian J.* **2009**, *4,* 855-860

(22) Varghese, N.; Ghosh, A.; Voggu, R.; Ghosh, S.; and Rao, C. N. R. *J. Phys. Chem. C* **2009,** *113,* 16855-16859.

(23) Dalosto, Sergio. D.; Levine, Z. H. *J. Phys. Chem. C* **2008,** *112,* 8196-8199

(24) Chen, W.; Chen, S.; Qi, D. C.; Gao, X. Y.; Wee, A. T. S. *J. Am. Chem. Soc.* **2007**, *129*, 10418-10422.

(25) Nosho, Y.; Ohno, Y.; Kishimoto, S.; Mizutani. T. *Nanotechnology* **2007**, *18* 415202-415205.

(26) Pinto, H.; Jones, R.; Goss, J. P.; Briddon, P. R. *J. Phys.: Condens. Matter* **2009**, 21, 402001-402003.

(27) Kresse, G.; Furthmu¨ller J. *Comput. Mater. Sci.* **1996**, *6*, 15-50.

(28) Kresse, G.; Joubert, D.; *Phys. Rev. B* **1999**, *59*, 1758-1775.

(29) Rochefort, A.; and Wuest, J. D., *Langmuir* **2009**, *25*, 210-215.

(30) Li, M. M.; Zhang, J.; Li, F. J.; Zhu, F. X.; Zhang, M.; and Zhao, X. F. *Phys. Status Solidi C* **2009**, *6*, s90-s93

(31) Shi, D. X.; Ji, W.; Lin, X.; He, X. B.; Lian, J. C.; Gao, L. ; Cai, J. M.; Lin, H.; Du, S. X.; Lin, F.; Seidel, C.; Chi, L. F.; Hofer, W. A.; Fuchs, H.; and Gao, H.-J. *Phys. Rev. Lett.* **2006**, *96*, 226101-226105.

(32) Ulbricht,H.; Moos, G.; and Hertel, T. *Phys. Rev. Lett.* **2003**, *90*, 095501-095504.

(33) Romaner, L.; Heimel, G.; Bre´das, J. L.; Gerlach, A.; Schreiber, F.; Johnson, R. L.; Zegenhagen, J.; Duhm, S.; Koch, N.; Zojer, E. *Phys. Rev. .Lett.* **2007**, *99*, 56801-56804.

(34) Rangger, G. M.; Hofmann, O. T.; Romaner, L.; Heimel, G.; Bröker, B.; Blum, R. P.; Johnson, R. L.; Koch, N.; Zojer, E *Phys. Rev. B* **2009**, *79*, 165306-165317.

(35) Malard, L. M.; Nilsson, J.; Elias, D. C.; Brant, J. C.; Plentz, F.; Alves, E. S.; Castro Neto, A. H.; Pimenta, M. A. *Phys. Rev. B* **2007**, *76*, 201401(R)-201404(R).

(36) Wallace, P. R. *Phys. Rev.* **1947**, *71*, 622-634.

(37) Kuzmenko, A. B.; Van Heumen, E.; Van der Marel, D.; Lerch, P.; Blake, P.; Novoselov, K. S.; Geim, A. K. *Phys. Rev. B* **2009**, *79*, 115441-115445.

(38) Malard, L. M.; Nilsson, J.; Elias, D. C.; Brant, J. C.; Plentz, F.; Alves, E. S.; Castro Neto, A. H.; Pimenta, M. A. *Phys. Rev. B* **2007**, *76*, 201401-201404.

Chapter 5 Self-Assembly of PTCDA Ultrathin Films on Graphene: Structural Phase Transition and Charge Transfer Saturation

5. 1 Introduction

Graphene sheet, a two dimensional crystal constructed by sp^2 hybridization of carbon atoms, has attracted significant attention due to its extremely high carrier mobility, ballistic charge transport characteristics, and quantum relativistic phenomena.[1-8] The band structure of single-layer graphene exhibits as circular cone near six corner points K (K') of its first Brillouin zone. The graphene sheet whose π and π^* bands of electrons intersects at the Dirac points has a zero band gap attribute of semiconductor or semimetal. The intrinsic zero band gap characteristic has limited the potential applications of graphene in future nano-electronics. Chemical functionalizations of graphene are perceived to effectively modulate the electronic structure of graphene to attain the intended properties which will be exploited for the potential applications of graphene in nanoelectronics.

Atomic doping of graphene by depositing potassium and gold atoms onto graphene could be used for n and p type graphene semiconductors, respectively,[9, 10] and superconducting phase could be obtained by Sn cluster decorating.[11] However, atomic doping could cause clustering of doping species, severe structural conformation and defects into graphene. Surface fuctionalization of graphene by organic molecules, especially aromatic molecule doping, is a feasible route to tackle these problems. Recently 1,3,6,8-pyrenetetrasulfonic acid (TPA) functionalized single-layer graphene was experimentally exfoliated. And it was found that the interaction between a TPA and the graphene could induce G-band splitting.[12]

Meanwhile, an *n* type molecular semiconductor PTCDA was deposited onto graphene surface at room temperature. It was found that the molecules possess long-range order with a herringbone arrangement, the molecular ordering is unperturbed by defects in the epitaxial graphene or atomic steps in the underlying SiC surface.[13] *In-situ* low-temperature scanning tunneling microscopy (LT-STM) and high-resolution *x*- ray photoemission spectroscopy are used (HR-XPS) to study the growth of PTCDA thin films on epitaxial graphene (EG) on 6H-SiC(0001), and it was revealed that there is a weak charge transfer between PTCDA and EG.[14] PTCDA has also fall into research interest of its initial growth morphology and electronic structure on metal, insulator, and semiconductor surfaces.[15-24] One of PTCDA's derivatives 3,4,9,10-perylene tetracarboxylic acid (PTCA) was used to functionalize graphene, and atomic layer deposition of dielectric Al_2O_3 on graphene on a micron scale was achieved.[25]

Accordingly, the stable and uniform PTCDA functionalized graphene may provide new opportunities for graphene-based electronics. However, the growth and doping mechanisms have yet not been elucidated. Here, we use state-of-the-art first principles technique to address the doping effect and growth mechanism of PTCDA on graphene. Our calculation results of the optimized structures prove that the well-ordered PTCDA monolayers naturally self-assemble on single-layer graphene, and the formation of herringbone orientation is attributed to the densely disposed intermolecular hydrogen bonds. In order to better understand the intriguing interface features, typical defects of graphene are considered. And it is found that they render very limited conformation to the monolayer, which is in good agreement with experiment.[13] We also find that the growth of PTCDA monolayers, obeys SK mode and a phase transition appears when the coverage approaches 2~3 MLs. Meanwhile, the calculation of band structure shows that the functionalized graphene behaves as *p*-type semiconductor and posses an intrinsic band gap. This study ameliorates the understanding of organic ultrathin films on graphene, and could inspire further design and fabrication of graphene based devices.

5. 2 Calculation Method

The calculations are performed within *Vienna ab initio simulation package* (VASP).[26] The electron-ion interaction is described by PAW method.[27] 29.40 Ry is used as the plane-wave basis set cutoff. Local density approximation (LDA) is better than generalized gradient approximations (GGA) in weak binding systems.[28,29] Therefore LDA is used. Our calculated graphite lattice constants are a = 2.445 Å and c =6.627 Å, in good agreement with experimental values a =2.462 Å and c =6.710 Å. But LDA does not take into account of the van der Waals interactions, and the ability to match the experimental interlayer spacing is due to a coincidental cancellation of errors. In order to better understand the growth process, we also conduct molecular mechanics (MM) calculations.[30, 31] MM^+ force field, which is improved from MM2, is used in MM calculations. Another method to take into account of the van der Waals interactions is to use DFT plus long range dispersion term.[32, 33] Graphene $5\sqrt{3}\times8$ single-layer is used as substrate to simulate PTCDA molecule adsorption at single molecular level, which also corresponds to 0.3 ML adlayer, while a graphene $5\sqrt{3}\times5$ single-layer plus two molecules are used to simulate PTCDA monolayer adsorption. The molecule and graphene atoms are allowed to relax until residual forces in all direction are less than 20 meV/Å. A 1.8 nm vacuum layer is used to eliminate the longitudinal interactions between super cells. 4×4×1 and 4×6×1 Monkhorst-Pack k-point meshes are used for low and high coverage cases, respectively.

For PTCDA 0.3 ML adlyaer on graphene, nine adsorption configurations with different orientations are considered. The adsorption energy is calculated by the following equation:

$$E_{ad}{}^{0} = -(E - E_0 - E_{molecule}) \qquad (1)$$

where E is the total energy of the single-layer graphene with the molecule; $E_{molecule}$ is the chemical potential of the molecule; E_0 is the total energy of pristine single-layer graphene.

5. 3 Results and Discussion

5.3.1 Adsorption of Single PTCDA Molecule on Graphene

The structural optimization result for most stable adsorption mode is shown in Figures 5.1(a) and (b). The single PTCDA molecule adsorption on graphene is thermodynamically stable under this structure due to its adsorption energy is E_{ad}^{0} = 1.20 eV and around 0.06~0.25 eV larger than other configurations. The vertical distance (averaged to each atom) between PTCDA and graphene is 3.11 Å. To investigate the PTCDA doping effects on graphene, the band structure for isolated PTCDA on graphene is shown in Figure 5.2(a). The Dirac energy level E_D is 160 meV higher than the Fermi level, and the band gap is 136 meV. As a result, PTCDA functionalized graphene shows p type semiconductor characteristics. Furthermore, each PTCDA molecule gains 0.30 electrons from graphene.

(a)

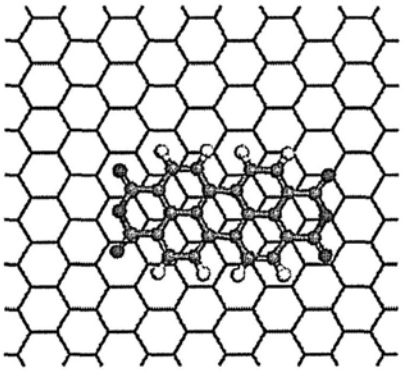

(b)

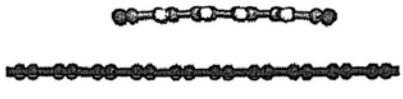

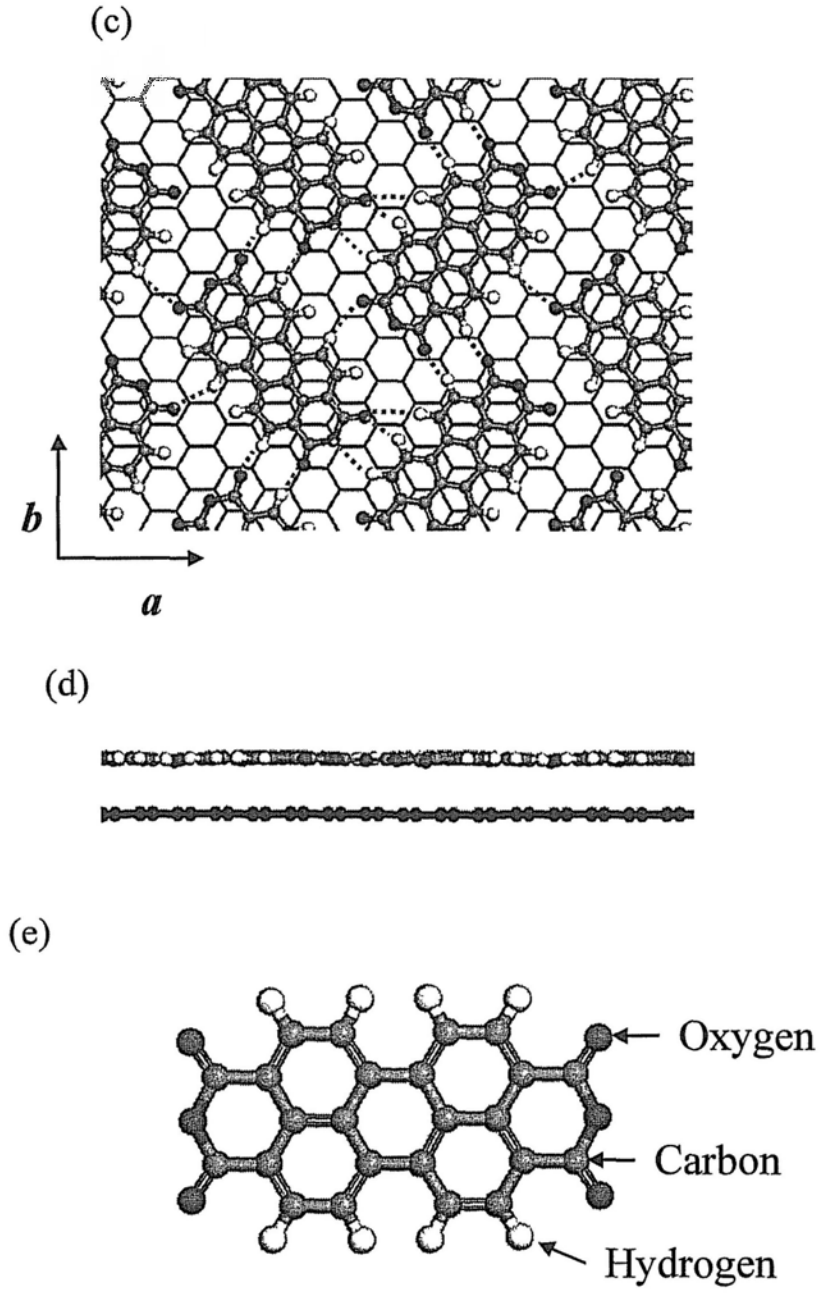

Figure 5.1 Calculated structures of PTCDA on graphene at different areal concentration: (a) top view and (b) side view of 1/3 ML; (c) top view and (d) side view of 1 ML. (e) structure of PTCDA molecule. Oxygen atoms are blue, hydrogen atoms are white, carbon atoms of PTCDA are green, and carbon atoms of graphene are black. Red dashed lines are hydrogen bonds.

(a)

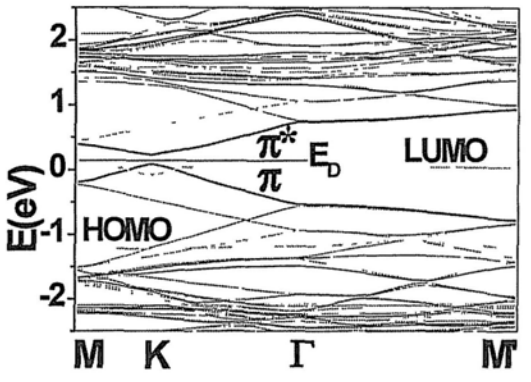

(b)

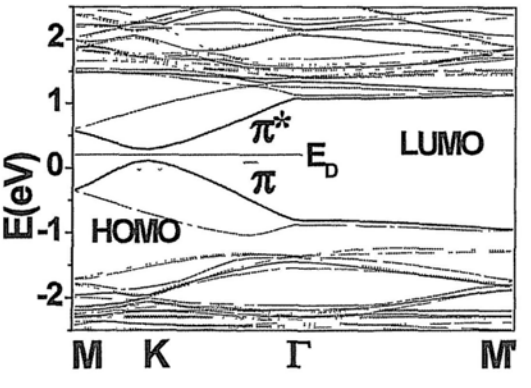

Figure 5.2 Band structure of PTCDA doped graphene at different areal concentration: (a) 0.3 ML (b) 1 ML.

5. 3.2 Growth of PTCDA Monolayer on Graphene

Also PTCDA monolayer (ML) on single-layer graphene is simulated by two molecules on each graphene $5\sqrt{3} \times 5$ super cell. From experiments,[34, 35] the unit cell parameters of the monolayer are a = 19.5 Å, b = 13.2 Å. Graphene $5\sqrt{3} \times 5$ super cell with a = 21.175 Å, b = 12.225 Å is the closest geometry to the experimental unit cell. Actually there are other close unit cells such as graphene $4\sqrt{3} \times 6$ and $4\sqrt{3} \times 5$. Nevertheless, for graphene $4\sqrt{3} \times 6$, the PTCDA monolayer cannot constitute a full C-H···O hydrogen bonding network, especially in b direction with neighboring C···O

distance around 5.10 Å. To form a good hydrogen bonding, the C···O distance should be smaller than 4.0 Å.[36-38] On the other hand, for graphene $4\sqrt{3} \times 5$, the distance between atoms in neighboring molecules is too small, and the molecule will be decomposed after structural optimization. The laterally intermolecular interaction energy is defined by:

$$E_{HB} = -(E - 2E_{molecule})/2 \qquad (2)$$

where E is the total energy of the molecular monolayer, composed of two molecules per supercell, and $E_{molecule}$ is the energy of the isolated molecule. For isolated PTCDA molecular monolayer, the intermolecular interaction energy is E_{HB} = 0.78 eV, which is contributed from intermolecular hydrogen bonds. Compared to single PTCDA adsorption energy 1.20 eV, E_{HB} is around 35% smaller.

The structural optimization for PTCDA monolayer on single-layer graphene is shown in Figures 5.1(c) and (d). The average distance between PTCDA monolayer and graphene is 3.21 Å, which is 0.1 Å larger than the distance of the single PTCDA molecule adsorption on graphene. The monolayer rumpling is within 0.23 Å and the graphene rumpling is no more than 0.10 Å. PTCDA molecules are arranged as a herringbone packing to keep totally 10 hydrogen bonds between each molecule and neighboring molecules. The adsorption energy of the monolayer layer averaged to each molecule is calculated by:

$$E_{ad}^{1} = -(E - E_0 - E_{monolayer})/2 \qquad (3)$$

where E is the total energy of the single-layer graphene with monolayer adsorption; $E_{monolayer}$ is the total energy of monolayer; E_0 is the total energy of pristine single-layer graphene. The adsorption energy for each molecule is E_{ad}^{1} = 0.83 eV, which is around 0.08~0.23 eV larger than other configurations. E_{ad}^{1} is around 35% smaller than E_{ad}^{0}. For PTCDA monolayer on graphene, E_{HB} is comparable to E_{ad}^{1}. Since E_{HB} is in-plane intermolecular energy, it plays the role as driving force for PTCDA to grow in plane and on top of substrate together with E_{ad}^{1}. These two interactions: in plane intermolecular interaction and molecule-substrate interaction

help PTCDA to form a complete monolayer on graphene substrate. The relative energy stability for PTCDA monolayer to isolated PTCDA molecule adsorption is $E_{ad}^{1} + E_{HB} - E_{ad}^{0} = 0.41$ eV averaged to each molecule.

Its corresponding band structure is shown in Figure 5.2(b). Each molecule obtains 0.16*e* from graphene and is around 57% of single molecular charge transfer between PTCDA and graphene, which indicates the molecule-substrate interaction, is suppressed by increasing the coverage. The gained charge from graphene substrate mainly localizes on the carbonyl group of PTCDA as shown in Figure 5. 3. The charge difference density is defined by:

$\rho_{diff} = \rho_{total} - \rho_{molecule} - \rho_{substrate}$, where ρ_{total} refers to the charge density of substrate with molecule after adsorption; $\rho_{molecule}$ represents the charge density of molecule, and $\rho_{substrate}$ denotes the charge density of molecule before adsorption. The charge density difference is shown in Figure 5.3. PTCDA gains electron from graphene, and the gained charge mainly localizes on first PTCDA layer.

When PTCDA establishes hydrogen bonds with its 6 neighbors, its carbonyl group's chemical activity has been weakened. This results in the suppression of charge acceptor ability of PTCDA monolayer in contrast to the isolated PTCDA molecule. Similar to the variation of charge acceptor ability, the adsorption energy for PTCDA on graphene is damped due to the reduction of chemical activity by the formation of dense hydrogen bonds network.

(a)

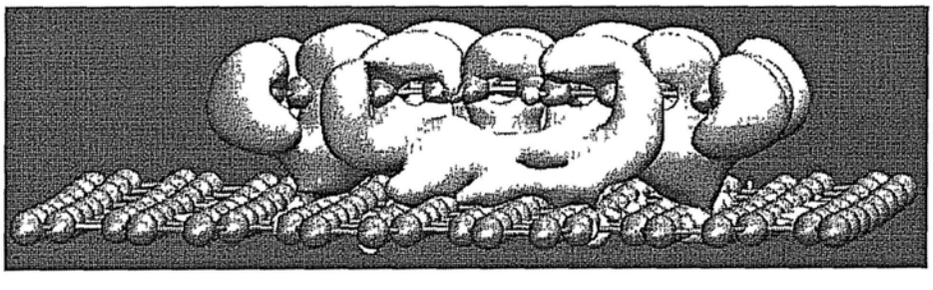

(b)

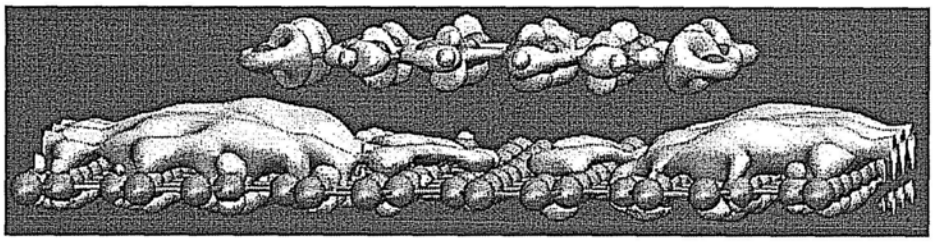

(c)

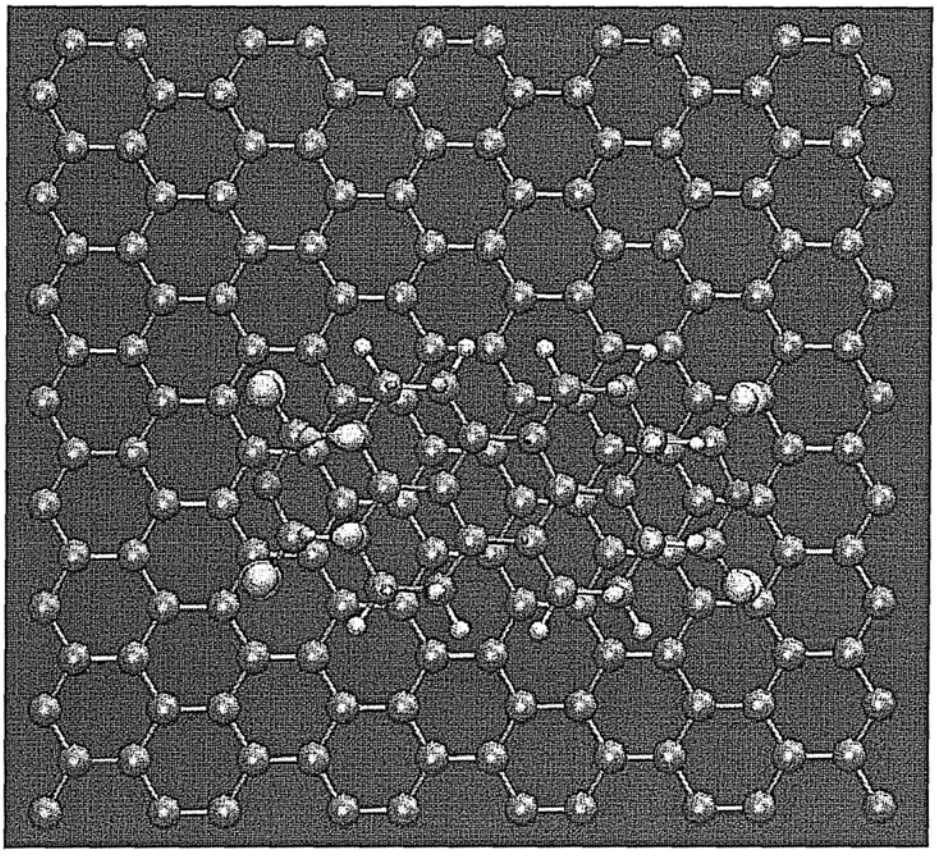

(d)

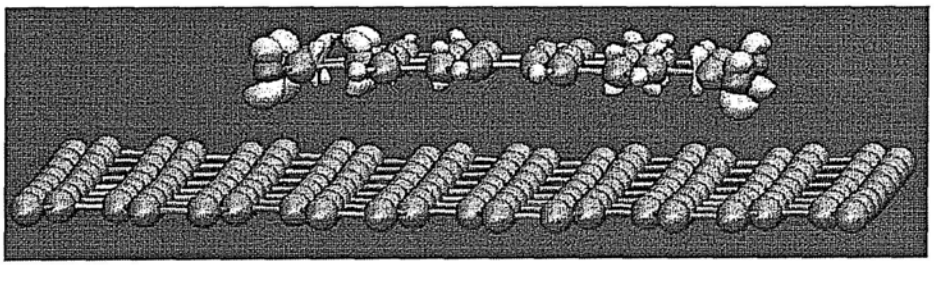

(e)

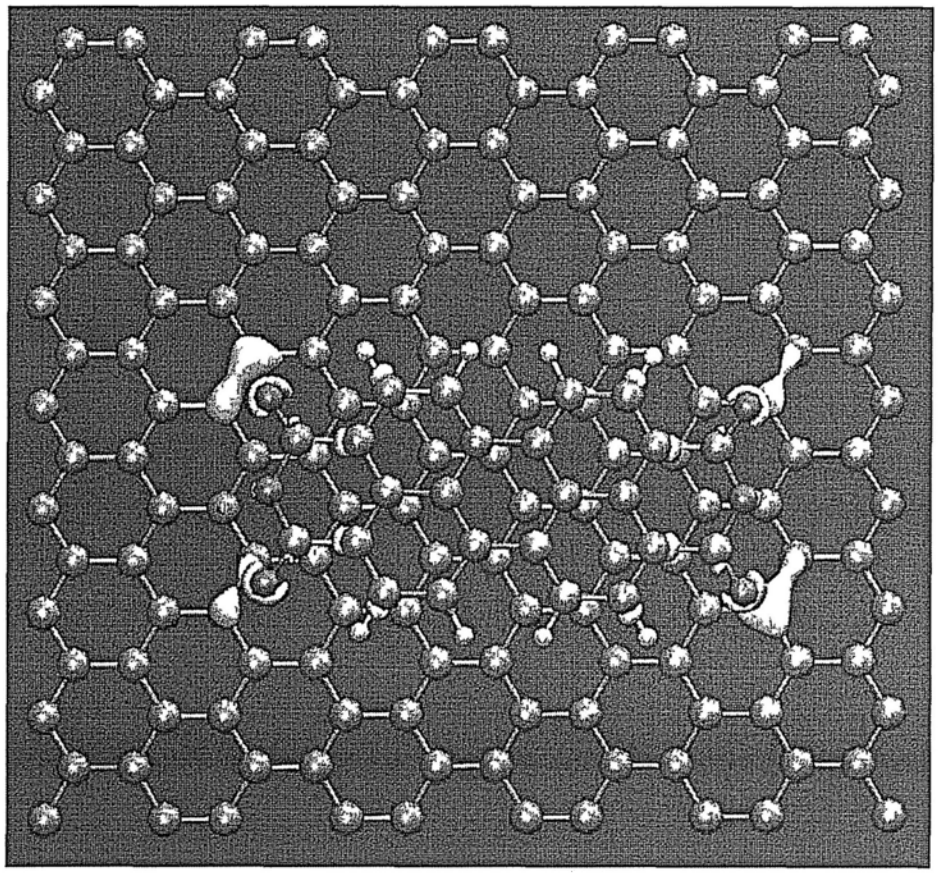

(f)

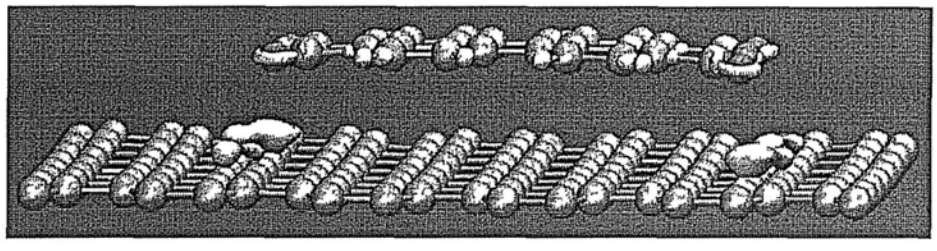

Figure 5.3 Isosurface of charge difference distribution at different densities for isolated PTCDA molecule adsorption on Graphene: (a) Side view of 0.001e/ $Å^3$ (b) Side view of -0.001e/ $Å^3$(c) Top view of 0.006 e/ $Å^3$(d) Side view of 0.006 e/ $Å^3$(e) Top view of -0.006 e/ $Å^3$(f) Side view of -0.006 e/ $Å^3$.

Although the charge transfer for each molecule is decreased, the averaged graphene surface charge density increases by 70%. The band gap of graphene is 182 meV. Therefore, by increasing the coverage of PTCDA monolayer, the band gap opening is also enhanced.

5. 3.3 Growth of PTCDA Monolayer on Defect Functionalized Graphene

To further investigate the graphene substrate interaction with PTCDA adlayer, three typical graphene defects: Stone Wales defect (*SW*), single vacancy (*SV*) and double vacancies (*DV*) in 1% concentration are considered.

The structural optimization for PTCDA adlayer on graphene with *SW* defect is shown in Figures 5. 4(a) and (b). Although the adlayer-substrate interaction has caused a strong conformation in graphene, the PTCDA adlayer remains its planar geometry. The averaged adsorption energy for each molecule is 1.03 eV, so the *SW* defect can enhance the interaction between adlayer and substrate. The averaged distance between them is 3.22 Å. But the closest distance between oxygen atom and graphene atoms is reduced to 3.05 Å, compared to 3.22Å for adlayer on pristine graphene. So it can be understood why the averaged distance is unchanged, but the adsorption energy is increased by 0.2 eV. The rumpling of PTCDA monolayer is within 0.28 Å and the rumpling of graphene is 0.78 Å. Compared to the adlayer on pristine graphene, the PTCDA adlayer adsorption induced the rumpling increment in graphene is around fourteen times that of PTCDA adlayer.

(a)

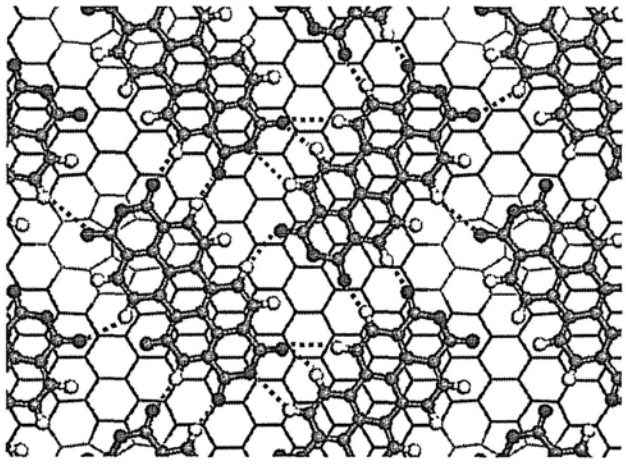

(b)

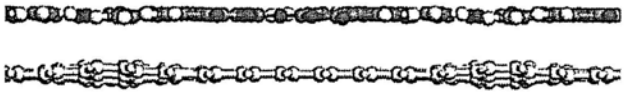

(c)

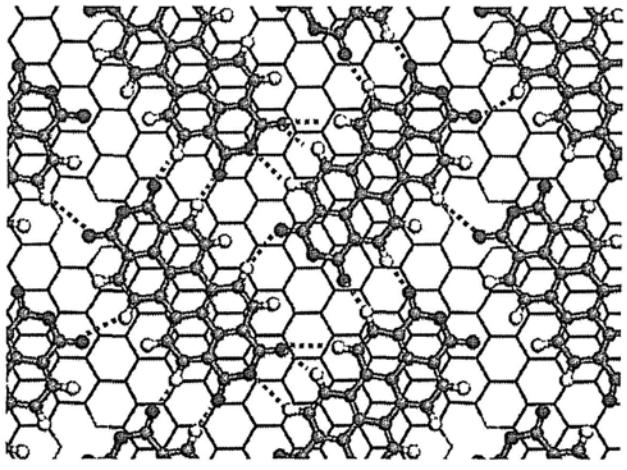

(d)

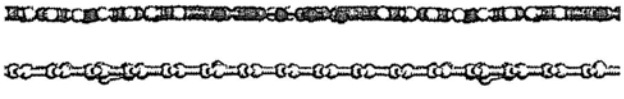

(e)

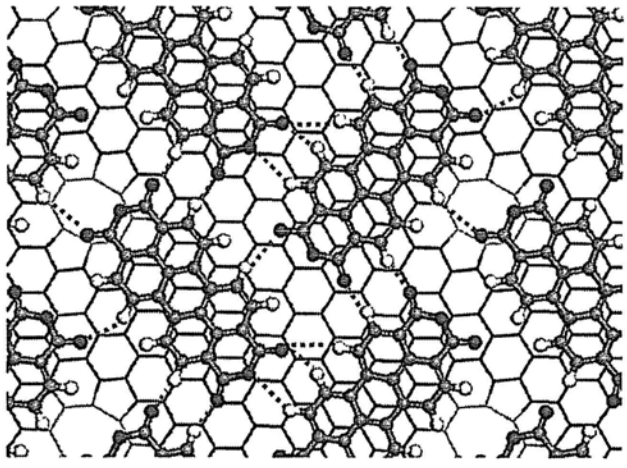

(f)

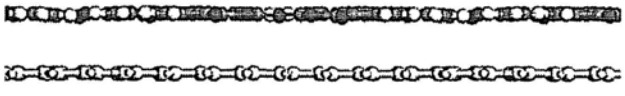

Figure 5. 4 Calculated structures of PTCDA ML on three typical defected areas: (a) and (b) *SW* defect; (c) and (d) *SV* defect; (e) and (f) *DV* defect. Defected areas are brown. Red dashed lines are hydrogen bonds.

Figures 5.4(c) and (d) show the structural optimization for PTCDA monolayer on graphene with *SV* defect. The vertical distance between PTCDA and graphene is 3.21 Å. The adsorption energy is E_{ad} = 0.96 eV, averaged to each molecule, which is 0.13 eV larger than the adsorption energy on pristine graphene. The first closest distances between oxygen atom and graphene atoms are reduced to 3.19 Å compared to that of single monolayer on graphen 3.22 Å. The monolayer rumpling on single vacancy functionalized graphene sheet is almost the same as that for monolayer on pristine one, but graphene rumpling is strongly increased by 0.38 Å.

The structural optimization for PTCDA adlayer on graphene with *DV* defect is shown in Figures 5.4(e) and (f). The vertical distance between PTCDA and graphene is 3.21 Å. The adsorption energy is 0.95 eV, averaged to each molecule, which is 0.12 eV larger than the adsorption energy on pristine graphene. The first closest distances between oxygen atom and graphene are reduced to 3.19 Å, Both the molecular and

graphene's rumpling is compared to PTCDA adlayer on pristine graphene.

To summarize, defects have very limited perturbation effects on the structural conformation of PTCDA monolayer. The PTCDA adlayer remains its planar structure on the defect areas and full hydrogen bonding network between neighboring molecules. These results corroborate experimental results that PTCDA monolayer long range ordering is unperturbed by the defects in graphene substrate.[13]

5. 3.4 Growth of PTCDA Bilayer on Graphene

The PTCDA multiple-layers on graphene are further investigated. The adsorption energies for different coverage are summarized in Tables 5.1 and 5.2. To start with, eight configurations for PTCDA bilayer on single-layer graphene are considered, with four typical optimized structures as shown in Figure 5.5.

Table 5. 1 Evolution of intermolecular and molecule-substrate interaction energies by DFT.

	E_{HB}	$E_{ad}{}^{0}$	$E_{ad}{}^{1}$	$E_{ad}{}^{2,\alpha}$	$E_{ad}{}^{2,\beta}$	$E_{ad}{}^{3,\alpha}$	$E_{ad}{}^{3,\beta}$
Energy (eV)	0.78	1.20	0.83	0.75	0.73	0.88	0.68

Table 5. 2 Evolution of intermolecular and molecule-substrate interaction energies by MM.

	E_{HB}	$E_{ad}{}^{0}$	$E_{ad}{}^{1}$	$E_{ad}{}^{2,\alpha}$	$E_{ad}{}^{2,\beta}$	$E_{ad}{}^{3,\alpha}$	$E_{ad}{}^{3,\beta}$
Energy (eV)	0.65	1.04	0.69	0.59	0.54	0.73	0.44

(a)

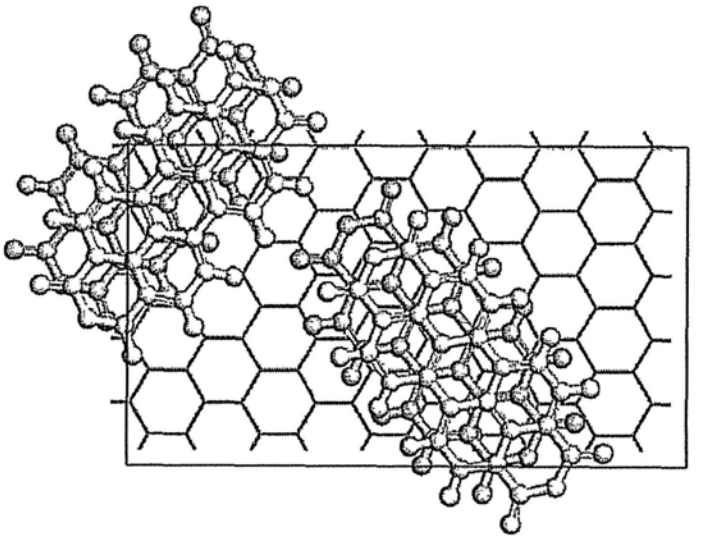

(b)

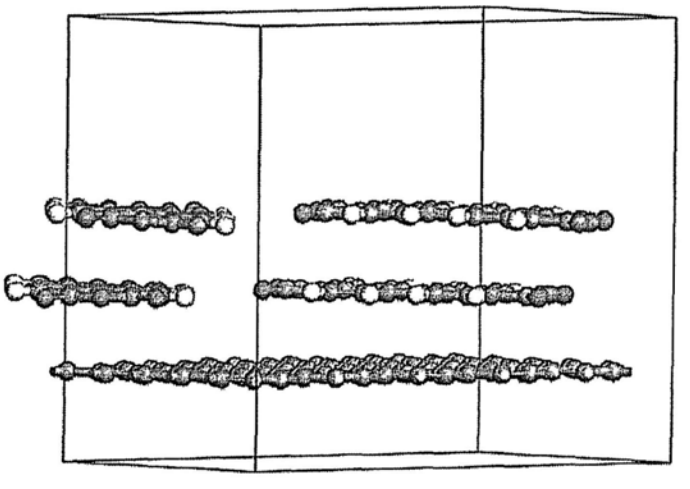

(c)

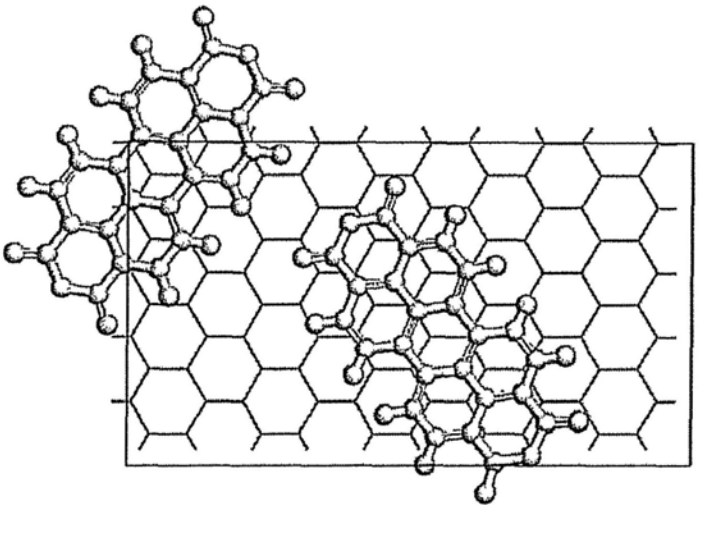

(d)

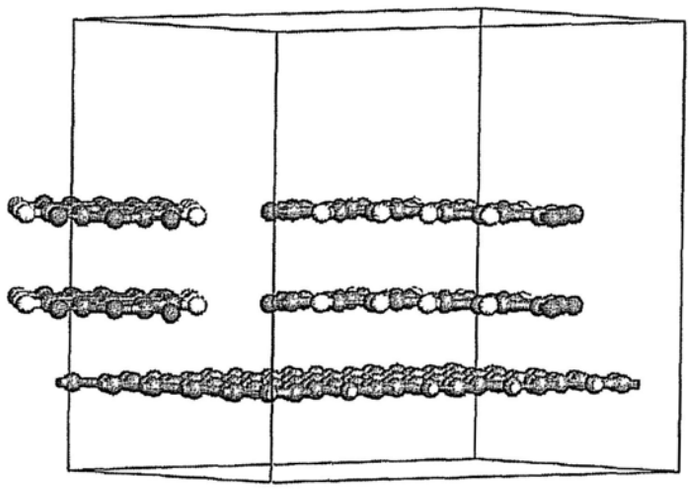

(e)

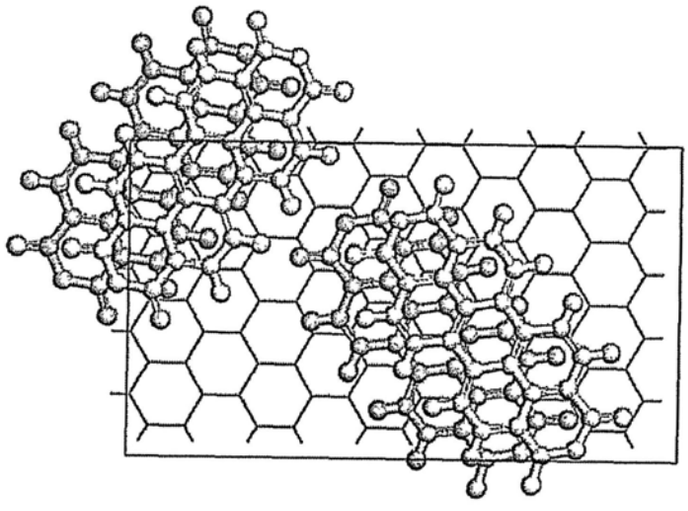

α modification

(f)

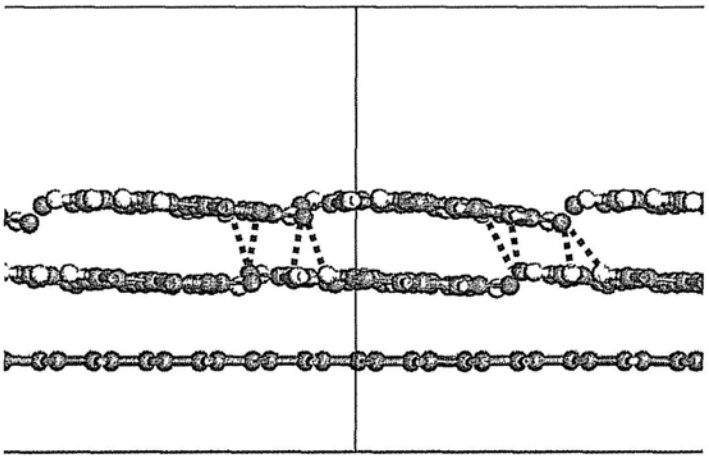

(g)

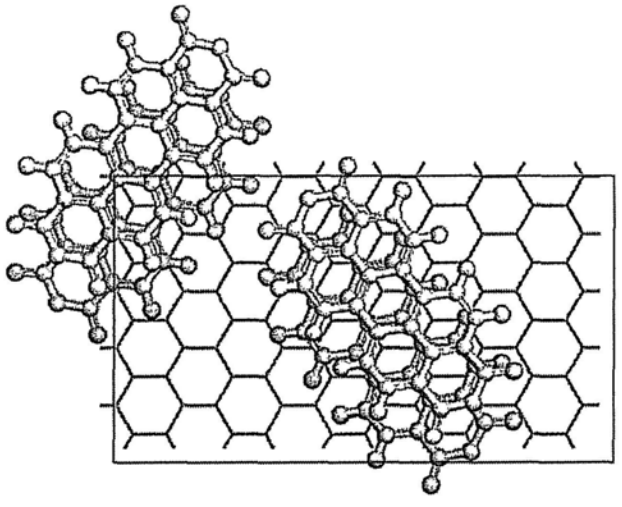

β modification

(h)

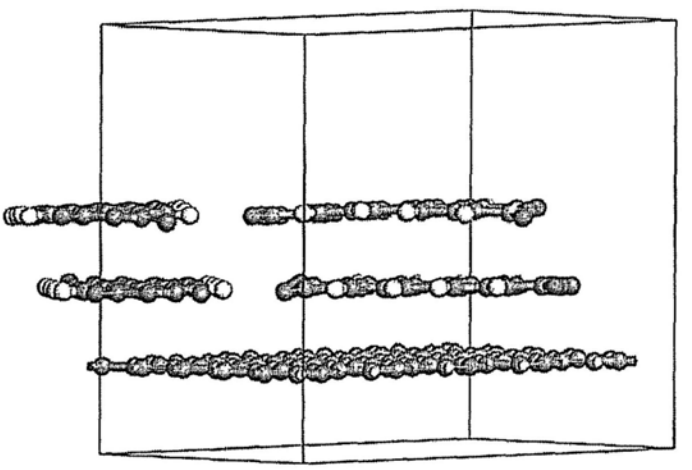

(i)

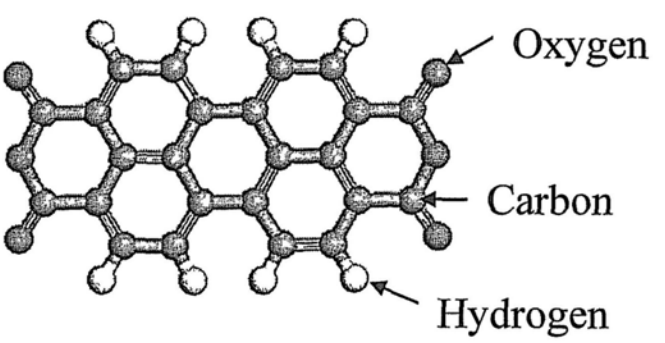

Figure 5.5 Optimized configurations of PTCDA bilayer on graphene with four typical configurations: (a) and (b) type I; (c) and (d) type II; (e) and (f) α modification; (g) and (h) β modification. (i) structure of PTCDA molecule. In top view, top molecule is brown and bottom is green. In side view, oxygen atoms are red, hydrogen atoms are white, and carbon atoms are gray. Blue dashed lines are inter-layer hydrogen bonds.

The adsorption energy of the second layer averaged to each molecule is calculated by:

$$E_{ad}{}^{2} = -(E - E^{1} - E_{monolayer})/2 \qquad (4)$$

where E is the total energy of the single layer graphene with bilayer PTCDA adsorption; $E_{monolayer}$ is the total energy of monolayer; E^{1} is the total energy of

single-layer graphene with monolayer adsorption.

Subsequently, the adsorption energy of the third layer averaged to each molecule is calculated by:

$$E_{ad}{}^{3} = -(E - E^{2} - E_{monolayer})/2 \qquad (5)$$

where E is the total energy of the single layer graphene with trilayer PTCDA adsorption; $E_{monolayer}$ is the total energy of monolayer; E^{2} is the total energy of single-layer graphene with bilayer PTCDA adsorption.

For type I configuration, as shown in Figures 5.5(a) and (b), the relative shift of the second layer to the first layer is 1.62 Å, and the shift direction is neither along *a* or *b*, with an angle around –45° to *a*. In this case, the stacking of right molecule in the top layer to the bottom layer is similar to the Bernal stacking of graphite π electrons, and the stacking of the left molecule in the top layer to the bottom layer slightly differs from the Bernal stacking. Hence it is expected this configuration may have a larger adsorption energy contributed from π electron interaction of the two PTCDA monolayers. The adsorption energy contributed from the second layer, averaged to each molecule ($E_{ad}{}^{2}$) is 0.65 eV. The adsorbed two layer planes are titled around 3° relative to the graphene plane. $E_{ad}{}^{2}$ is smaller than that of the single monolayer-substrate absorption energy $E_{ad}{}^{1}$=0.83 eV, and the intermolecular lateral interaction energy E_{HB} = 0.78 eV, so the adsorption of the top monolayer has a minor effect on the bottom monolayer.

Type II configuration is shown in Figures 5.5(c) and (d). The adsorption energy of the second monolayer PTCDA is $E_{ad}{}^{2}$= 0.29 eV. The top monolayer has no lateral shift relative to the bottom monolayer. The two layer planes are nearly parallel to the graphene plane, with an angle around 1° relative to the graphene one. $E_{ad}{}^{2}$ is fairly smaller than $E_{ad}{}^{1}$ and E_{HB}, so the adsorption of the top monolayer has negligible effect on the bottom monolayer.

The optimized structure of type III configuration (*α* modification) is shown in Figures 5.5(e) and (f). The second monolayer has a shift of 2.12 Å relative to the first layer along *a* direction. The PTCDA adsorption energy contributed from the second

layer is $E_{ad}{}^{2,\alpha} = 0.75$ eV. $E_{ad}{}^{2,\alpha}$ is slightly larger than E_{HB} and is closed to $E_{ad}{}^{1,\alpha}$. Therefore the adsorption of the top layer can affect the bottom layer. The top and bottom layer planes are slanted at 10° and 8° angles, respectively relative to the graphene plane. There are 8 interlayer hydrogen bonds between the top and bottom layers, which can contribute to the adsorption energy and ensure the adsorption configuration more stable. We also consider type III configuration, with the top layer having a shift of 1.85 and 2.41 Å relative to the first layer along a direction, respectively. It is found that their adsorption energy is smaller than those in type III configuration with 2.12 Å shift. The top PTCDA layer has totally 8 hydrogen bonds with the bottom layer, which could drive the PTCDA phase transition from surface phase to bulk-like phase. Each PTCDA of the bottom layer gains $0.15e$ from graphene, and that of the top layer attains $0.06e$ from graphene.

The optimized structure of type IV configuration (β modification) is depicted in Figures 5.5(g) and (h). The second layer has a shift of 2.00 Å relative to the first layer along b direction. Its adsorption energy is $E_{ad}{}^{2,\beta} = 0.73$ eV. Type IV configurations, with a shift of 1.76 and 2.32 Å have also been calculated, and their adsorption energy are smaller than those with 2.00 Å shift. Therefore it is anticipated that β modification with 2.00 Å shift is thermodynamically stable.

So it is concluded that for PTCDA bilayer growth on graphene, α modification is more thermodynamically stable than β modification, due to $E_{ad}{}^{2,\alpha}$ larger than $E_{ad}{}^{2,\beta}$. MM calculation also confirm the α modification is more stable than β modification with energy preference of 50 meV. The comparison for out-plane adsorption energy of different PTDA layers is shown in Figure 5.6 For α modification mode, the $E_{ad}{}^{2,\alpha}$ is smaller than $E_{ad}{}^{1,\alpha}$ by 0.08eV, so the growth of full first layer is preferable to incomplete first layer with partial second layer on top thermodynamically. Similarly, this comparison is applicable for β modification mode. For initial growth stage of PTCDA on graphene, the PTCDA could form a completer first monolayer on graphene substrate, and this is in agreement with experimental findings.[13, 14]

(a)

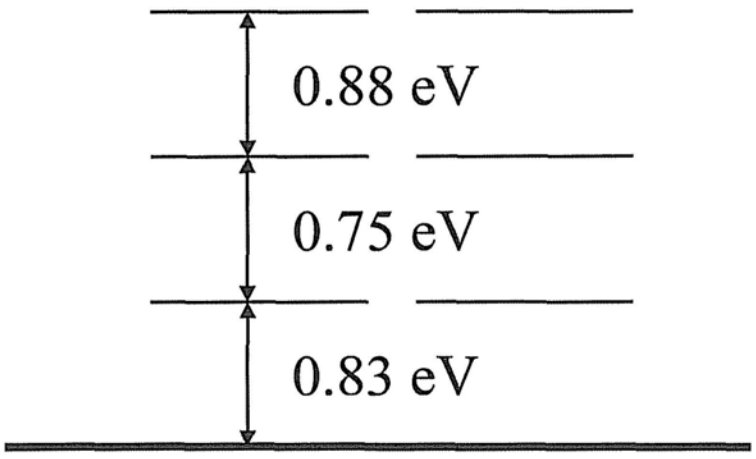

(b)

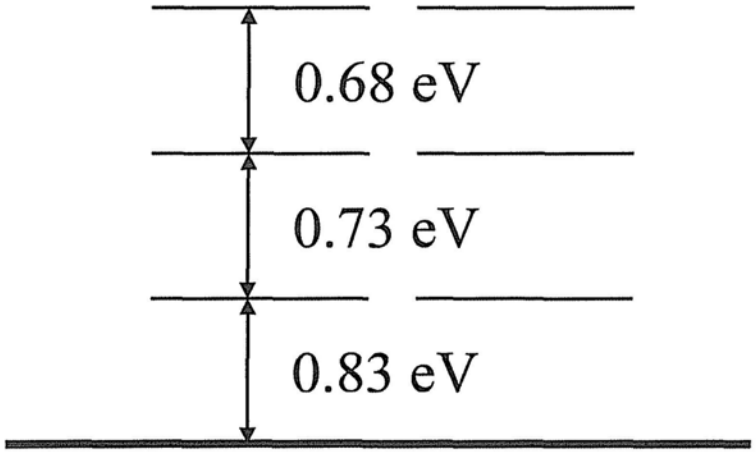

Figure 5.6 Comparison of out-plane adsorption energy for three layers by DFT (a) *α modification*; and (b) *β modification*. Thick line stands for graphene substrate and each two in-plane thin lines stand for PTCDA monolayer.

5. 3.5 Growth of PTCDA Trilayer on Graphene

Subsequently, PTCDA trilayer growth on graphene with both α and β

modifications are investigated, with the optimized structures shown in Figure 5.7

(a)

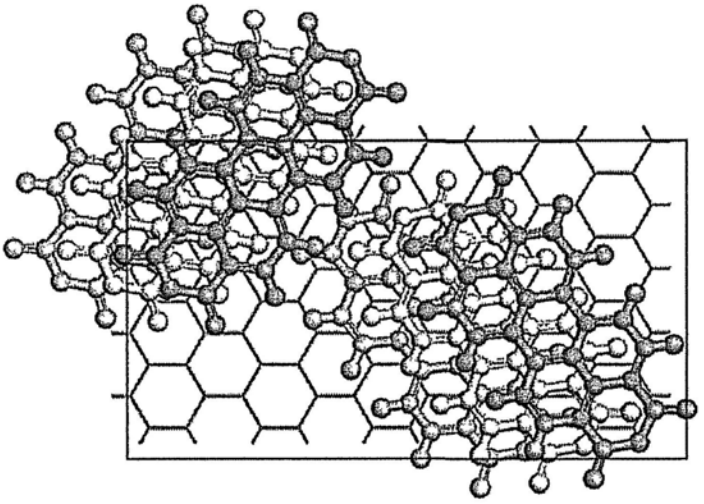

α modification

(b)

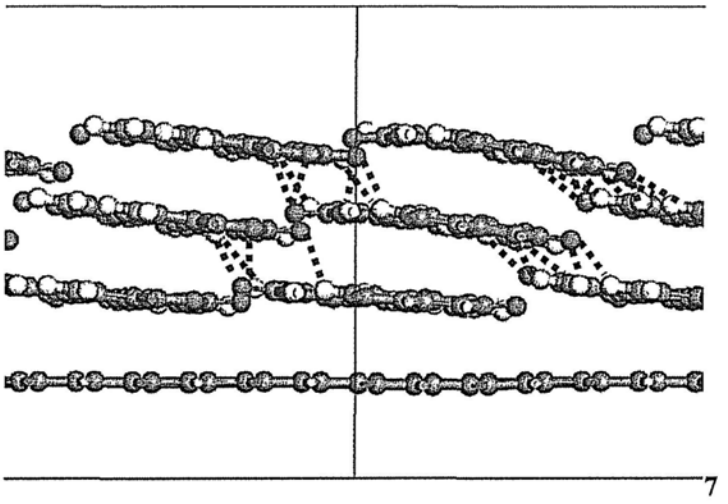

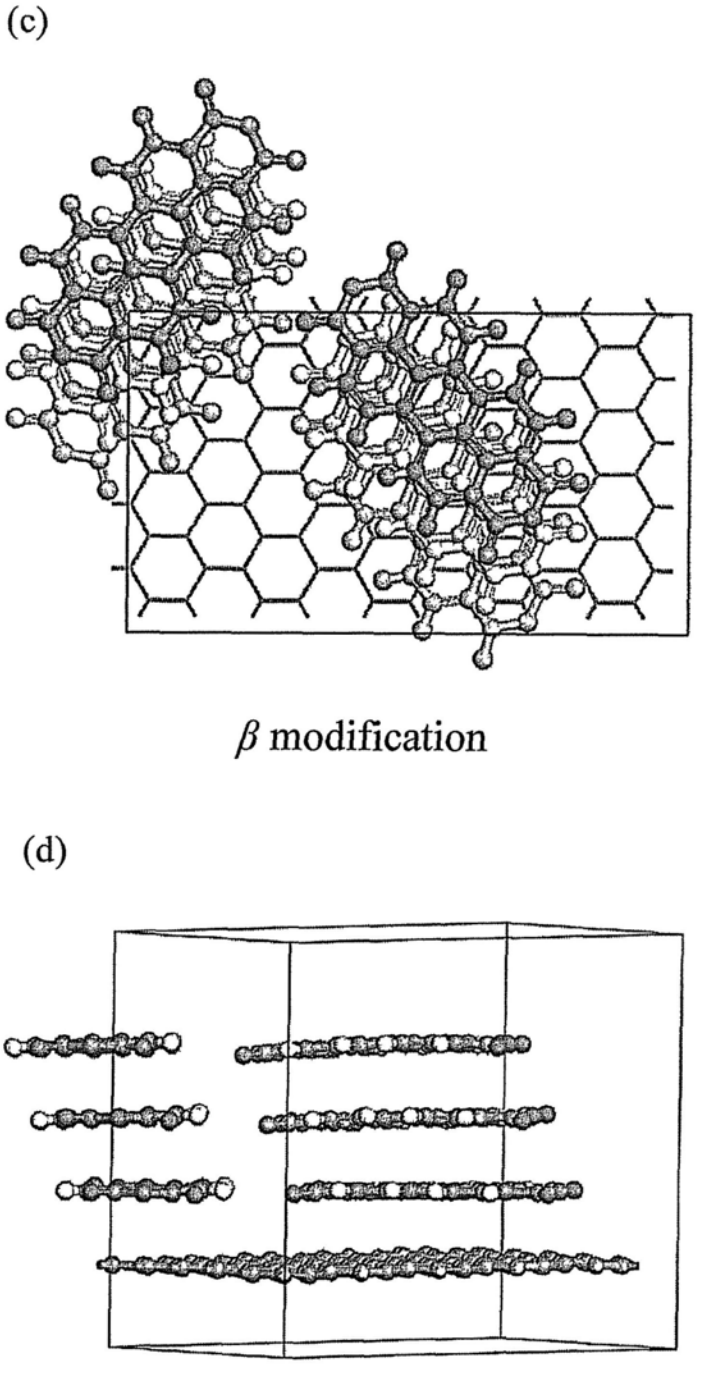

Figure 5.7 Optimized configurations of PTCDA trilayer on graphene: (a) and (b) *α modification*; (c) and (d) *β modification*. For top view, top molecule is pink, middle is brown, and bottom is green. Blue dashed lines are inter-layer hydrogen bonds.

For α modification of 2.15 Å, the adsorption energy contributed by the third layer, averaged to each molecule ($E_{ad}^{3,\alpha}$) is 0.88 eV. Obviously, $E_{ad}^{3,\alpha}$ is larger than both $E_{ad}^{2,\alpha}$ and E_{HB}. Hence it is expected that the adsorption of the third PTCDA monolayer

could introduce structural conformation in the bottom bilayer. The top, middle and bottom layer planes have tilted angles around 15°, 13° and 10°, relative to the graphene plane, respectively. So PTCDA molecules with high coverage tend to incline relative to graphene substrate, which eventually improves the lateral transport properties and is useful for organic transistors. The top layer has 14 hydrogen bonds with the middle layer in each super cell, which contributes to the adsorption energy and enlarges the inclination angles of the molecular planes relative to the substrate. Besides, the dense intermolecular hydrogen bonds could help to drive the phase transition from surface phase to bulk-like phase to release the free energy. Each bottom PTCDA gains $0.15e$ from graphene, while the middle and top attains 0.02 and $0.01e$ respectively from graphene, and the total charge transfer of $0.36e$ is less than that of $0.42e$ in bilayer. The charge difference distribution is shown in Figure 5.8. Both gained charge of top and middle MLs are less than that of bottom ML. The gained charge of top ML is smaller than that of middle ML. Therefore it is awaited that the total charge transfer saturates in the bilayer configuration.

For α modification, 1.90 and 2.38 Å shifts are also calculated, with adsorption energies smaller than that with 2.15 Å shift. Based on the analysis of out-plane adsorption energy as shown in Figure 5.6 (a), $E_{\mathrm{ad}}{}^{3,\alpha}$ is larger than $E_{\mathrm{ad}}{}^{2,\alpha}$, so the growth of island on top of incomplete second layer is more stable than complete second layer thermodynamically. For α modification mode, PTCDA could not form a second complete monolayer on graphene, and the growth of PTCDA follows 3D island growth mode, when coverage is larger than 1 ML. So the growth of PTCDA on graphene follows SK mode (layer plus island).

(a)

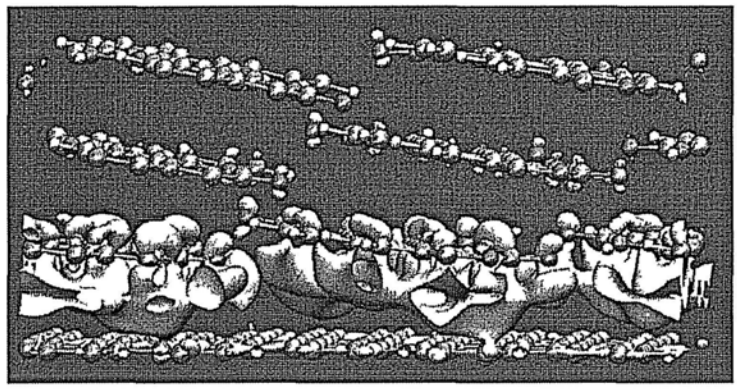

(b)

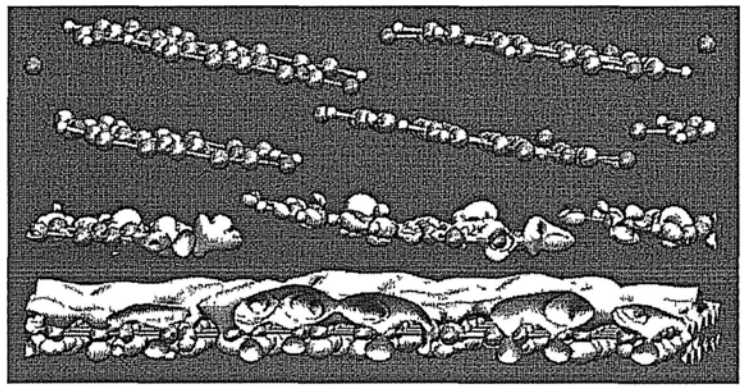

(c)

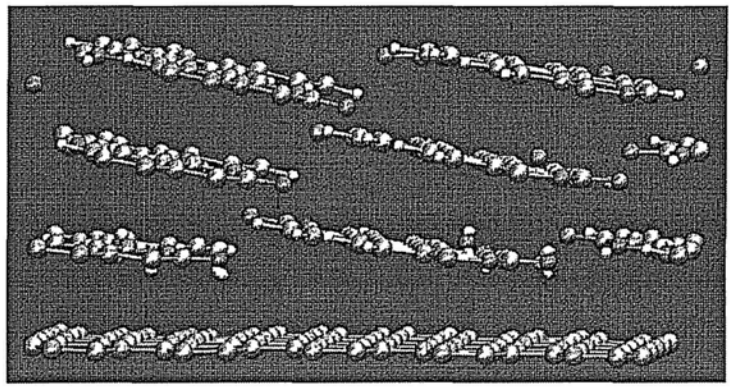

(d)

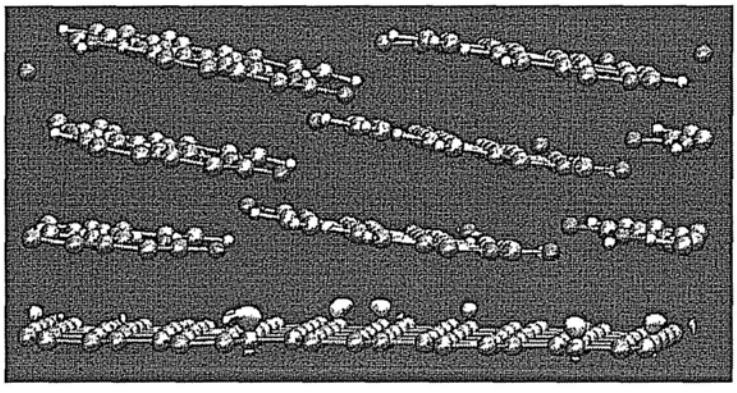

Figure 5.8 Isosurface of charge difference distribution at different densities: (a) 0.001e/ Å^3, (b) -0.001e/ Å^3, (c) 0.006e/ Å^3, and (d) -0.006e/ Å^3.

For trilayer with β modification growth, the adsorption energy of 1.96 Å shift is $E_{ad}{}^{3,\beta} = 0.68$ eV, which is larger than that of both 1.76 Å and 2.22 Å. The PTCDA molecular planes are tilted around 3° respective to graphene substrate. There exists no hydrogen bond among PTCDA monolayers. From the comparison of out-plane adsorption energy as shown in Figure 5.6(b), $E_{ad}{}^{3,\beta}$ is smaller than $E_{ad}{}^{2,\beta}$ by 0.05 eV, so complete second layer is more stable than partial third layer on top of incomplete second layer thermodynamically. For β modification growth, PTCDA could form a second complete layer on graphene.

Therefore, for PTCDA trilayer on graphene, α modification is more stable than β modification, due to energy preference of 0.20 eV as shown in Table 1. From MM calculation, the α modification is more stable than β modification due to energy preference of 0.29eV. The optimized structures of PTCDA trilayer on graphene by MM is shown in Figure 5.9. For α modification, there is a surface to bulk-like phase transition, while for β modification, there is no such structural phase transition.

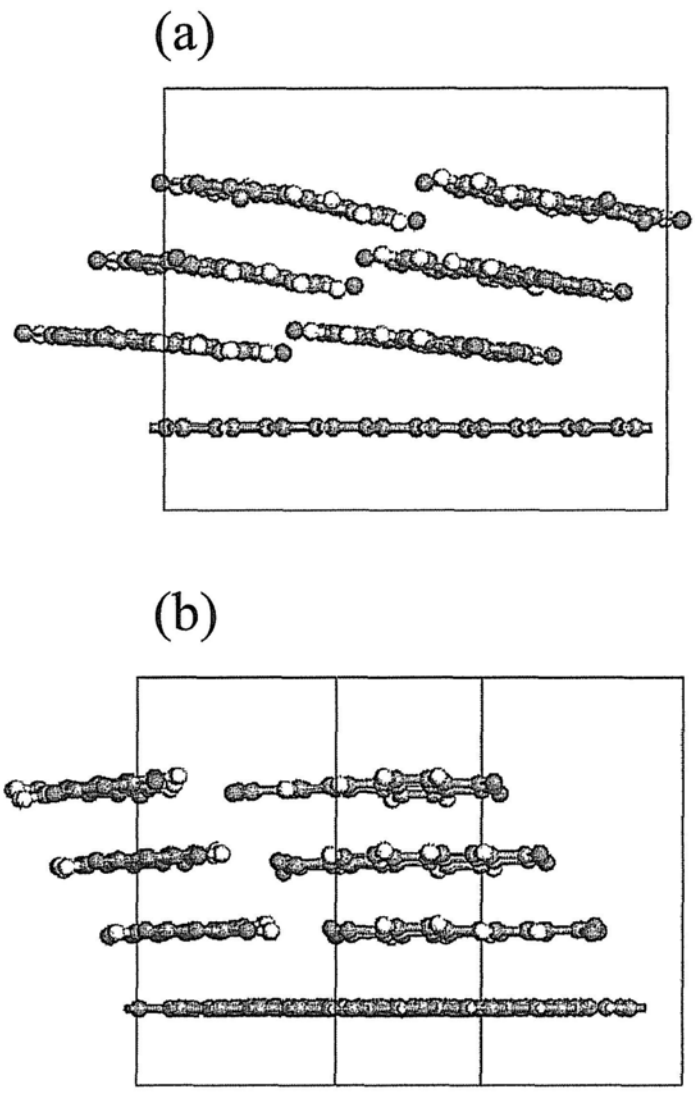

Figure 5. 9 Side views of optimized structures for PTCDA trilayer on graphene by MM: (a) α modification; (b) β modification.

5. 4 Conclusion

PTCDA ultrathin films assembly behaviors on single-layer graphene are investigated by DFT based *ab initio* calculation techniques. PTCDA monolayers are disposed in a stable herringbone configuration on graphene sheet. Typical defects in graphene substate have very limited perturbation effects on structural planarity and continuity of PTCDA monolayer. The growth of PTCDA on graphene follows the SK mode. A distinctive phase transition from surface phase to bulk-like phase is

discovered to occur when the coverage reaches 2~3 MLs. In particular, at 3 MLs coverage, the molecular planes of PTCDA have a larger inclined angle to graphene substrate, with the top monolayer at 15°, which is highly anticipated to affect the lateral charge transport characteristics, and be useful in organic transistors. Meanwhile, PTCDA molecules gain electrons from graphene, which clearly demonstrate *p* type doping attributes. For bilayer PTCDA coverage, the total charge transfer between them per PTCDA molecule is 0.42*e*, which is 0.1*e* and 0.06*e* larger than that in 1 and 3 ML coverage, respectively. Moreover, it introduces a direct band gap to graphene sheet. These results are in accordance with experiment and reveal a progressive way of PTCDA growth on graphene. This approach presents a potential to explore self-assembly organic layers on graphene and paves the way for design of graphene-based electronics.

References

(1) Novoselov, K. S.; Geim, A. K.; Morozov, S. V.; Jiang, D.; Zhang, Y.; Dubonos, S. V.; Grigorieva, I. V.; Firsov, A. A. *Science* **2004**, 306, 666-669.

(2) Castro Neto, A. H.; Guinea, F.; Peres,N. M. R.; Novoselov, K. S.; Geim, A. K. *Rev. Mod. Phys.* **2009**, 81, 109-162.

(3) Morozov, S. V.; Novoselov, K. S; Katsnelson, M. I.; Schedin, F.; Elias, D. C.; Jaszczak, J. A.; Geim, A. K. *Phys. Rev. Lett.* **2008**, 100, 016602-016605.

(4) Kudin, K. N.; Ozbas, B.; Schniepp, H. C. ; Prud'homme, R..; Aksay, I. A.; and Car, R. *Nano Lett.* **2008**, 8, 36-41.

(5) Park, C.-H.; Giustino,F.; Spataru, C. D.; Cohen, M. L.; and Louie, S. G. *Nano Lett.* **2009**, 9, 4234-4239.

(6) Pan, Y. ; Zhang, H. G.; Shi, D. X.; Sun, J. T.; Du, S. X.; Liu, F.; Gao, H. J. *Adv. Mater.* **2009**, 21, 2777-2780.

(7) Xiang, H.; Kan, E. J.; Wei, S. H.; Whangbo M. H.; and Yang, J. L. *Nano Lett.* **2009**, 9, 4025-4030.

(8) Huang, B.; Liu, M.; Su, N. H.; Wu, J.; Duan, W.H.; Gu, B. L.; and Liu, F. *Phys. Rev. Lett.* **2008**, 100, 016602-016605.

(9) Ohta, T.; Bostwick, A.; Seyller, T.; Horn, K.; Rotenberg, E. *Science* **2006**, 313, 951-954.

(10) Gierz, I.; Riedl, C.; Starke, U.; Ast, C. R.; Kern, K. *Nano Lett.* **2008**, 8, 4603-4607.

(11) Kessler, B. M.; Girit, C. O¨.; Zettl, A.; and Bouchiat, V.; *Phys. Rev. Lett.* **2010**, 104, 047001-047004.

(12) Dong, X. C.; Shi, Y. M.; Zhao, Y.; Chen, D. M.; Ye, J.; Yao, Y. G.; Gao, F.; Ni, Z. H.; Yu, T.; Shen, Z. X.; Huang, Y. X.; Chen, P.; and Li L. J. *Phys. Rev. Lett.* **2009**, 102, 135501-135504.

(13) Wang, Q. H.; and Hersam, M. C. *Nat. Chem.* **2009**, 1, 206-211.

(14) Huang, H.; Chen, S.; Gao, X. Y.; Chen, W.; and Wee, A. T. S. *Acs Nano* **2009**, 3,

3431-3436.

(15) Temirov, R.; Soubatch, S.; Luican, A.; and Tautz, F. S.; *Nature* **2006**, 444, 350-353.

(16) Du, S. X.; Gao, H. J.; Seidel, C.; Tsetseris, L.; Ji, W.; Kopf, H.; Chi, L. F.; Fuchs, H.; Pennycook, S. J.; and Pantelides, S. T.; *Phys. Rev. Lett.* **2006**, 97, 156105-156108.

(17) Burke, S. A.; Ji, W.; Mativetsky, J. M.; Topple, J. M.; Fostner, S.; Gao, H.-J.; Guo, H.; and Gru¨tter1, P. *Phys. Rev. Lett.* **2008**, 100, 186104-186107.

(18) Jalkanen,J.P.; and Zerbetto, F. *J. Phys. Chem. B* **2006**, 110, 5595-5601.

(19) Swarbrick, J. C.; Rogers, B. L.; Champness, N. R.; and Beton, P. H. *J. Phys. Chem. B* **2006**, 110, 6110-6114.

(20) Ma, J.; Rogers, B. L.; Humphry, M. J.; Ring, D. J.; Goretzki, G.; Champness, N. R.; and Beton, P. H. *J. Phys. Chem. B* **2006**, 110, 12207-12210.

(21) Yang, A.; Shipman, S.T.; Garrett-Roe, S.; Johns, J.; Strader, M.; Szymanski, P.; Muller, E.; and Harris, C. *J. Phys. Chem. C* **2008**, 112, 2506-2513.

(22) Eremtchenko, M.; Schaefer, J. A.; and Tautz, F. S. *Nature* **2003**, 9, 602-605.

(23) Kendrick, C.and Kahn, A. *J. Cryst. Growth.* **1997**, 181, 181-192.

(24) Möbus, M.; Karl, N.; and Kobayashi, T. *J. Cryst. Growth.* **1992**, 116, 495-504.

(25) Wang, X. R.; Tabakman, S. M.; and Dai, H. J. *J. Am. Chem. Soc.* **2008**, 130, 8152-8153.

(26) Kresse, G.; Furthmu¨ller J. *Comput. Mater. Sci.* **1996**, 6, 15-50.

(27) Kresse, G.; Joubert, D.; *Phys. Rev. B* **1999**, 59, 1758-1775.

(28) Rochefort, A.; and Wuest, J. D., *Langmuir* **2009**, 25, 210-215.

(29) Li, M. M.; Zhang, J.; Li, F. J.; Zhu, F. X.; Zhang, M.; and Zhao, X. F. *Phys. Status Solidi C* **2009**, 6, s90-s93

(30) Shi, D. X.; Ji, W.; Lin, X.; He, X. B.; Lian, J. C.; Gao, L. ; Cai, J. M.; Lin, H.; Du, S. X.; Lin, F.; Seidel, C.; Chi, L. F.; Hofer, W. A.; Fuchs, H.; and Gao, H.-J. *Phys. Rev. Lett.* **2006**, *96*, 226101-226104.

(31) Ulbricht,H.; Moos, G.; and Hertel, T. *Phys. Rev. Lett.* **2003**, *90*, 095501-095504.

(32) Feng, C.; Lin, C. S.;Fan, W.; Zhang, R. Q.; and Van Hove, M. A. *J. Chem. Phys.* **2009**, *131*, 194702-194709.

(33) Chakarova-Ka¨ck, S.D.; Schro¨der, E.; Lundqvist, B. I.; and Langreth, D. C. *Phys. Rev. Lett.* **2006**, *96*, 146107-146110.

(34) Kendrick, C.; Kahn, A.; and Forrest, S. R. *Appl. Surf. Sci.* **1996**, *104/105*, 586-594.

(35) Hoshino, A.; Isoda, S.; Kurata, H.; and Kobayashi, T. *J. Appl. Phys.* **1994**, 76, 4113-4120.

(36) Jiang, L.; and Lai, L. H. *J. Biol. Chem.* **2002**, 277, 37732-37740.

(37) Scheiner, S.; Kar, T.; and Gu, Y. L. *J. Biol. Chem.* **2001**, 276, 9832-9837.

(38) Desiraju, G. R. *Acc. Chem. Res.* **1996**, 29, 441-449.

(39) Musolino, V.; Selloni, A.; and Car, R. *Phys. Rev. Lett.* **1999**, 83, 3242-3245.

Chapter 6 Covalent Modification Induced Novel Magnetic Properties in Graphene Sheet

6. 1 Introduction

Graphene sheet has drawn intense research interest in recent years, since it was first synthesized in 2004.[1] Pristine graphene sheet is a zero gap semiconductor and non-spinpolazied, which limits its applications. The problems of current diluted magnetic semiconductor (DMS) are merits of carriers and ferromagnetism could not coexist well, and Curie temperature (T_c) is normally below room temperature.[2,5] Previous investigations have reported numerous methods to introduce magnetism into graphene.[6-10] The magnetic properties of graphene could be tuned by transitional metal interaction with single and double vacancies in graphene via orbital hybridization as shown in Figures 6.1 and 6.2.[6] Self-assembled metal atom chains on GNR were studied, and light alkali and alkaline-earth metal elements could introduce magnetism into graphene as shown in Figure 6.3.[7] Hydrogenation of graphene is another method to introduce magnetism into graphene. [8] Graphene defects were investigated and found to be another source for spin polarization.[9] Experimental results have verified defects in graphene could introduce above room temperature ferromagnetism in graphene sheet.[10]

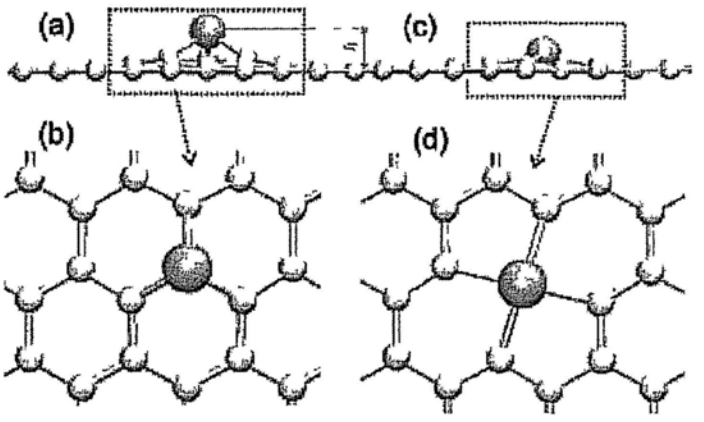

Figure 6.1 Typical atomic configurations of TM atoms adsorbed on single and double vacancies in a graphene sheet. Metal atom on a single vacancy: Side view (a), top view (b). Note that the metal atom is above the surface, with an elevation h of up to 2 A°. Metal atom on a double vacancy: Side view (c) and top view (d). The grey balls are metal atoms, the yellow balls carbon atoms. The structure of a V@DV complex is shown in the inset in Figure2. Taken from Ref. 6.

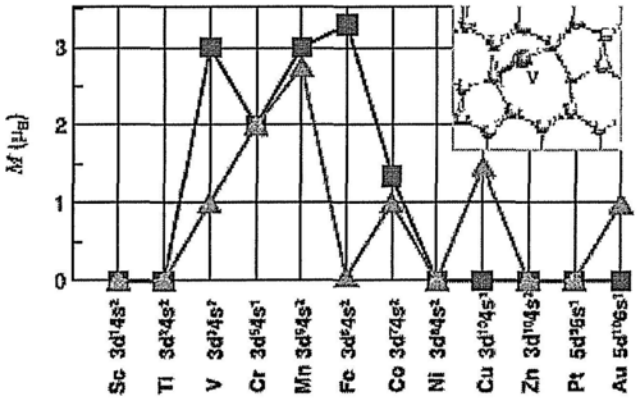

Figure 6.2 Magnetic moments (M) of the graphene sheet with TM atoms adsorbed on SVs and DVs (red and blue curves, respectively). The inset shows the configuration for V atom on DV which is different from those for all other atoms. The lines guide the eye. Taken from Ref. 7.

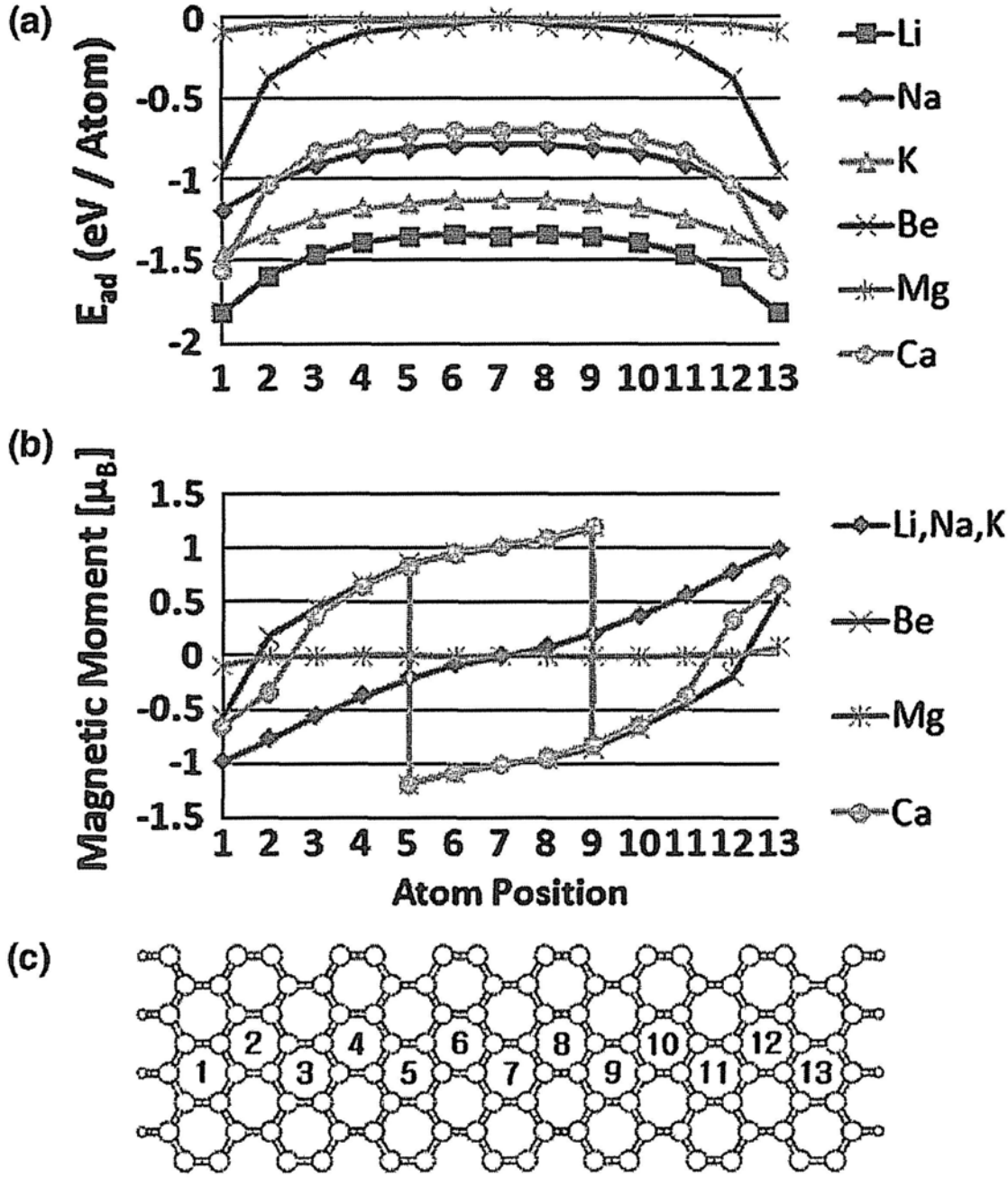

Figure 6.3 (a) Calculated adsorption energy of the metal atoms on a ZGNR along the lateral direction, and (b) calculated magnetic moment of the metal-adsorbed ZGNR per unit cell shown in (c).

In this chapter, we present a chemical modification route to obtain above room temperature ferromagnetic coupling graphene sheet, meanwhile with an abundance of hole carriers around $6.1\times10^{13}/cm^2$. Aryl groups were frequently used to functionalize graphene sheet in experiments. The transport properties of epitaxial graphene (EG) on

SiC substrate could be tuned from near-metallic to semiconducting characteristics by aryl group modification.[11] The aryl group functionalized graphene nanosheets disperse readily in polar aprotic solvents, allowing alternative avenues for simple incorporation into different polymer matrices.[12, 13] However, the exact interaction mechanism between aryl groups and graphene is not clear. Here we study the interaction mechanism between aryl groups and graphene, using methoxyphenyl, nitrophenyl to reveal the covalent modification of graphene, which induces the high T_c ferromagnetism.

6. 2 Calculation Methods

We use state of the art first principles technique to study the magnetic properties of methoxyphenyl and nitrophenyl groups modified graphene sheet. The calculations are carefully performed within Vienna ab initio simulation package (VASP).[14] The electron-ion interaction is described by PAW method.[15] The electron exchange and correlation is modeled by generalized gradient approximation (GGA) of Perdew–Burke–Ernzerhof (PBE) form.[16] 29.40 Ry is used as the plane-wave basis set cutoff. Single-layer graphene with super cell size of $3\sqrt{3}\times5$ is used as substrate to simulate aryl group adsorption at single molecular level. This super cell could guarantee the lateral separation between molecules is larger than 10 Å and this coverage also corresponds to molecular concentration of $6.3\times10^{13}/cm^2$. Single-layer graphene with super cell size of $2\sqrt{3}\times4$ plus four molecules in each cell are used to simulate arly group adsorption at high coverage, which also corresponds to aryl group concentration $4.7\times10^{14}/cm^2$. All atoms of molecule and graphene are allowed to relax until residual forces in all direction are less than 20 meV/Å. A 1.8 nm vacuum layer is used to eliminate the longitudinal interactions between super cells. 4×4×1 and 6×4×1 Monkhorst-Pack k-point meshes are used for low and high coverage cases, respectively. For GNR calculation, a k-point sampling of 16 k points that are uniformly positioned along the 1D Brillouin zone is employed for GNRs with zigzag

(armchair) shaped edges. The lateral vacuum layer between GNRs edges is larger than 1.2 nm and the perpendicular vacuum layer is 1.8 nm.

6. 3 Results and Discussion

6.3.1 *p*-Type Ferromagnetism Induced by Methoxyphenyl Group Adsorption on Graphene

For single molecule adsorption, the optimized structure is shown in Figure 6.4. The adsorption energy is defined by the following equation:

$$E_{ad}{}^{0} = -(E - E_0 - E_{molecule}) \qquad (1)$$

where E is the total energy of the single layer graphene with the molecule; $E_{molecule}$ is the chemical potential of the molecule and E_0 is the total energy of pristine single layer graphene. The adsorption energy $E_{ad}{}^{0}$ is 0.87 eV/molecule and the C_M-C_G bond length is 1.59 Å, which is 0.16 Å larger than graphene *C*-*C* bond length 1.43 Å.

(a)

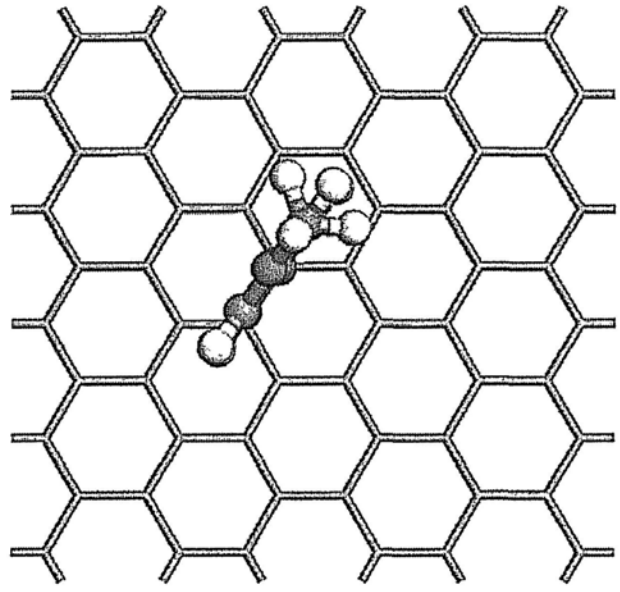

(b)

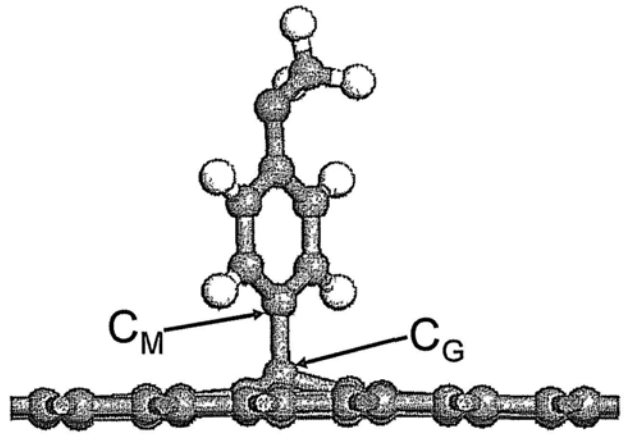

(c)

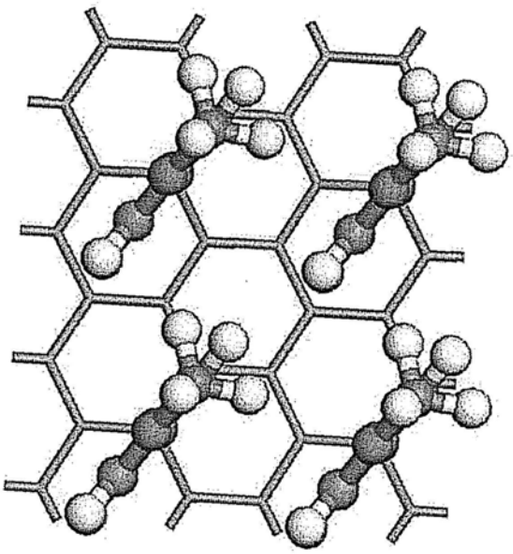

(d)

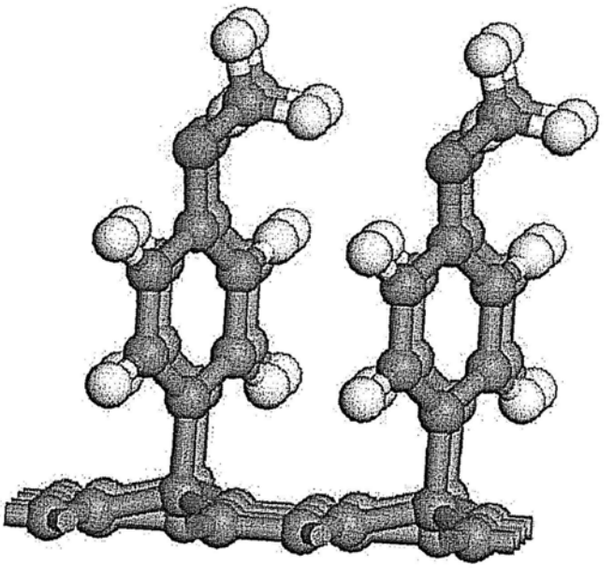

(e)

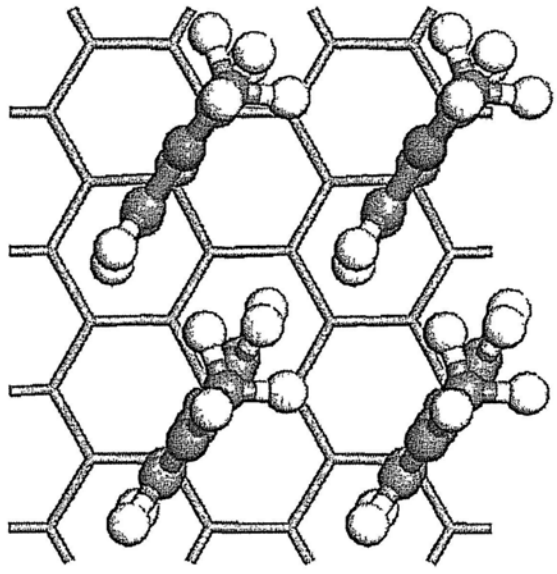

(f)

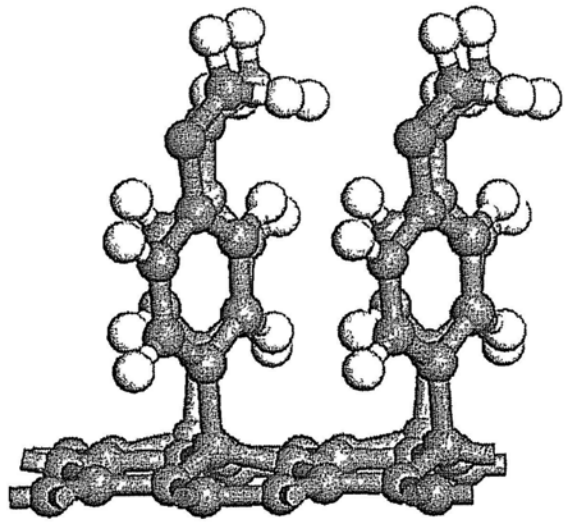

Figure 6.4 Optimized structure of methoxyphenyl group adsorption on graphene: (a) top view and (b) side view of low coverage, (c) top view and (d) side view of high coverage at configuration 1. (e) top view and (f) side view of high coverage at configuration 2. H atoms are white, C atoms are gray, and O atoms are red. This notation is used throughout this chapter.

The spin polarized projected density of states (SP-PDOS) is shown in Figure 6.5 (a). The SP-PDOS distribution for spin up and spin down is not symmetric, and the total magnetic moment is 0.91 Bohr magnetons (μ_B). There is an around 0.4 eV gap in graphene. As shown in Figure 6.5 (b), the net spin density is delocalized around aryl group, unlike $3d$ metallic magnet localized spin density distribution. The spin polarized $2p$ obtials are gained, which are useful in spintronics. Besides, the light element has a weak spin-orbital coupling energy, due to the coupling proportional to Z^4, where Z is the atomic index. If the C_G is set as in the B sublattice of graphene's two sublattices,[17] the atoms in A sublattice near C_G are spin-polarized as shown in Figure 6.5 (b). The C_M is spin-polarized with 0.07 μB, and C_G is non spin-polarized. The spin density around C_G obeys nearly triangular distribution, but not exact. Two atoms in L_S line neighboring C_G are spin polarized, each with 0.11 μ_B. The atom in L_F line closest to C_G is also spin polarized with 0.14 μ_B. The spin polarization along L_F is stronger than other lines.

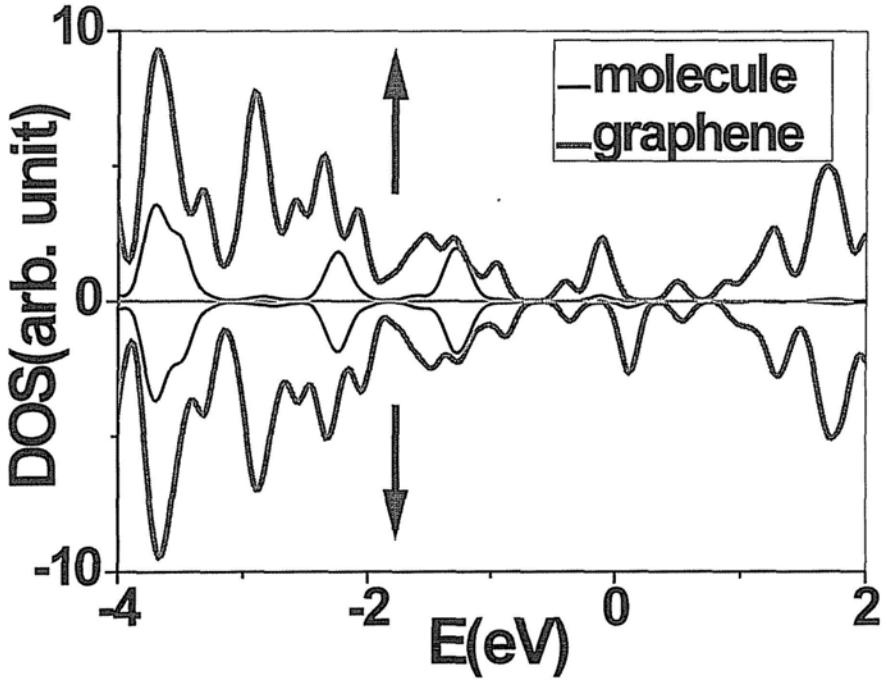

(a)

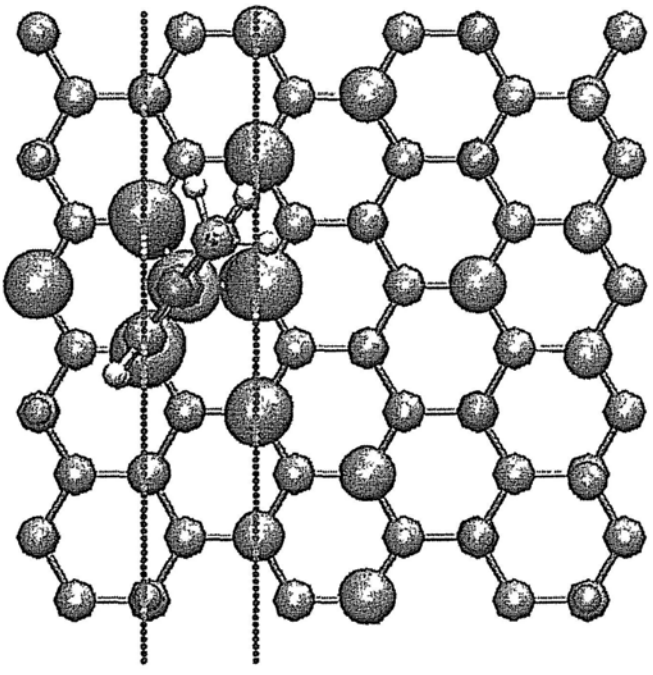

(b)

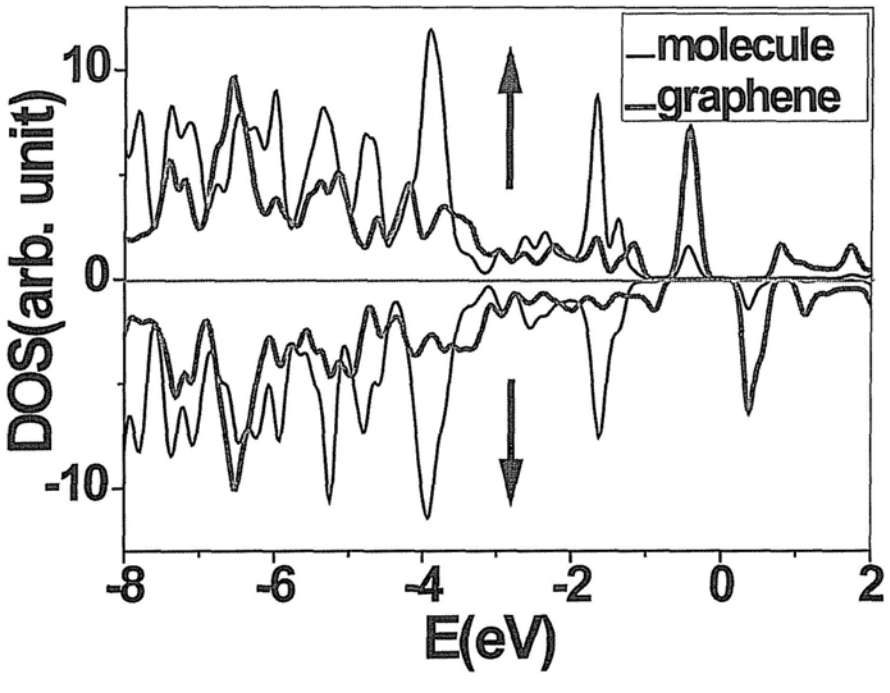

(c)

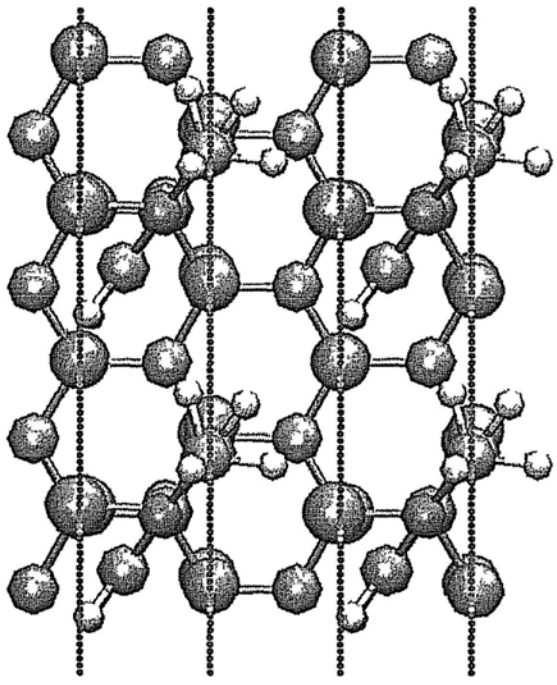

(d)

Figure 6.5 Electronic structures of methoxyphenyl group modified graphene: (a) SP-DOS and (b) 0.01Å^{-3} net spin density distribution of modificated graphene at low coverage (c) SP-DOS and (d) 0.01Å^{-3} net spin density distribution of modificated graphene at high coverage. For DOS figures, Fermi level is set to zero.

For high coverage adsorption of configuration 1, the optimized structure is shown in Figures 6.4 (c) and (d). The C_M-C_G bond length is 1.60 Å, which is nearly the same as that of single molecule adsorption. The adsorption energy E_{ad}^1 is 0.68 eV/molecule. Actually, this all aryl groups on the *B* group of Bernal stacking configuration is not the most stable configuration, with adsorption energy around 0.12 eV/molecule smaller than the most stable configuration 2 with aryl group adsorption at both *A* and *B* groups as shown in Figures 6.4 (e) and (f). This energy barrier is drastically smaller than kinetic process threshold energy barrier 0.8eV, [3, 18] so it is not large enough to prevent the proposed configuration 1 appearing in experiments. The configuration controlling and switching technique is an important step to exploit the ferromagnetism of aryl group modified graphene. The magnetism quenches at the most stable configuration. For configuration 1, each molecule gains 0.13*e* from

graphene by C_M-C_G bond. The PDOS is shown in Figure 6.5 (c), the spin up is the majority band, and spin down is the minority band. The molecule is weakly spin-polarized, and the spin polarization mainly localizes in graphene substrate. The spin density distribution is shown in Figure 6.5 (d), and there is totally 4 μ_B /cell. The C_M of molecule has 0.12 μ_B, which is around twice that of low coverage case. The C_G also has no magnetic moment. The total magnetic moment along L_F is 1.20 μ_B, and 0.56 μ_B along L_S line. The atom nearest to C_G, and which is also in the L_F, has the strongest spin polarization, with 0.41 μ_B.

The energy preference for ferromagnetic to anti-ferromagnetic state is defined as:

$$\Delta E = E_{AF} - E_F \qquad (2)$$

where E_{AF} is the total energy of anti-ferromagnetic state; E_F is the total energy of ferromagnetic state. The ΔE is 0.26 eV for 4 molecules, so for 3D calculation, the energy preference for ferromagnetic to anti-ferromagnetic state is $\Delta E/6$ per unit, which is 43 meV, with T_c of 496K estimated by the mean field approximation. The energy preference for anti-ferromagnetic state to nonmagnetic state is 46 meV. The GGA-PW91[19] results indicate that $\Delta E/6$ is 39 meV. The magnetic interaction for this delocalized ferromagnetism is via direct exchange, not RKKY, super exchange or double exchange.

From the band gap structure for clean graphene substrate shown in Figure 6.6(a), π and π^* bands intersect at the Dirac point (K). The non spin-polarized band structure for methoxyphenyl modified graphene at high coverage is shown in Figure 6.6 (b), and there is a 0.75 eV band gap opening at Γ. There are four nearly flat bands near Fermi level, corresponding to four molecules per cell. The spin-polarized band structure is shown in Figure 6.6 (c), and the band gaps for spin up and down are 1.06 eV and 1.20 eV, respectively at Γ. There are eight nearly flat bands near the Fermi level, four for spin up and other the other four for spin down, respectively. These eight nearly flat bands are actually the hybridized orbitals between molecule and graphene,

which can be understood by its corresponding PDOS in Figure 6.5 (d). The functionalized graphene shows a direct band gap, with both valence band maximum (VBM) and conduction band minimum (CBM) distributing at Γ not K of pristine graphene. So the monolayer coverage not only bring spin polarization into graphene sheet, but also introduce an around 1.1 eV band gap into graphene. This is in consistent with the experimental results that aryl group functionalization could reduce the conductivity of epitaxial graphene (EG) [8].

(a)

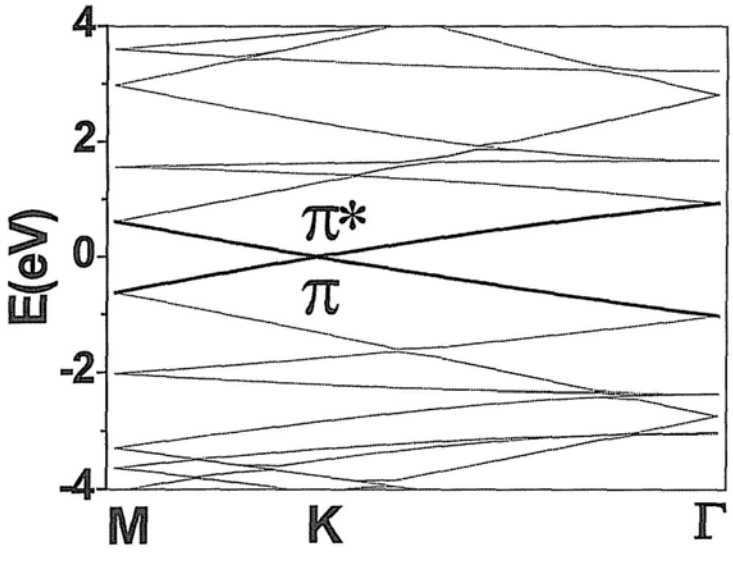

(b)

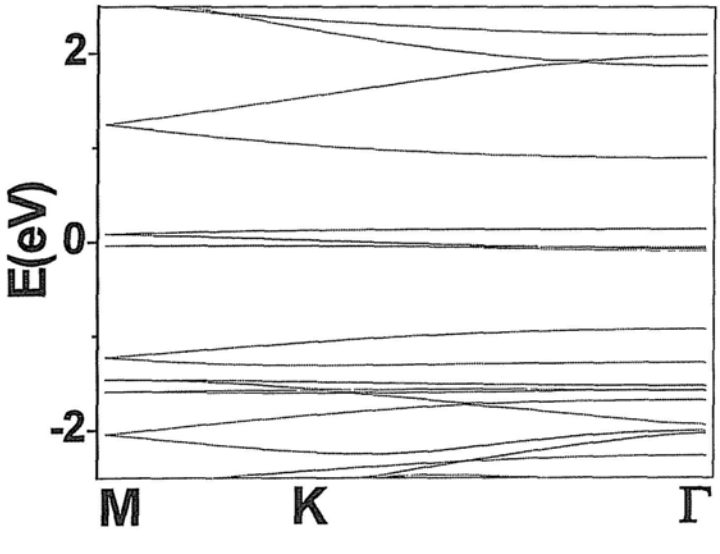

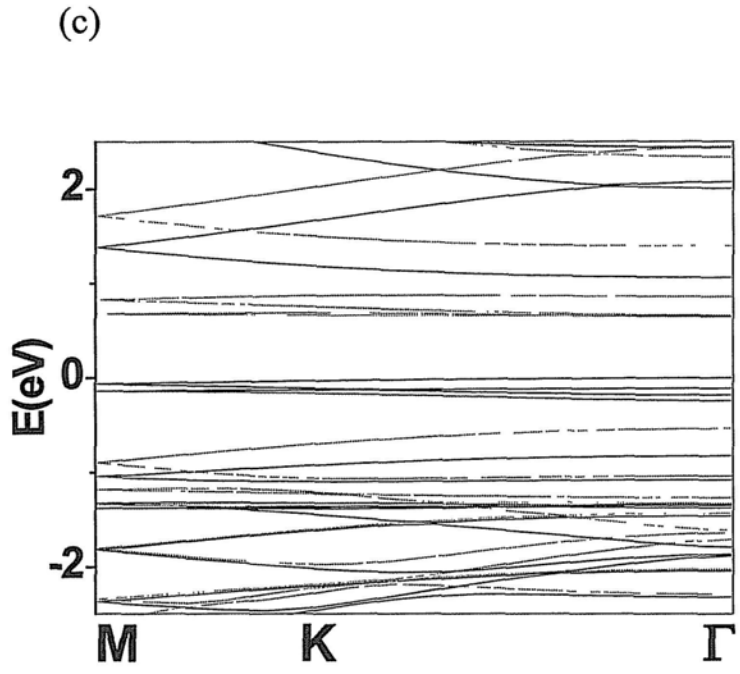

Figure 6.6 Band structure of pristine and methoxyphenyl group modified graphene at high coverage: (a) pristine graphene, (b) non-spin polarized band structure of the modified graphene, and (c) spin polarized band structure of the modified graphene. For spin polarized band structure, spin up is black and spin down is red. This notation is used throughout this chapter. The Fermi level is set to zero.

6.3.2 Ferromagnetism Introduced by Nitrophenyl Group Modification

To explore the functional group influence on the magnetic properties, nitrophenyl adsorption on graphene was also investigated. At high coverage of $4.7\times10^{14}/cm^2$, the nitrophenyl also induces spin polarization into graphene. The calculated structure for nitrophenyl on graphene is shown in Figures. 6.7 (a) and (b). The energy preference for ferromagnetic to anti-ferromagnetic state per unit $\Delta E/6$ is 40 meV, which is 3 meV smaller that of methoxyphenyl. The band gap is 1.12 eV and 1.15 eV for spin up and down bands respectively. Different from methoxyphenyl group, the spin up majority shows indirect band gap as shown in Figures. 6.7(c) and (d), with VBM around K and CBM at Γ. So the tail group of phenyl could have influence on the magnetic properties of graphene substrate.

(a)

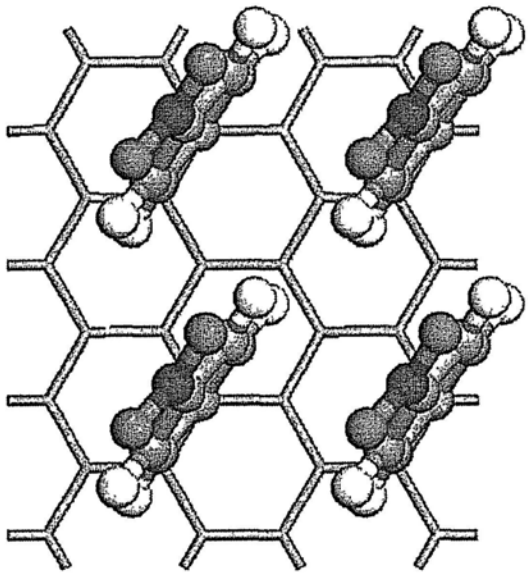

(b)

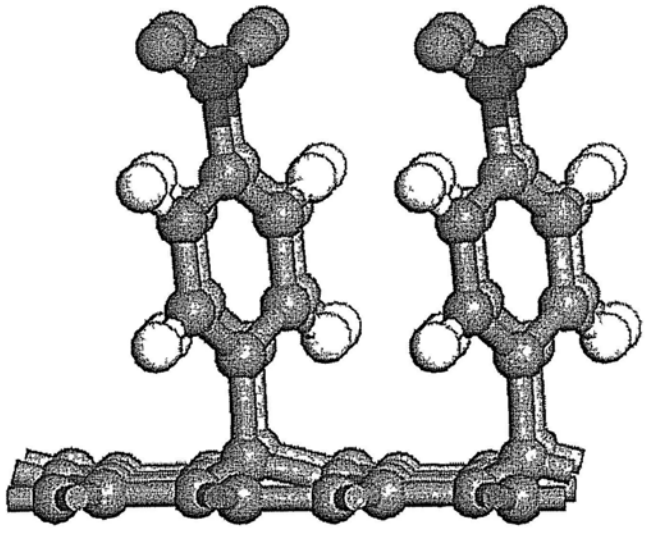

(c)

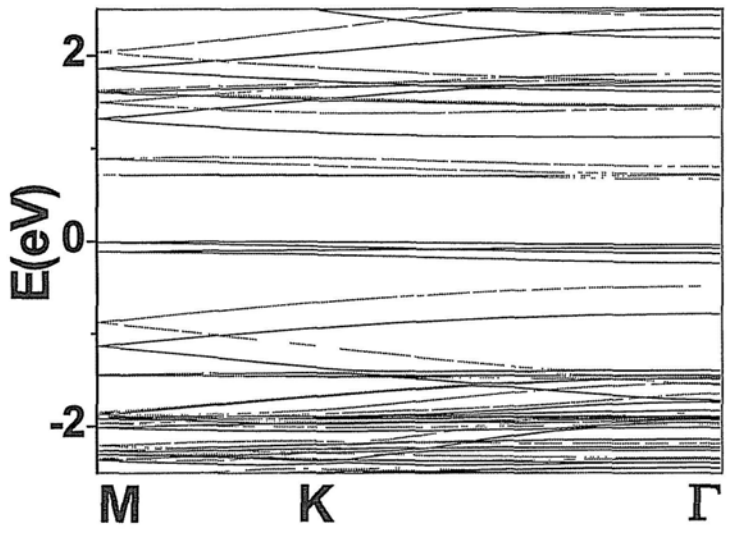

(d)

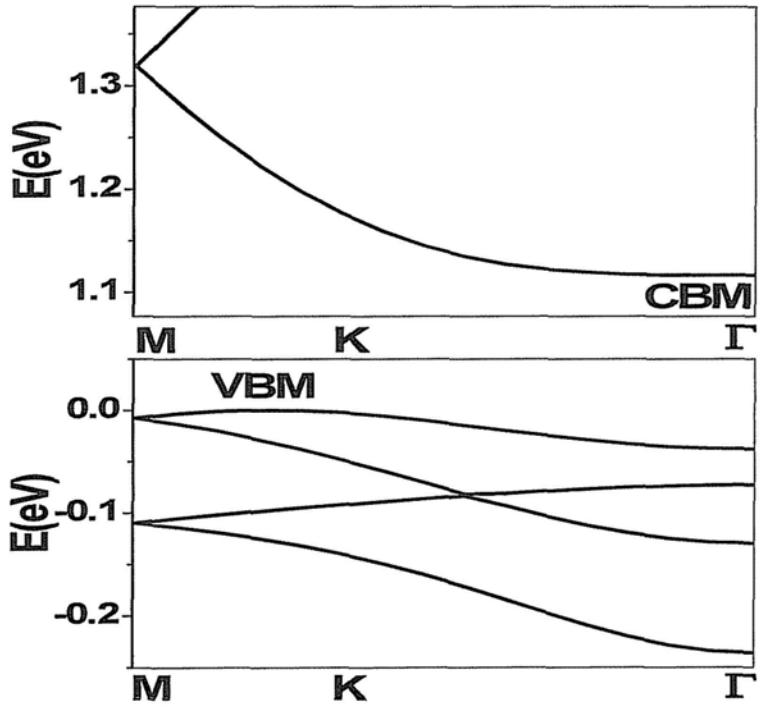

Figure 6.7 Optimized structure of nitrophenyl group modified graphene at high coverage. (a) top view, and (b) side view, and its corresponding spin polarized band structure: (c) with large

energy scale (d) zoom-in view of spin up around CBM and VBM. Nitrogen atoms are blue. For spin polarized band structure, the Fermi level is set to zero.

6.3.3 Magnetism on GNR by Methoxyphenyl Group Adsorption

The aryl group functionalization of zigzag GNR is also investigated, and the GNR scale is defined as Ref. 20. Zigzag nanoribbons were investigated and found to be spin polarized with magnetic moment enhancement. Zigzag nanoribbon with 6×10 scale is investigated by 5 adsorption configurations near edge as shown in Figure 6.8(a). The adsorption energy (E_{ad}^{0}) and magnetic moment (MM) for site dependence by GGA-PBE are shown in Table 6.1. The most stable configuration has the lowest MM, the second stable site 3 has around 2.9 μ_B, which is also the second largest MM. The site specific magnetic properties are confirmed by GGA-PW91, as shown in Table 6.2. The metastable site 4 has around 3.8 μ_B, and its PDOS is shown in Figure 6.8 (b). From the PDOS, it is found that the spin polarization mostly localizes in graphene nanoribbon and the molecule is weakly polarized. The near edge site dependent spin polarization is also found in zigzag 5×10 and 8×12 GNR. The maximum MM for zigzag 5×10 and 8×12 GNR can reach 3.0 and 4.0 μ_B, respectively. The adsorption energy also shows strong site specific characteristics. Why site 1 has the largest adsorption energy is possibly explained, as this configuration has the largest structural relaxation and distortion. The structural relaxation and distortion on other 4 inner sites are restricted by the perfect and stable conjugated π orbitals. Experiments have realized the fabrication of GNR with controlled edge structure.[21] It is anticipated that the site specific magnetic properties of GNR by aryl group functionalization would be exploited for spintronic applications.

(a)

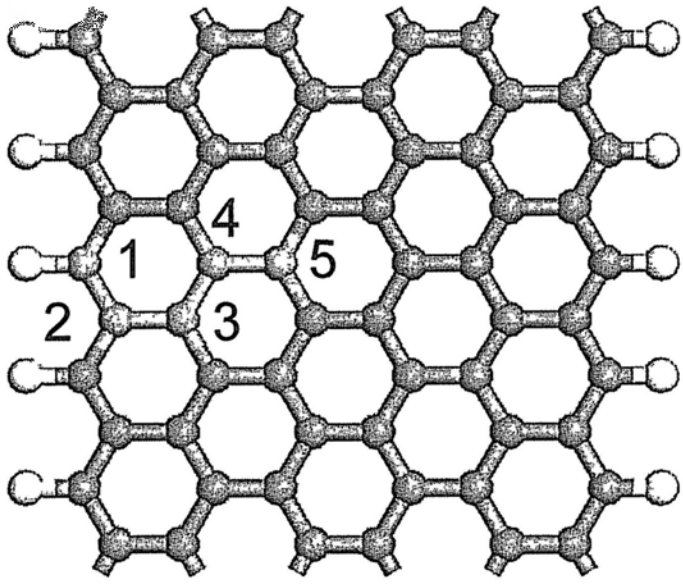

(b)

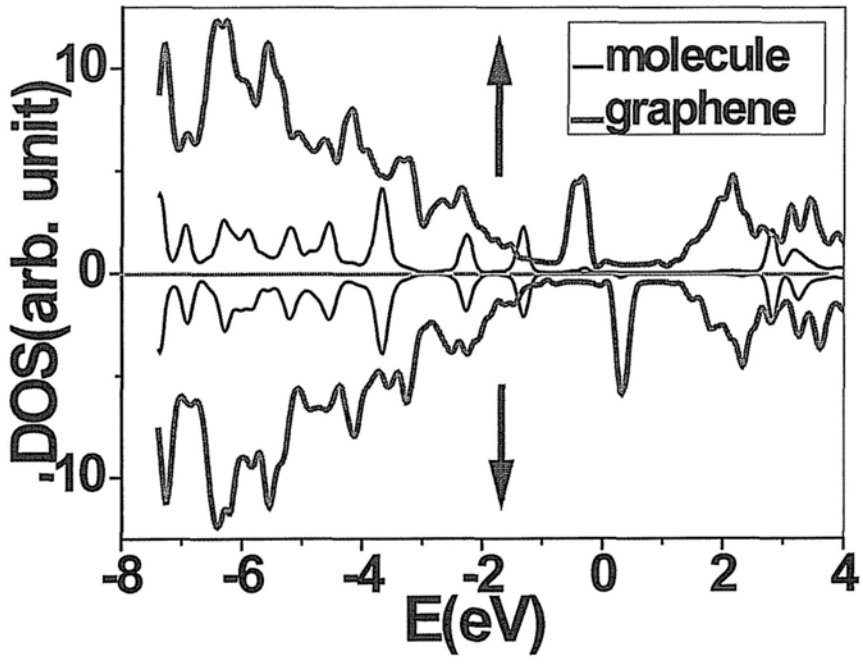

Figure 6.8 Five adsorption sites near edge (a), and SP-DOS of methoxyphenyl adsorption at site 4 (b).

Table 6. 1 Adsorption energy ($E_{ad}{}^{0}$) and magnetic moment (MM) of 5 sites near GNR edge by GGA-PBE.

	1	2	3	4	5
$E_{ad}{}^{0}$(eV)	3.02	0.55	1.47	0.78	1.13
MM(μ_B)	1.02	1.05	2.87	3.78	2.54

Table 6. 2 Adsorption energy ($E_{ad}{}^{0}$) and magnetic moment (MM) of 5 sites near GNR edge by GGA-PW91.

	1	2	3	4	5
$E_{ad}{}^{0}$(eV)	3.05	0.56	1.41	0.82	1.06
MM(μ_B)	1.08	1.03	2.76	3.83	2.52

6. 4 Conclusion

In summary, the delocalized *p*-type ferromagnetism in graphene sheet can be achieved by aryl group modification, with T_c above room temperature. Each aryl group will totally induce 1 μ_B into molecule/graphene system. The methoxyphenyl functionalized graphene may also induce a 1.1 eV direct band gap into graphene for both majority and minority bands, and nitrophenyl may induce 1.12 eV indirect band gap into majority band, and 1.15 eV direct band gap into minority band, respectively. Zigzag GNR shows strong site specific magnetic properties by aryl group adsorption. These results demonstrate that organic molecule covalent modification can induce novel ferromagnetism into graphene and indicate a new method to improve T_c for current DMS.

References

(1) Novoselov, K. S.; Geim, A. K.; Morozov, S. V.; Jiang, D.; Zhang, Y.; Dubonos, S. V.; Grigorieva, I. V.; Firsov, A. A. *Science* **2004**, *306*, 666-669.

(2) Richardella, A.; Tang, J. M.; Flatté, M. E.; Yazdani, A. *Nature* **2006**, *442*, 436-439.

(3) Zhu, W.G.; Zhang, Z. Y.; Kaxiras, E., *Phys. Rev. Lett.* **2008**, 100, 027205-027208.

(4) Hilkka, S.; Thomas, B.; Michael, B., *Phys. Chem. Chem. Phys.* **2009**, 11, 201–3209.

(5) Barglik-Chory, C.; Remenyi, C.; Dem, C.; Schmitt, M.; Kiefer, W.; Gould, C.; Rüster, C.; Schmidt, G.; Hofmann, D. M.; Pfistererd, D.; Müller, G., *Phys. Chem. Chem. Phys.* **2003**, 5, 1639-1643.

(6) Krasheninnikov, A. V.; Lehtinen, P. O.; Foster, A. S.; Pyykkö, P.; Nieminen, R. M. *Phys. Rev. Lett.* **2009**, *102*, 126807-126810.

(7) Choi, S. M.; Jhi, S. H. *Phys. Rev. Lett.* **2008**, *101*, 266105-266108.

(8) Lehtinen, P. O.; Foster, A. S.; Ayuela, A.; Krasheninnikov, A.; Nordlund, K.; Nieminen, R. M. *Phys. Rev. Lett.* **2003**, *91*, 017202- 017205.

(9) Zhou, J. ; Wang, Q. ; Sun, Q. ; Chen, X. S. ; Kawazoe, Y. ; Jena, P. *Nano Lett.* **2009**, *9*, 3867-3870.

(10) Wang, Y. ; Huang, Y. ; Song, Y. ; Zhang, X. Y. ; Ma, Y. F. ; Liang, J. J. ; Chen, Y. S. *Nano Lett.*, **2009**, *9*, 220-224.

(11) Bekyarova,E. ; Itkis, M. E. ; Ramesh, P. ; Berger, C. ; Sprinkle, M. ; de Heer, W. A. ; Haddon, R. C. *J. Am. Chem. Soc.* **2009**, *131*, 1336-1337.

(12) Lomeda, J. R. ; Doyle, C. D. ; Kosynkin, D. V. ; Hwang, W. F. ; Tour, J. M., *J. Am. Chem. Soc.* **2008**, *130*, 16201-16206.

(13) Park, S. J. ; Ruoff , R. S. *Nat. Nanotech.* **2009**, *4*, 217-224.

(14) Kresse, G.; Furthmu¨ller, J. *Comput. Mater. Sci.* **1996**, *6*, 15-50.

(15) Kresse, G.; Joubert, D. *Phys. Rev. B* **1999**, *59*, 1758-1775.

(16) Perdew, J. P.; Burke, K.; Ernzerhof, M. *Phys. Rev. Lett.* **1996**, *77*, 3865-3868.

(17) Zhou, S. Y.; Gweon, G. H.; Fedorov, A. V.; First, P. N.; De Heer, W. A.; Lee, D. H.;Guinea, F.; Castro Neto A. H.; Lanzara, A. *Nature Mater*. **2007**, 6, 770.

(18) Lassagne, B.; Raquet, B.; Broto, J. M.; Cleuziou, J. P.; Cuhu, T. O.; Monthioux, M.; Magrez, A. *New J. Phys.* **2006**, *8*, 1367-2630

(19) Perdew, J. P.; Wang, Y. *Phys. Rev. B* **1992**, *46*, 6671-6687.

(20) Son, Y. W.; Cohen, M. L.; Louie, S. G. *Phys. Rev. Lett.* **2006**, *97*, 216803-216806.

(21) Tapasztó, L.; Dobrik, G.; Lambin, P. ; Biró, L. P. *Nat. Nanotech.* **2008**, *3*, 397-401.

Chapter 7 Conclusion and Future Plan

7.1 Conclusion

In this thesis, four types of interfaces based on organic molecules/ZnO and organic molecules/graphene are investigated. It is found that organic molecules play an important role in manipulating the electronic structure and engineering the band gap of semiconductors. The organic dopant concentration can be varied to tune the electronic structure and band gap of substrate under a controllable way. Moreover, the hybrid organic molecule/semiconductor system can respond to the external field, e.g. electric field in a monotonic or nonlinear way. The band gap of substrates can be reduced and even metal to insulator (MIT) transition can be achieved. The band gap of substrate can be opened from zero band gap state, and be enlarged to semiconductor state. The substrate can also be non-destructively deposited by π-conjugated organic molecules to investigate the 2D hydrogen-bonded molecular network, in-plane and out-plane growth problems. The 2D hydrogen-bonded molecular network on substrate can gain the charge from substrate, open the band gap of substrate, and act as buffer layer for depositing dielectric materials such as Al_2O_3. Organic functionalization is able to manipulate the magnetic state and inject spin into substrate. The major conclusions of this work are drawn as follows:

(1) The electronic structures of ZnO($10\bar{1}0$) could be controlled by various types of carboxylic acids. The geometric structure calculation results are consistent with the recent Fourier transform infrared attenuated total reflectance (FT-IR-ATR) findings. The mercapto-acetic acid molecule could bring band gap states into the ZnO substrate. The CBM-HOMO energy difference is smaller than band gap, and LUMO resides in the CBM of semiconductor. These two fulfill the criteria for dye sensitized solar cells. At monolayer coverage, the band gap of ZnO is fully filled by mercapto-acetic acid molecular states, and the CBM of ZnO is around 0.2~0.3 eV below Fermi level. So

MIT transition comes up by mercapto-acetic acid monolayer coverage on ZnO(10 $\bar{1}$ 0). Mercapto-acetic acid/ZnO interface also behaves facet dependence that there is no MIT transition for ZnO(2 $\bar{1}$ $\bar{1}$ 0) by monolayer coverage. Acetic acid does not contribute to the band gap states of ZnO(10 $\bar{1}$ 0), whereas benzoic acid and 9-anthracenecarboxylic acid do contribute an abundance of band gap states to ZnO(10 $\bar{1}$ 0). 9-anthracenecarboxylic acid functionalized ZnO(10 $\bar{1}$ 0) shows a smaller CBM-HOMO energy difference compared to that of mercapto-acetic acid in the same situation.

(2) Each isolated F4-TCNQ molecule could gain 0.63e from bilayer graphene, and graphene shows *p*-type semiconductor characteristics. With high F4-TCNQ dopant concentration of 1.3×10^{-10} mol/cm^2, the charge transfer between each F4-TCNQ molecule and graphene is 0.45*e*, and the built-in electric field E_{bi} between the graphene layers could reach 0.070 V/Å. The band gap opening (E_g) and the gap at the Dirac point *K* (ΔE_K) are found to be 213 meV and 236 meV respectively at this high F4-TCNQ dopant concentration. The mobility of bilayer graphene is reduced by around 21% compared to pristine bilayer graphene from Drude's model. Considering the mobility varies up to one order in graphene, the mobility deformation induced by F4-TCNQ is moderate. The electronic structure of F4-TCNQ/bilayer graphene could be further tuned by E_{ext}. At 0.077 eV/Å, ΔE_K = 306 meV and E_g = 253 meV are around 71% and 49% larger than those of the pristine bilayer under the same E_{ext}.

(3) The growth of PTCDA on graphene obeys two experimentally found growth modes: α modification mode and β modification mode. For α modification mode, with critical thickness of 1 ML, the growth of PTCDA on graphene follows the Stranski-Krastanov (SK) mode. For β modification mode, the PTCDA could form two complete MLs on graphene substrate. From the thermodynamical viewpoint, α modification mode is more stable than β modification mode. At 1 ML, the PTCDA follows a planar configuration on graphene, which is almost unperturbed by typical defects in graphene substrate. For α modification mode with 2 and 3 ML coverage, the

molecular planes incline to the substrate plane with angles around 9° and 13° respectively, which indicates that bulk-like phases appear and this could also facilitate the lateral intrinsic charge transport characteristics. For α modification mode, the total charge transfer between PTCDA and graphene per $5\sqrt{3}\times5$ super cell at 2 MLs saturates with $0.42e$, which is 0.1 and $0.06e$ larger than those of 1 and 3 MLs respectively.

(4) Methoxyphenyl group could covalently modify the graphene substrate and induce a *p*-type ferromagnetism into graphene with high T_c. With a high methoxyphenyl group coverage of $4.7\times10^{14}/cm^2$, an above room temperature ferromagnetic coupling graphene sheet is obtained, meanwhile with an abundance of hole carriers around $6.1\times10^{13}/cm^2$. At this coverage, each methoxyphenyl group could totally create 1 μ_B into molecule/graphene hybrid system. Besides, an around 1.1 eV direct band gap is introduced into both majority and minority spin bands of graphene sheet. Nitrophenyl group could also induce a *p*-type ferromagnetism into graphene with T_c slightly lower than that of methoxyphenyl group modified graphene. Meanwhile, the majority band shows indirect band gap characteristic and minority bands shows direct band gap characteristic. Zigzag GNR shows strong site specific magnetism by aryl group adsorption near edge. At specific site of GNR, each molecule could totally induce 3~4 μ_B into molecule/GNR hybrid system.

7.2 Future Plan

The future plans for studying the interfacial electronic problems by first principles method are drawn as follows:

(1) Learn and study time-dependent density functional theory (TDDFT) to investigate excitation problems. Time-dependent density functional theory (TDDFT) could

accurately consider the many-body effects, which are neglected in the conventional ground state DFT. Within TDDFT, the experimentally frequently used photoabsorption, and its corresponding electronic properties will be calculated in comparison to experimental results. Another many-body effect Kondo problem will also be accurately calculated in comparison to STS of experiments.

(2) Learn and carry out the DFT+vdw method. The van der Waals interaction is not included into the conventional DFT. Using DFT plus long range dispersion term, e.g., London dispersion, one can accurately calculate the van der Waals interaction related problems. Using DFT+vdw method, the organic crystal, organic multi-layers and corresponding electronic properties will be more accurately calculated and better understood.

(3) Learn and implement non-equilibrium Green's function (NEGF) approach. By NEGF, the transport properties as well as external contact of molecular devices will be simulated and compared to experimental results. NEGF goes beyond the Landauer approach for ballistic, non-interacting electronics, and it can also include the inelastic scattering and the strong interactions between electrons from an atomistic level. The transmission probability and *I-V* curve will be able to be calculated by NEGF approach, and be compared to experimental results.

(4) Implement conventional DFT to study surface, interface and bulk problems. Use molecules, other dopants and external fields to manipulate the electronic structures of ZnO and graphene. The investigated systems and corresponding results should be based on and compared to experimental results.

List of Publications during Ph.D. Study

Journal Paper

1. Xiaoqing Tian, Qiuju Zhang, Qinghong Yuan, and Jianbin Xu, Covalent Modification Induced Novel Ferromagnetism in Graphene Sheet ***Phys. Chem. Chem. Phys.*** (submitted)
2. Xiaoqing Tian, Jianbin Xu and Xiaomu Wang, Self-Assembly of PTCDA Ultrathin Films on Graphene: Structural Phase Transition and Charge Transfer Saturation, ***J. Phys. Chem. B*** (in revision)
3. Xiaoqing Tian, Jianbin Xu and Xiaomu Wang, Band Gap Opening of Bilayer Graphene by F4-TCNQ Molecular Doping and Externally Applied Electric Field ***J. Phys. Chem. B*** **2010,** *114,* 11377–11381
4. Xiaoqing Tian, Jianbin Xu and Weiguang Xie, Controllable Modulation of the Electronic Structure of ZnO(10$\bar{1}$0) Surface by Carboxylic Acids ***J. Phys. Chem. C*** **2010,** *114,* 3973–3980

Conference Paper

1. Xiaoqing Tian, Jianbin Xu and Rong Zhang, First Principles Calculation of Nanomagnetism at Organic/Inorganic Interface, ***American Materials Research Society 2009 March Meeting***